Durham E-Theses

AGN evolution, clustering and the X-ray background

Georgantopoulos, Ioannis

AGN evolution, clustering and the X-ray background

Ioannis Georgantopoulos

Thesis submitted to the University of Durham for the degree of Doctor of Philosophy

October 1991

October 1991

DECLARATION

I hereby declare that no part of this thesis has been previously submitted to this or any other University as part of the requirement for a higher degree. The work described here was conducted mostly by the undersigned. Contributions from others are acknowledged in the text, references and in the following list of publications.

I. Georgantopoulos

To my parents Titika & Mimis.
To Margaret Plummer
To Ioannis Anthrakopoulos

Acknowledgements

List of Publications

Some of the work reported here has been published elsewhere as follows:

Georgantopoulos, I., and Shanks, T., 1989, in 23rd ESLAB Symposium on X-ray Astronomy, ed. Hunt and Battrick, ESA publications

Georgantopoulos, I., Shanks, T., Stewart, G.C., Pounds, K.A., Boyle, B.J., Griffihs, R., 1991, in Observational tests of Inflation, ed. Shanks, NATO ASI series, Kluwer

Georgantopoulos, I., Stewart, G.C., Pounds, K.A., Shanks, T., Boyle, B.J., Griffiths, R., 1991, in *Space Distribution of Quasars*, ed. Crampton, Pub. Astr. Soc. Pac.

Georgantopoulos, I., and Shanks, T., 1991, in *Space Distribution of Quasars*, ed. Crampton, Pub. Astr. Soc. Pac.

Shanks, T., Georgantopoulos, I., Stewart, G.C., Pounds, K.A., Boyle, B.J., Griffihs, R., 1991, *Nature*, **353**, 6042

Abstract

We combine optical, X-ray (Einstein and ROSAT) and infrared (IRAS) data to investigate the evolution and spatial distribution of AGN with particular emphasis on the implications for the origin of the diffuse X-ray background.

First, we derive the IRAS Seyfert luminosity function to test the continuity of properties between the Seyfert and the QSO population. The QSO luminosity function evolved back to $z \sim 0$, agrees well with the Seyfert luminosity function. In particular, the similarity of the faint parts of the two luminosity functions, suggests that the optical luminosity function is not severely affected by incompleteness due to reddening. We analyze the clustering properties of the IRAS Seyfert sample in order to probe the AGN clustering evolution. We detect clear clustering (5σ) at scales $< 20~h^{-1}$ Mpc. Comparing the Seyfert with the QSO clustering results at higher redshifts we find that a comoving model for AGN clustering evolution, where AGN clusters are expanding with the Hubble flow, is probably favoured by the data.

Using new faint CCD observations we recalibrate the photometry of the Durham UVX catalogue of Boyle et al. (1990). We show that the luminosity function 'knee' feature claimed by Boyle et al. is not an artefact of photometric errors at faint magnitudes. We evaluate the contribution of Active Galactic Nuclei (AGN) to the X-ray background using this optical luminosity function and evolve it according to Pure Luminosity Evolution models. We estimate that AGN produce around half of the X-ray background at 2 keV. This contribution is consistent with the small scale (arcmin) fluctuations of the X-ray background for both the stable and comoving model of clustering evolution. If a large number of low luminosity AGN with high intrinsic absorption is missed by the optical surveys, AGN could produce all the 2 keV intensity. Although the uncertainty in the estimate of the AGN contribution is high, this work demonstrates, at least, that Pure Luminosity Evolution models are consistent with both the X-ray background intensity and anisotropy constraints.

A recent deep ROSAT observation yields a high surface density of X-ray sources ($> 100~deg^{-2}$). Spectroscopic follow up observations show that most of these sources are QSOs. The identified QSOs contribute $\sim 30\%$ at 1 keV and therefore this is the lower limit of the AGN contribution to the X-ray background. No other class of sources contributing substantially to the X-ray background has been yet identified.

Contents

List of Figures

VI

VII

List of Tables

Chapter 1

Introduction

1.1 Overview

Almost 30 years after its discovery the origin of the X-ray background remains unknown. The main goal of this thesis is a new, detailed determination of the Active Galactic Nuclei (AGN) contribution to the X-ray background. This question was addressed by many authors in the past who used mainly the (then uncertain) optical AGN luminosity function in conjunction with the X-ray to optical luminosity relation. Recently, Ultraviolet excess (UVX) selection techniques produced large, complete samples of faint AGN and therefore constrained much better the form and evolution of the AGN luminosity function (Boyle, Shanks and Peterson 1988). Using these recent optical data, we attack afresh the problem of the AGN contribution to the X-ray background.

Related to the X-ray background are the luminosity function and the clustering properties of the Infrared Astronomical Satellite (IRAS) Seyfert galaxies. The Seyfert luminosity function unaffected by extinction, compared to

1

the optical luminosity function can give clues on whether the UVX optical luminosity function suffers from incompleteness at low luminosities; such an incompleteness has a significant impact on our estimates of the AGN X-ray emission. On the other hand, clustering affects the X-ray background anisotropy and therefore the results on the AGN clustering and its evolution help to constrain the AGN contribution to the X-ray background. However, the IRAS Seyferts, irrespectively of the X-ray background, present large astrophysical interest: Comparison of the Seyfert luminosity function with the optical Quasi Stellar Object (QSO) luminosity function probes if there is a continuity between Seyfert and QSOs which is a fundamental aspect of AGN evolution. The Seyfert clustering is of great cosmological interest: AGN probe the structure of the universe at scales intermediate between the recombination ($z \sim 1000$) and the present time ($z \sim 0$). Recent results from UVX surveys have shown that AGN of moderate redshift, $z \sim 1.5$, cluster strongly at small scales ($< 10h^{-1}$ Mpc). What remains unknown is the evolution of structure with cosmic time. Comparison of the Seyfert clustering properties with these of QSOs at higher redshifts can tie down the AGN clustering evolution models.

In the next Sections we review the X-ray background. In Sections 1.7 and 1.8 we turn to discuss the current results on the AGN luminosity function and clustering properties.

1.2   Introduction to the X-ray background

In 1962 a rocket carrying Geiger counters sensitive in the 2-6 keV range made two important discoveries. The first X-ray source, Sco X-1 and a strong, isotropic background were detected (Giacconi *et al.* 1962).

A few years later an isotropic background in the microwave region of the spectrum was discovered (Penzias and Wilson 1965). Although the microwave background has a commonly accepted, standard interpretation, the origin of the X-ray background remains unknown. What is known, however, is that the X-ray background at hard energies (> 2 keV) is of extragalactic origin. This is deduced from its angular distribution. The argument is that if emission were Galactic then since its mean free path is greater than the dimensions of the galaxy, the radiation should show the same general distribution as the matter. Such an effect is not observed: apart from a large anisotropy associated with a thick Galactic disk (Iwan *et al.* 1982), the brightness of the X-ray sky presents no systematic variation with Galactic latitude. Another, although not conclusive yet, argument in favour of the X-ray background's extragalactic nature emanates from its global anisotropy. The cosmic microwave background exhibits a dipole anisotropy consistent with a motion of the local Group of galaxies at 600 km sec^{-1} relative to the rest frame defined by the cosmic background radiation (see Strukov 1989 for a recent review). Based upon data from the HEAO1-A2 X-ray experiment the large scale anisotropy of the X-ray background appears to be compatible with such an interpretation: the X-ray background intensity shows an excess (at the 95% level of confidence) in the direction $l = 286°, b = 30°$ (Galactic coordinates), which translates to a velocity of 975 ± 165km sec^{-1} (Protheroe it et al. 1980, Shafer 1983, Shafer and Fabian 1983, Boldt 1987). Nevertheless, given the large directional uncertainties, this anisotropy is also consistent with an interpretation based on a possible component of the background associated with the Virgo Cluster (Boldt 1987).

Its extragalactic origin makes the study of the X-ray background of great astrophysical interest. The primary goal is to understand its origin. Its intensity, spectrum and fluctuations, even without explicit identification of individual sources, provide information about the nature of the sources

that contribute to it. The observed intensity and fluctuations constrain the number density of objects and their distribution on the sky, while the X-ray background spectrum gives clues on the source emission mechanisms.

1.3   The X-ray background Characteristics

We can identify three distinct observational properties of the X-ray background: its intensity, spectrum and isotropy. A breakthrough in the knowledge of these properties came with the HEAO1-A2 experiment (Boldt 1987) due to its good photon statistics and efficient non cosmic X-ray event rejection.

The intensity of the X-ray background at 10 keV is reported to be 3.2 keV keV^{-1} cm^{-2} sec^{-1} sr^{-1} (Marshall *et al.* 1980). This intensity is only a small fraction of the background intensity observed at other parts the electromagnetic spectrum and especially of that in the microwave region (Cowie 1989).

The spectrum of the X-ray background was measured in the 3-40 keV region by Marshall *et al.* (1980). The observed spectrum below 20 keV is not inconsistent with a power law of index 0.4 and the overall spectrum can be very well represented with a free-free (Bremsstrahlung) emission spectrum with a present temperature of 40 keV. This finding renewed the interest on models asserting that the X-ray background is due to free-free emission from a hot Intergalactic medium (IGM) (e.g. Cowsik and Kobetich 1972, Field and Perrenod 1977). According to these models the gas is heated at some redshift z_H and then cools adiabatically. As the free-free emissivity critically depends on density, most of the background originates around the heating redshift z_H and thus the background spectrum resembles that of

4

a single temperature gas. However, these models encounter various severe problems. First of all, a tremendous energy input is required to heat the intergalactic gas at such high temperature. It is estimated (e.g. Setti 1990) that each galaxy should deposit 10^{64} ergs to the intergalactic medium. To alleviate this energy problem, one has to assume that the heating took place at earlier epochs. As the free-free emission intensity is proportional to the square of the gas density and since density in the past was higher by a factor of $(1 + z)^3$ the energy requirements are relaxed. Also, at high redshifts relativistic effects such as electron-electron bremmstrahlung enhance the observed intensity (Guilbert and Fabian 1986). At redshifts $z \sim 3$ energetic phenonena such as those associated with QSOs were more powerful and could have played an important role in the heating of the intergalactic gas. However, even if the gas heating occured at high redshifts the baryon density required to produce the observed X-ray emission is $\Omega_B > 0.25$ (Guilbert and Fabian 1986, Barcons 1987, Taylor and Wright 1989). This is in contradiction with the standard theories of big bang nucleosynthesis, which in order to explain the light element abundances, require a low baryon density $\Omega_B < 0.19$ (Boesgaard and Steigman 1985). Again this constraint can be relaxed by assuming that the intergalactic gas is clumped, since higher densities yield higher X-ray emission. In this case the intergalactic gas would consist of cold dense blobs ($T \approx (1+z)5 \times 10^8$ K) surrounded by a less dense but hotter medium not contributing substantially to the soft X-ray background. Such a two phase IGM would have several implications. The most obvious one is fluctuations in the X-ray background (Barcons and Fabian 1988). Fluctuations in the cosmic microwave background are also expected as photons interact with the electrons of the hot intergalactic gas via Inverse Compton scattering. Fomalont et al. (1984) using Very Large Array (VLA) observations have shown that the size of the hot blobs should be of the order of few hundred kpc. Another, more important, consequence of the hot inter-

galactic gas model is the distortion of the microwave background blackbody spectrum. Inverse Compton scattering of the microwave background photons with the gas electrons should raise significantly the Rayleigh - Jeans part of the microwave background spectrum (Wright 1979). The launch of the Cosmic Microwave background Explorer satelite (COBE) gave the final blow to hot intergalactic medium theories. COBE observed the spectrum of microwave background with unprecedented accuracy (within one percent). No deviation from a blackbody spectrum was observed (Mather et al. 1990). The Comptonization of the microwave background allowed by COBE measurements implies that a hot IGM should contribute less than 3% to the XRB intensity even if the heating occurs at redshifts as low as $z \approx 2$ (Mather et al. 1990).

An important feature of the X-ray background is its small scale isotropy or its intensity fluctuations. The fluctuations provide the means for studying the number counts of the source population that produces the X-ray background, beyond the flux limit of any given X-ray survey. The argument is that a population of discrete sources produces fluctuations in excess of those expected purely from photon noise, since the number of objects in each pixel varies. The amount of fluctuations is determined by the form of the number counts: flat number counts translate to a high number of sources per pixel to produce all the X-ray background and therefore to a low level of fluctuations. Steep number counts imply that a small number of sources is producing all the X-ray background and thus the fluctuations are high. The usual way to constrain the number counts is to create background Monte Carlo simulations based on trial number count models. The amount of fluctuations is measured from the $P(D)$ distribution i.e. the frequency distribution of the number of photons D in each pixel. By minimizing the differences between observed and simulated fluctuations one can determine the properties of the underlying number count distribution up to the flux

level where there is one source per pixel (Barcons and Fabian 1989). The use of Monte Carlo simulations presents the advantage that effects like source clustering or detector vignetting can be easily taken into account. Alternatively, the P(D) distribution or its variance can be predicted analytically (Scheuer 1974, Fabian 1975, Shafer 1983).

The HEAO1-A2 X-ray experiment provided a wealth of information on the hard (2-10keV) X-ray background fluctuations. The excess fluctuations are $\delta I/I < 0.02$ on a scale of few degrees (Shafer and Fabian 1983). These fluctuations are consistent with an extrapolation of the number count distribution with a Euclidean power law slope down to a flux about one order of magnitude fainter than the Piccinoti *et al.* (1982) HEAO1-A2 survey limit. The Einstein observatory provided the opportunity to study fluctuations on arcminute scales. Hamilton and Helfand (1987) found that the observed granularity, defined as the square root of the ratio of the second moment over the first moment of the photon distribution, is $G \approx 0.17$ on 1 arcminute scale. Using Monte Carlo techniques, Hamilton and Helfand (1987) showed that if a population of sources produces all the observed X-ray emission, then its number counts should flatten from the Euclidean $\beta \approx 1.5$ slope to $\beta \approx 1.2$ or flatter just below the flux limit of the Einstein Deep Survey (Giacconi *et al.* 1979). This in turn means that the surface density of this population should exceed $\sim 5000 \ \text{deg}^{-2}$. Barcons and Fabian (1990) reanalyzed the Einstein fields of Hamilton and Helfand (1987) using analytical techniques and considering the full P(D) distribution. They confirm the Hamilton and Helfand (1987) finding for the flattening of the number counts. More recently Warwick and Stewart (1989) analysed the degree scale fluctuation (2-10 keV) from Ginga. They derive $\delta I/I \approx 0.05$ and prove that the number count distribution has a Euclidean slope. The Ginga measurements constrain the source counts at flux about 5 times fainter below the flux level reached by Shafer and Fabian (1983), but do not reach

the depth of the Einstein High Sensitivity Survey.

An alternative way to study the background anisotropy is through the auto-correlation function of the intensity fluctuations, $w(\theta)$ (Peebles 1980). This function reflects the clustering properties of the sources that produce the background. Thus, if we know the correlation function of a class of sources, using $w(\theta)$ we can derive an upper limit for the contribution of these sources to the X-ray background. $w(\theta)$ was derived by De Zotti et $al.$ (1990), on degree angular scales ($> 3°$), from HEAO1 (2-10 keV) data. Carrera et $al.$ (1991) derived $w(\theta)$ again on degree scales ($> 2°$) using Ginga (4-12 keV) data. Carrera et $al.$ (1991) derive a 95% upper limit of 10^{-4} for $w(\theta)$, 4 times lower that the HEAO1 upper limit. This places an upper limit to the AGN contribution to the hard X-ray background of $\sim 50\%$. Barcons and Fabian (1989) derived $w(\theta)$ at arcminute angular scale ($> 1'$) using Einstein IPC data. They detected some signal at $< 5'$ which is probably due to detector effects and thus cannot place very strong constraints on the AGN X-ray emission.

1.4 Discrete Source Contribution

As hot IGM models are ruled out, we should search for the origin of the X-ray background in discrete sources. The most obvious candidates are the ones detected in Einstein surveys, namely clusters of galaxies, galaxies and AGN. Let's consider the X-ray properties of these objects.

Rich clusters appear to be X-ray emitters with luminosities 10^{42} - 10^{46} erg sec^{-1} due to intergalactic hot gas, free-free emission ($2 < kT < 10$ keV). The X-ray intensity is given by $I = \int dN(S)\ S\ dS$ where $dN(S)$ are the differential number counts. Using the number counts derived by Gioia et

al. (1984) and integrating up to $S_{min} \approx 10^{-13}$ erg sec^{-1} cm^{-2} (0.5-3.5 keV), which is the flux limit of the Einstein Medium Sensitivity Survey, the derived cluster contribution to the 2 keV X-ray background is only $\sim 1\%$.

The X-ray properties of normal galaxies are reviewed by Fabbiano (1989); in general they are not strong X-ray emitters. X-rays in early type galaxies come from free-free, hot gas emission, while the X-rays in late type galaxies come from hard X-ray binaries and supernova remnants. Typical X-ray to optical luminosity ratios are 1.5×10^{-7} and 3.5×10^{-7} for spirals and ellipticals respectively (Trinchieri and Fabbiano 1985). Giacconi and Zamorani (1987), by combining the faint ($B < 27^m$) galaxy number counts (Tyson 1984) with the mean X-ray to optical flux ratio observed, conclude that galaxies contribute $\approx 13\%$ to the X-ray background intensity at 2 keV.

The discovery of many AGN by the Einstein satellite (Tananbaum *et al.* 1979, Giacconi *et al.* 1979), initially suggested that AGN could produce the whole of the X-ray background. Griffiths *et al.* (1988) detect a surface density of 20-30 X-ray sources deg^{-2} most of which are QSOs. Adding up the fluxes of these identified QSOs, yields a lower limit for the AGN contribution to the 2 keV X-ray background of $\sim 30\%$. Zamorani *et al.* (1981) and Marshall *et al.* (1983) attempted to derive the total AGN contribution by convolving the optical luminosity function with the relation between X-ray and optical luminosity. Their attempts, although hampered by the then limited knowledge of the form and evolution of the optical luminosity function, demonstrated that QSOs may produce the bulk of the X-ray background intensity at 2 keV. The derivation of the AGN X-ray emission critically depends on the X-ray to optical luminosity ratio and the X-ray spectral index. We therefore discuss these separately in the next paragraphs.

9

1.5 The spectra of Active Galactic Nuclei

X-ray emission is a common property among Seyfert galaxies (Pounds 1977, Elvis et al. 1978). The first good quality spectra were obtained by HEAO1-A2 in the 2-10 keV range (Mushotzky 1982, Petre et al. 1984). The X-ray spectral indices of the few nearby, bright Seyfert galaxies observed had values of $a_x \approx 0.7$ and very little dispersion around this mean value ($\sigma \sim$ 0.15). This result was of great astrophysical interest as the constancy of the spectral index implied some common physical processes for the generation of the continuum. Turner and Pounds (1989), observing a sample of hard X-ray selected Seyferts with EXOSAT, show that the canonical spectral index, $a_x \sim 0.7$, extends to soft energies below 2 keV. Urry and Kruper (1989) find the same result for a large Seyfert sample observed in the soft X-ray band with Einstein. Turner and Pounds (1989) and Urry and Kruper (1989) conclude that the X-ray spectrum cannot be represented by a single power law. Excess emission around 0.3 keV is superimposed on the hard power law spectrum. This excess emission can be represented by a blackbody spectrum.

While Seyferts seem to have well constrained spectra this is not the case for QSOs. The first results on QSO spectra were based on Einstein Imaging Proportional Counter (IPC) data (Wilkes and Elvis 1986). They found that radio quiet QSO have steep spectra $a_x \sim 1$, while radio loud QSO present, in general, flatter spectra, $a_x \sim 0.5$, with large dispersion. Maccacaro et al. (1988), using the hardness ratios and the detection rate as a function of Galactic latitude method (Zamorani et al. 1988), derive $a_x \approx 1$, with dispersion $\sigma = 0.36$, for the spectra of extragalactic sources. Canizares and White (1989) make a detailed analysis of the QSO mean spectra using Einstein IPC observations. They group QSOs into ensembles according to their redshift, luminosity and radio properties. The radio quiet QSOs,

which present great interest as they could be potential contributors to the X-ray background due to their high space density, have $a_x > 1$; unfortunately one object dominates the photon counts and excluding this object the uncertainty is large ($0.5 < a_x < 1.4$). The presence of soft excesses could be a potential source of error when one attempts to do spectroscopy with a low spectral resolution instrument such as the IPC, which is actually a 3 band photometer. Fitting a single power functional form to a spectrum with soft excess would result (erroneously) in a steep slope spectrum. This consideration urged Wilkes *et al.* (1989) to reanalyze their QSO, IPC spectra; combining them now with higher spectral resolution measurements from Einstein's Monitor Proportional Counter and fitting double power law models to the observed spectra, they find agreement with their previously published results. Finally, Turner *et al.* (1989) analyze hard (2-10 keV) X-ray QSO spectra from Ginga observations. For the eight objects of their sample the mean spectral index is $a_x = 0.69$ (i.e. the canonical spectral index) and the dispersion is rather high (~ 0.29). However, one should be cautious in interpreting their result as only 3 out of 8 objects are radio quiet. Two of the radio quiet objects have $a_x \sim 1$ whilst the third one (PG 1416-129) presents a peculiar very flat spectrum with $a \sim 0$. Therefore, it appears that in general radio quiet QSOs present steeper spectra than the canonical value of $a_x \approx 0.7$.

The spectra of AGN place severe constraints on their contribution to the X-ray background. The mean spectrum of the population that produces the whole of the X-ray background should be identical to the background spectrum ($a_x \approx 0.4$). As the AGN spectra are in general much steeper than $a_x = 0.4$, it is usually claimed that AGN cannot produce the total X-ray background intensity. Fabian, Canizares and Barcons (1989), by combining the 2-10 keV spectrum with the soft X-ray background measurements of Burrows *et al.* (1984), conclude that if AGN have $a_x \approx 1$, they can-

not produce more than $\sim$ 40% of the X-ray background intensity at 2-10 keV. However, Schwartz, Qian and Tucker (1989) argue that more complex spectra including energy dependent curvature for the power law index could reproduce the observed X-ray background spectrum in the 3-12 keV region. As regards the softer < 3 keV background, the lack of spectral measurements leaves the AGN contribution unconstrained. If the X-ray background spectrum shows an upturn below 2 keV, as indicated by Garmire and Nousek (1981), then AGN can contribute most of the background intensity below 2 keV.

1.6 The Relation between Optical and X-ray luminosity

The relation between optical, L_o, and X-ray luminosity, L_x, is of great astrophysical interest as it not only provides information on AGN emission mechanisms but also provides a useful tool for determining the AGN contribution to the X-ray background.

The relation between L_x and L_o is most often studied through the a_{ox} spectral index (Tananbaum et $al.$ 1979)

$$a_{ox} = \frac{-log\frac{L_x}{L_o}}{log\frac{\nu_x}{\nu_o}} \tag{1.1}$$

L_x and L_o denote the monochromatic X-ray and optical luminosity at 2 keV (6Å) and 2500Å respectively. By definition, a_{ox} represents a hypothetical power law connecting the soft X-ray with the ultraviolet part of the spectrum. When an optically selected sample is observed in the X-ray band it is not guaranteed that all objects will be detected. Therefore one deals with a sample that consists of detections and flux upper limits or a 'censored'

12

data set. Analysis of such samples, the so called survival analysis, makes the major assumption that upper limits and detections come from the same parent population. Detailed introductions to survival analysis techniques, with special emphasis on astronomical applications, are given by Avni *et al.* (1980), Feigelson and Nelson (1985) and Schmitt (1985).

Using these techniques, Avni and Tananbaum (1982) find that a_{ox} depends on optical luminosity ($a_{ox} \propto L_o^{0.07}$), which implies that optical luminous QSOs are relatively less powerful X-ray emitters. The a_{ox} dispersion is high: at a given optical luminosity the X-ray luminosity varies by at least a factor of ten. These findings were confirmed by the results of Kriss and Canizares (1985) Avni and Tananbaum (1986), which were based on large optically selected QSO samples. Avni and Tananbaum (1986) found that the data are not incompatible with a skew a_{ox} distribution towards faint X-ray luminosities. One possible interpretation of such a skew distribution is that some QSOs are X-ray quiet. Detailed statistical analyses by Kriss and Canizares (1985) and Avni and Tananbaum (1986) seem to reject this possibility but with a large number of non X-ray detections, especially at high redshifts, this result cannot be viewed yet as conclusive. Anderson and Margon (1987) analysed the a_{ox} spectral index of high redshift, faint, $B < 19.5$, QSOs. The importance of their analysis lies in the fact that these high redshift, faint QSOs are the typical contributors to the X-ray background due to their high space density. Despite the very low rate of detection ($\sim 20\%$), Anderson and Margon (1987) find good agreement with previous results.

The results above refer mostly to QSOs. At low luminosities the a_{ox} spectral index may be contaminated by host galaxy starlight and intrinsic absorption. Both these effects tend to increase a_{ox} (Kriss and Canizares 1985). Despite these uncertainties, the low luminosity AGN a_{ox} spectral index

13

seems to follow the same relation with luminosity as in QSOs (e.g. Kruper and Canizares 1989).

1.7 The AGN luminosity function and its evolution

The AGN evolution can be studied through the luminosity function, i.e. the probability distribution over luminosity. Among the early attempts to derive the optical AGN luminosity function was that by Schmidt (1972), who found that the luminosity function can be represented by a power law with slope β

$$\Phi(L) = \Phi_*(\frac{L}{L_*})^{-\beta} \qquad (1.2)$$

AGN evolve strongly. Schmidt (1968) showed that AGN of given luminosity were more numerous in the past. He interpreted this as Pure Density Evolution. According to this model the luminosity function at redshift z is given by

$$\Phi(L, z) = \Phi(L, 0)\rho(z) \qquad (1.3)$$

where $\Phi(L, 0)$ is the local AGN luminosity function and $\rho(z)$ is a function of redshift. More refined models of density evolution postulate that the AGN evolution is a function of luminosity as well (Luminosity Dependent Density Evolution, Schmidt and Green 1983). More recent AGN surveys (e.g. Marshall *et al.* 1983) have shown that the AGN evolution can be well represented by Pure Luminosity Evolution models, where the luminosity of the AGN population dims with cosmic time. However, if the AGN luminosity function is a single power law, both density and luminosity evolution can represent equally well QSO evolution. A breakthrough in AGN evolution studies came recently when Boyle, Shanks and Peterson (1988) detected

14

a turnover in the QSO luminosity function at faint luminosities: it is the shift of this turnover with redshift which shows that Pure Luminosity evolution represents most adequately the AGN evolution. According to Boyle, Shanks and Peterson (1988) the luminosity evolution follows a power law: $L(z) \propto L(z = 0)(1 + z)^k$. Then the AGN luminosity function at redshift z is given by:

$$\Phi(L, z)dL = \frac{\Phi_\star}{L_\star}[(\frac{L_\star(1 + z)^k}{L})^{-\alpha} + (\frac{L_\star(1 + z)^k}{L})^{-\beta}]^{-1}dL \qquad (1.4)$$

where $L_\star$ denotes the characteristic luminosity, i.e. the luminosity where the luminosity function breaks to a flatter power law. As $L_\star$ evolves with redshift, the slope and normalization of the luminosity function remain constant.

At low redshifts, $z < 0.1$, Seyfert galaxies can probe the AGN luminosity function. Cheng *et al.* (1985) derived the luminosity function of Markarian Seyfert galaxies. Marshall (1987) derived the luminosity function of Seyfert galaxies, selected spectroscopically from the CfA galaxy survey. Both Cheng *et al.* (1985) and Marshall (1987) find that the luminosity function shows a turnover at low luminosities similar to the QSO luminosity function at higher redshifts. UVX AGN surveys at low luminosities, may be incomplete due to starlight contamination or dust reddening. Spectroscopic surveys can also miss low luminosity AGN as it is difficult to recognise the AGN properties when the nuclear emission is weak. Therefore, as the IRAS selection is not affected by the effects above, provides a new method of probing the AGN luminosity function at low redshifts. Comparison with the optical QSO luminosity function at higher redshifts can give clues on whether there is a continuity of properties between QSO and Seyfert galaxies.

1.8 AGN clustering

Of course, the structure of the universe can be studied via galaxies and clusters at small redshifts ($z < 0.5$), while at very large redshift ($z \approx 1000$) it can be studied via the anisotropy of the microwave background. However, in the vast intermediate redshift range it is only AGN that can probe the large scale structure of the universe. Osmer (1981) first attempted to study the three dimensional QSO distribution but detected no clustering. QSO .clustering studies were dramatically improved when UVX selection in conjuction with multi object spectroscopy enabled large, complete QSO samples, to be easily produced the largest being the Durham QSO survey (Boyle *et al.* 1990). Large, but inhomogenous, catalogues were also used e.g. the Veron catalogue (Kruszewski 1988, Shaver 1988, Anderson 1988). The results from these studies show strong clustering at small scales while no clustering is present at larger scales.

An important question that remains unanswered is how structure evolves with cosmic time. Shanks *et al.* (1988), splitting their 400 QSO sample in two redshift bins, cannot discriminate between the stable evolution model (where QSOs trace clumps of mass that have collapsed and have ceased to expand with the Hubble flow) and the comoving model (where the QSO clusters still take part in the expansion of the universe). On the other hand Shaver *et al.* (1988) and Kruszewski (1988) detect strong evolution. An acid test for evolution is the study of clustering properties of low luminosity AGN, which residing at low redshifts, probably represent the endpoints of QSO evolution. Then comparison of the clustering properties of the low luminosity AGN and QSOs can directly probe the AGN clustering evolution over a large redshift range.

1.9 Thesis outline

The organization of this thesis has as follows. In Chapter 2, we derive the luminosity function of Seyfert galaxies from the IRAS Point Source Catalogue. We compare with the optical QSO luminosity function to test the relation between QSOs and Seyferts as well as the completeness of the UVX selection techniques. The infrared luminosity function is subsequently used in the evaluation of the Seyfert clustering properties.

In Chapter 3 we deal with the clustering properties of the IRAS Seyfert galaxies. We compare the low redshift, Seyfert galaxy clustering properties with these of QSOs to tie down the AGN clustering evolution. Although this chapter could be viewed independently from the X-ray background, there is relation to the latter since the AGN clustering properties affect the X-ray background fluctuations.

In Chapter 4, before addressing the issue of the X-ray background, we test the validity of the recently derived optical luminosity function (Boyle, Shanks and Peterson 1988) using new CCD observations. We particularly check if photometric errors at faint magnitudes could have produced an artificial break in the optical luminosity function. The presence of such a break critically affects the AGN X-ray emission. The break is also of particular cosmological interest as only by determining the redshift dependence of such a feature one can discriminate between different evolution models.

Then the AGN contribution to the X-ray background is addressed in detail in Chapter 5. We mainly deal with the soft 2 keV background, as the vast majority of AGN X-ray observations (e.g. spectra, L_x/L_o ratios) come from the Einstein observatory. The drawback is that the X-ray background is not well measured at these soft energies. Thus to derive the AGN contribution

to the 2 keV X-ray background we assume that the 3-40 keV spectrum observed by HEAO1 (Marshall *et al.* 1980) extrapolates down to 2 keV. There, we also predict the expected fluctuations of the X-ray background due to AGN and compare them with observations to derive further constraints on the AGN X-ray emission.

Chapter 6 was added after the completion of this thesis as an off-print chapter. It presents *very briefly*, preliminary, deep ROSAT observations of a high Galactic latitude field from the Durham QSO survey. These observations not only probe the X-ray properties of faint QSOs but also, due to their high sensitivity, resolve directly the X-ray background to a flux level higher than any previous X-ray experiment, placing directly a lower limit to the AGN X-ray emission.

We define as a QSO an object with stellar appearance, broad emission lines ($FWHM > 1000$ km sec^{-1}) and absolute magnitude $M_B < -23$ ($H_o = 50, q_o = 0.5$) following the definition of Schmidt and Green (1983). In the AGN definition we include QSOs and Seyfert nuclei.

Chapter 2

The IRAS Seyfert luminosity function

2.1 Introduction

Here, we derive the luminosity function of 192 Seyfert galaxies, selected
from the IRAS Point Source Catalogue by de Grijp *et al.* (1987) on basis of
their flat infrared spectra. Comparison of the IRAS infrared with the optical
QSO luminosity function of Boyle, Shanks and Peterson (1988), probes the
AGN evolution under the assumption that a Seyfert nucleus represents the
final stage of QSO evolution. Comparison of the optical and the infrared
luminosity function can assess if any incompleteness in the ultraviolet excess
selection technique is introduced e.g. due to reddening. Finally, the infrared
luminosity function is used later in the analysis of the clustering properties
of the Seyfert galaxy sample.

2.2   The Catalogue

Most known Seyferts have been previously found mainly through the presence of a strong ultraviolet continuum (e.g. the Markarian galaxies, see Veron 1986 and references therein) or the presence of emission lines in their spectrum (e.g. Marshall 1987, Huchra and Burg 1990).

The Infrared Astronomical Satelite (IRAS) survey has proved to be rich in finding new Seyfert galaxies. The surface density of Seyfert galaxies discovered by examination of IRAS galaxies is comparable with that of previously known Seyferts (de Grijp et $al.$ 1985).

The IRAS mission lasted from January to November 1983 during which time 96% of the sky was covered. The area missed is contained in two gaps on opposite sides of the sky, 5° wide at the widest point, centered on ecliptic longitudes of 160° and 340° and extending 60° above and below the ecliptic plane. Based on the data from this mission, the IRAS Point Source Catalogue that contains observations of $\sim$ 250,000 sources at 12, 25, 60 and 100 μm was compiled (Neugebauer et $al.$ 1984). The 60 μm is most sensitive for the detection of extragalactic objects. Roughly 25,000 galaxies have been detected about half of which had been previously listed in optical catalogs. Well over 75% of the 60 μm sources in the IRAS Point Source Catalog at $|b| < 30°$ are extragalactic (Soifer, Houck and Neugebauer, 1987). The catalogue contains sources with fluxes levels of about 0.5 Jy at 12, 25 and 60 μm and about 1.5 Jy at 100 μm. The angular resolution varies between about 0.5 arcmin at 12 μm to about 2 arcmin at 100 μm. The positional accuracy is usually better than $20''$. The galactic extinction is virtually negligible at the survey wavelengths; at galactic latitudes $|b| > 30°$, extinction in the Galaxy is $\leq$ 1% at 25, 60 and 100 μm and at most a few percent at 12 μm.

Most of the $\sim$ 25,000 galaxies in the Point Source Catalogue have relatively steep infrared (IR) spectra with indices $\alpha \sim 2.5$. This cold IR emission is believed to be produced in the disks of spiral and interacting galaxies (e.g. Young *et al.* 1984). On the other hand IR emission from the nuclear region of active galaxies is characterized by a flatter spectrum in the IR. Quasars and BL Lacs have even flatter spectra than low luminosity AGN (Soifer, Houck and Neugebauer 1987). These considerations prompted de Grijp *et al.* (1987) to compile an AGN candidate catalogue, on the basis of whether an object from the Point Source Catalogue presents a flat (i.e. blue) IR spectrum.

More specifically the exact selection criteria of the de Grijp *et al.* 'warm' source catalogue were the following:

(1) AGN colours: $-1.5 < a(25,60) < 0.0$ where a(25,60) is the spectral index defined by the nominal 25 and 60 μm flux densities. de Grijp *et al.* (1987) stress that use of the a(25,60) spectral index is more efficient than the a(60,100) spectral index as a cold galactic disk probably dominates the 60 to 100 μm spectrum masking the nuclear component.

(2) High Galactic Latitude, $|b| > 20°$, in order to minimize contamination by galactic sources. Also the sky region covered by the Magellanic clouds was rejected to minimize confusion:

$$4^h 40^{min} < a < 5^h 55^{min}, -74° < \delta < -72° \quad (SMC) \quad (2.1)$$

$$0^h 36^{min} < a < 1^h 23^{min}, -72° < \delta < -65° \quad (LMC) \quad (2.2)$$

(3) Objects with high or medium quality fluxes were included. This means that sources were confirmed on hours and seconds scale, see Beichman (1988) for details. This requirement rejects signals from non astronomical sources.

Confirming specroscopy was carried out for most objects (De Grijp *et al.* 1990). The outcome is a catalogue consisting of $\sim$ 350 AGN, namely 56 Seyfert 1, 136 Seyfert 2 and 106 Starbursts at the survey's flux limit $f_{60} = 0.5 \mathrm{Jy}$.

Seyfert galaxies have $[OIII] \lambda 5007 /H\beta > 6$, $[NII] \lambda 6850/Ha > 0.4$ (Baldwin *et al.* 1981). As this definition does not distinguish between Seyferts and QSOs, a small number of QSOs is included in the sample, classified as Seyfert 1. The rest of AGN are starburst galaxies, i.e. galaxies with the nuclear region photoionized by O and B stars. The 'warm' spectrum selection criterion provides a very efficient method for the detection of the Seyfert phenomenon. de Grijp *et al.* (1987) estimate the completeness of the IRAS AGN catalogue to $\sim$ 70% by comparision with UV and optically selected AGN samples. In low luminosity AGN where the nuclei are faint compared to the rest of the galaxy, the cold disk emission which is characterized by a steep IR spectrum dominates. Therefore selection of 'warm' spectra could introduce a bias towards low luminosity AGN. Note however, that this method is extremely effective in detecting Seyfert 2 galaxies which otherwise would remain undiscovered. The ratio of Seyfert 2 over Seyfert 1 galaxies in the IRAS AGN catalogue is $\sim$ 5/2, while in the Markarian Seyferts listed by Dahari and Roberts (1988) Seyfert 1 outnumber Seyfert 2 galaxies.

2.3   Constructing the luminosity function

Here, three independent methods to determine the luminosity function of 'field' galaxies (i.e. these not lying in rich clusters) are discussed. These methods are used to define the IR luminosity function of the IRAS Seyfert galaxies.

a. $1/V_{max}$ method

As Bingeli Sandage and Tammann (1988) point out before the eighties there was but one method to determine the galaxy luminosity function; this is the classical or $1/V_{max}$ method. Developers of this method are van den Bergh (1961) and Shapiro (1971). Detailed descriptions of this method are given in Christansen (1975), Schechter (1976) and Felten (1977). All this method does is to count the number of galaxies with luminosity L and then weight them up according to the maximum volume $V_{max}(L)$ that a galaxy of luminosity L can be observed. In detail the method has as follows. The luminosity of every galaxy is derived using the flux - luminosity relation and then galaxies are binned to logarithmic luminosity bins. The luminosity distribution of the observed sample is thus constructed. The luminosity function can be obtained from this luminosity distribution considering that bright galaxies are overrepresented since they can be observed throughout the whole volume of the survey. In contrast faint intrinsic luminosity galaxies can be sampled only in nearby volumes and therefore some weighting scheme has to be used. This weighting is simply the maximum volume through which a particular galaxy can be seen. The maximum volume corresponds to a maximum redshift z_{max}; z_{max} can be obtained from the flux - luminosity relation where the flux in this relation is now the survey flux limit. In general this is a non-linear equation that must be solved numerically using an iterative process. The maximum redshift, z_{max}, substituted in the volume expression, (Weedman 1986) gives the maximum volume V_{max}. The luminosity function at the ith luminosity bin centered on luminosity L_i is:

$$\Phi_i = \sum_{j=1}^{N_i} \frac{1}{V_{max}(L_j)} \qquad (2.3)$$

where N_i is the number of galaxies in the ith luminosity bin, i.e. the quantity $1/V_{max}(L_j)$ is taken as the contribution from that galaxy with luminosity L_j

to the total differential luminosity function in the bin $\log L, \log L + d \log L$. An approximation to the luminosity function error is $\sqrt{N}/V_{max}$, where V_{max} corresponds to luminosity L_i at the center of the ith bin. Note that Φ_i as derived from Eqn. 2.3 expresses the number of objects per unit comoving volume and per luminosity bin. Thus in order to obtain the luminosity function per unit logarithmic luminosity we have to multiply by $1/\delta log L$ where $\delta log L$ is the bin's width.

The $1/V_{max}$ method provides a non - parametric estimate of the luminosity function. However, it is desirable to represent the luminosity function by an analytic form. The free parameters of such analytic forms can be obtained fitting the predicted luminosity distribution to the data. The parameters of the luminosity function, as the slope and the characteristic break luminosity, $L_\star$, can be determined by minimizing the following quantity

$$\chi^2 = \sum_{i+1}^{\eta} \frac{(dN_i - dN_i^P)^2}{\sigma_i^2} \tag{2.4}$$

where the summation is over logarithmic luminosity bins, and η denotes the total number of these bins; dN_i is the number of objects observed in the ith luminosity bin and dN_i^P is the predicted number of objects in the same bin. dN_i^P is given by

$$dN_i^P = \int_0^z \int_{logL_{min}}^{logL_2} \Phi(logL) \, \frac{dV}{dz} \, dz \, dlogL \tag{2.5}$$

$\Phi(logL)$ is a function of the required parameters only, e.g. slope α and $L_\star$ for a Schechter form; dV/dz is the differential volume element (Weedman 1986). The lower limit of integration over luminosity is defined by $L_{min} = max(L_1, L_{lim})$. L_1 is the lower end of the ith bin. L_{lim} is the minimum luminosity detected at redshift z. The upper limit of integration L_2 is the upper end of the ith luminosity bin; σ_i^2 denotes the variance for each bin. Assuming a Poisson distribution we can substitute σ_i^2 by dN_i. It is obvious that the bins must be wide enough to contain a large number of objects in

order to have $\sigma_i^2 \approx dN_i$; five objects per bin is a minimum number (e.g. Wetherill 1982).

Minimization of the quantity χ^2 yields the required 'best fit' parameters of the analytic form. This minimization can be done in a straightforward, but slow, way by using a grid of values for the free parameters and checking one by one which set of values gives the minimum χ^2 values. More sophisticated, faster methods are discussed in Press *et al.* (1986). Note that the χ^2 fitting to the luminosity distribution gives more weight to the bins around the characteristic luminosity L_* that contain the higher number of objects.

The $1/V_{max}$ method has the advantage of being straightforward and easy to derive. Its major disadvantage, is that it assumes an homogenous galaxy distribution. If clustering occurs, the $1/V_{max}$ method yields erroneous results especially as regards the faint end of the luminosity function. Consider for example a cluster of galaxies nearby. Then since we see faint galaxies only nearby, the number density of faint galaxies is going to be based on the nearby cluster and therefore the luminosity function at faint luminosities is going to be overestimated. In contrast, if the observer resides in a low density environment, then the luminosity function will be flatter at faint intrinsic luminosities. At bright luminosities, no problem should occur since we observe bright galaxies over large volumes and therefore the number density estimate of these galaxies is a mean of cluster and field regions.

b. The Maximum Likelihood Method

This method was firstly introduced by Sandage *et al.* (1979) to derive the luminosity function of galaxies in the revised Shapley - Ames Catalogue. The method has as follows.

The number of galaxies with luminosity between $\log L$ and $\log L + d\log L$

per unit volume is given by:

$$dN(logL) = \Phi(logL) \; d\log L \tag{2.6}$$

The total number of galaxies per unit volume that can be observed at redshift z depends on the survey's flux limit, f_{lim}:

$$N(> logL) = \int_{\log L_{min}(z)}^{\infty} \Phi(logL) \; dlogL \tag{2.7}$$

where $L_{min}(z)$ is the minimum luminosity observable at redshift z. The probability that a galaxy at redshift z has luminosity $\log L$ is defined as the ratio of the number of galaxies with luminosity between $\log L$ and $\log L + d\log L$ over the total number of galaxies observed at redshift z_i

$$P_i = \frac{dN(logL_i)}{N(> logL_i)} = \frac{\Phi(logL_i)dlogL}{\int_{logL_{min}(z_i)}^{\infty} \Phi(logL)dlogL} \tag{2.8}$$

The goal is to form a likelihood function and search the best fit values of the luminosity function free parameters that maximise this likelihood function. Using the probability values defined above, the likelihood function becomes

$$ln\mathcal{L} = ln\prod_{i}^{N} P_i = \sum_{i=1}^{N} lnP_i \tag{2.9}$$

with N the total number of galaxies in the sample, or

$$ln\mathcal{L} = \sum_{i}^{N} ln(\Phi(logL_i)dlogL) - \sum_{i}^{N} ln\int_{logL_{min}(z_i)}^{\infty} \Phi(logL)dlogL \tag{2.10}$$

Assuming a Schechter form for the luminosity function the likelihood function becomes

$$ln\mathcal{L} = \sum_{i}[ln(\Phi_\star ln10) - \frac{L_i}{L_\star} + (\alpha+1)ln(\frac{L_i}{L_\star})] \tag{2.11}$$

$$+ \; N \; ln(\Phi_\star ln10) + \sum_{i}^{N} ln\int e^{-(\frac{L}{L_\star})}(\frac{logL}{L_\star})^{\alpha+1} \; dlogL \tag{2.12}$$

Defining $t = L/L_\star$ the last term of Eqn. 2.11 becomes

$$I = ln\int_{t(z_i)}^{\infty} e^{-t}t^\alpha dt \tag{2.13}$$

26

which is the definition of the incomplete Gamma function and can be readily evaluated as a series (Press *et al.* 1986). Omitting the constant terms that are of no importance in the maximization of $\ln \mathcal{L}$, Eqn. 2.11 becomes

$$\ln \mathcal{L} = \sum_i -(\frac{L_i}{L_\star}) + \sum_i (\alpha + 1)(\frac{L_i}{L_\star}) - \sum_i ln\Gamma(\alpha + 1, t(z_i)) \qquad (2.14)$$

If the luminosity function is expressed as a double power law, the likelihood function becomes

$$ln\mathcal{L} = \sum_i ln[10^{log\frac{L_\star}{L}(\alpha+1)} + 10^{log\frac{L_\star}{L}(\beta+1)}]^{-1} \qquad (2.15)$$

$$+ \sum_i ln \int_{logL_{min}(z_i)}^{\infty} [10^{log\frac{L_\star}{L}(\alpha+1)} + 10^{log\frac{L_\star}{L}(\beta+1)}]^{-1} \qquad (2.16)$$

Evaluation of this function is extremely time consuming due to the integral term. To accelerate the procedure it is better to use an optimization algorithm, Press *et al.* (1986), that makes use of the derivative of $ln\mathcal{L}$ in respect of the free parameters α, β and $L_\star$. The derivatives of the integral term can be constructed making use of the relation

$$\frac{\partial}{\partial \alpha} \int_b^{\infty} f(x, \alpha)dx = \int_b^{\infty} \frac{\partial f}{\partial \alpha}dx \qquad (2.17)$$

The maximum likelihood method has the advantage that it is independent on the sample's homogeneity. This is because the normalization constant $\Phi_\star$ which could be a function of position i.e. $\Phi_\star = \Phi_\star(x, y, z)$, cancels out in the definition of probability (Eqn. 2.8). Then, the normalizing constant $\Phi_\star$ has to be derived from the observed number counts

$$\Phi_\star = \frac{N}{\int_0^z \int_{L_{min}(z)}^{\infty} \Phi(logL) \ \Phi_\star^{-1} \ \frac{dV}{dz} \ dz \ dlogL} \qquad (2.18)$$

where N is the total number of objects in the survey. $L_{min}(z)$ is again the minimum luminosity observed at redshift z.

The confidence limits of the best fit values can be readily estimated following the prescription of Lampton *et al.* (1976) and Avni (1976). The set of free parameters $\mathbf{a}(a_1, a_2, ..., a_m)$ obtains its best fit value $\hat{\mathbf{a}}(a_1, a_2, ..., a_m)$ for the

maximum value $\mathcal{L}_{max}$ of the likelihood function. If the vector **a** of parameter values is perturbed away from **â** then $\mathcal{L}$ decreases. The region within which $\mathcal{L}$ decreases by no more than a set amount $\Delta\mathcal{L}$ defines the M dimensional confidence region around **â**. The quantity $\Delta\mathcal{L} = ln\mathcal{L}_{max} - ln\mathcal{L}$ is distributed as χ^2 with ν degrees of freedom such that $\Delta\mathcal{L} = \frac{1}{2}\chi_\nu^2(\beta)$ where β is the confidence level. In the case of a double power law luminosity function with L_* fixed, there are two degrees of freedom, ($\nu = 2$) and the 90% joint confidence level is given by $\Delta\mathcal{L} = \frac{1}{2}\chi_\nu^2(90\%) = 4.6$. In order to obtain the 90% confidence interval for the slopes α and β independently we have to find the projections of the M-dimensional ellipses defined by $\Delta\mathcal{L} = \frac{1}{2}\chi_1^2$ on the α and β axis. From inspection of tables in Avni (1976) we have $\Delta\mathcal{L} = \frac{1}{2}\chi_1^2(90\%) = 1.3$

The drawback of the maximum likelihood method is that the luminosity function is assumed to have a certain parametric form. If this form is not suitable the maximization procedure will produce erroneous results whose goodness of fit cannot be readily tested. With other words the derivation of errors described above gives only the relative errors for a given 'best fit' parameter set; parametric forms for the luminosity function that could produce better likelihoods are not taken into account.

c. Peebles method

This method was devised by P.J.E. Peebles to tackle with the problem of sample inhomogeneities. It is presented in detail in Bean (1983). This method has the advantage of producing a non - parametric luminosity function. Therefore it is not susceptible to the right choice of the analytic form for the luminosity function unlike the Sandage *et al.* (1979) maximum likelihood method. Compared with the non - parametric $1/V_{max}$ method it is superior as it is not sensitive on the presence of clustering. The method has

28

as follows.

Galaxies in the sample are binned into luminosity and distance; an array n_{ij} is thus formed with i and j running over luminosity and distance respectively. The mean number of galaxies expected in the ij^{th} bin is $\langle n_{ij} \rangle = \Phi_i \rho_j$ where Φ_i is the differential luminosity function at the ith luminosity bin and ρ_j is the actual number of galaxies in the jth distance bin, i.e. the number density of galaxies at that distance bin multiplied by the volume element $\rho_j = (\Phi_* \frac{dV}{dz})_j$. Poisson statistics give the probability of obtaining the observed number of galaxies n_{ij} in the ij^{th} bin

$$P = \langle n_{ij} \rangle^{n_{ij}} \frac{e^{-\langle n_{ij} \rangle}}{n_{ij}!} \tag{2.19}$$

Then a likelihood function can be easily formed by multiplying the probabilities from all bins, and taking the natural logarithm

$$ln\mathcal{L} = ln \prod_{ij} \langle n_{ij} \rangle^{n_{ij}} \frac{e^{-\langle n_{ij} \rangle}}{n_{ij}!} \tag{2.20}$$

The best fit values of Φ_i and ρ_j that maximize the likelihood function are sought. These values are given by $\partial ln\mathcal{L}/\partial \Phi_i = 0$ and $\partial ln\mathcal{L}/\partial \rho_j = 0$ or

$$\rho_j = \sum_i^{n_i} \frac{n_{ij}}{\sum_i^{n_i} \Phi_i} \tag{2.21}$$

and

$$\Phi_i = \sum_j^{n_j} \frac{n_{ij}}{\sum_j^{n_j} \rho_j} \tag{2.22}$$

Note that n_i and n_j are not the total number of luminosity and redshift bins respectively; n_i and n_j are functions of j and i respectively in a flux limited sample.

Caution has to be taken in the way data are binned. The numbers of luminosity and distance bins are chosen equal. Binning is over logarithmic luminosity and distance modulus $DM = logL - logf_{lim}$ instead of redshift. The binning is such that the lower end of the luminosity bin defines the

29

upper end of the distance modulus bin. For example if $logL_o$ defines the lower end of the first luminosity bin then $DM_1 = logL_o - logf_{lim}$ defines the upper end of the first distance bin. In this way all objects with luminosity within the ith luminosity bin, can be observed within the ith distance modulus bin. Some objects with luminosity L within the ith bin are going to lie in the $j = i + 1$ distance modulus bin. This bin should be discarded from the analysis so that completeness is ascertained. Then, according to this binning, summation in Eqn. 2.21 and 2.22 becomes simple; to obtain ρ_j the summation in 2.21 is over $n_i = j$. To solve Eqn. 2.21 and 2.22 we put a trial function Φ_i^0 in Eqn. 2.21 and estimate ρ_j^0 which is then inserted in Eqn. 2.22 to produce Φ_i^1; this iterative procedure continues until a stable solution is found, i.e. the Φ_i and ρ_j values converge. The trial function Φ_i^0 could be obtained from an analytic expression of the luminosity function; for example from a double power law expression with some reasonable values for the slopes α and β and the characteristic luminosity L_*.

Here again, as in the Sandage *et al.* maximum likelihood method, the shape of the luminosity function is only obtained and not the normalization factor Φ_*. Then Φ_* should be obtained from the number counts.

2.4 Completeness and evolution

The completeness of the IRAS AGN catalogue at a given flux limit can be estimated by inspection of the integral or differential number counts. The integral number counts for the total IRAS AGN sample (Seyfert 1, Seyfert 2 and Starburst) are presented in figure 2.1 The number counts turn over around 0.5 Jy due to incompleteness. We thus adopt a flux limit of 0.5 Jy and we discard objects with $f < 0.5$ Jy.
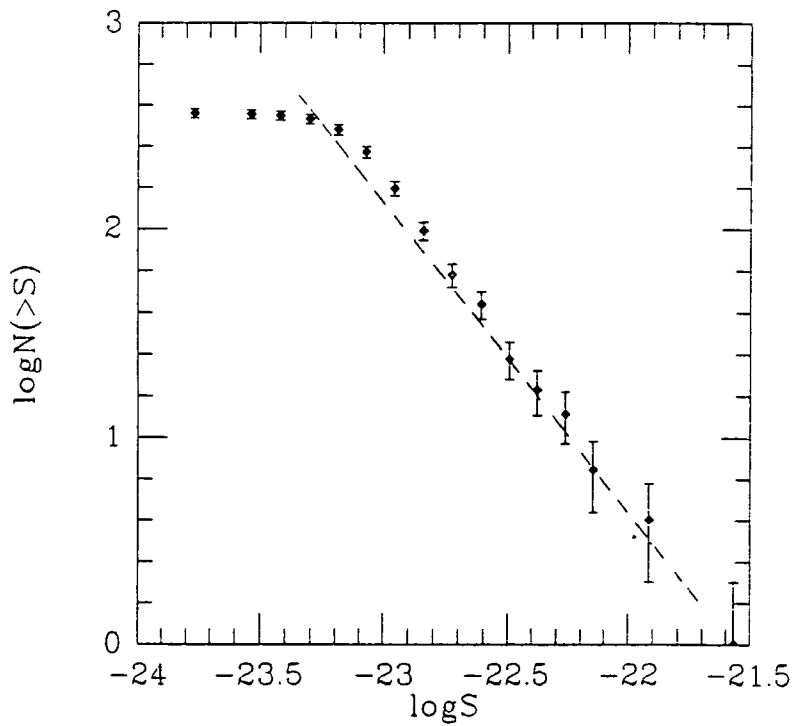
Figure 2.1: The integral number counts for all extragalactic objects of the IRAS AGN catalogue. The flux refers to monochromatic flux at $60\mu m$ and is in erg cm^{-2} sec^{-1} Hz^{-1} units. The dashed line represents the Euclidean, 1.5 slope.

Before deriving the luminosity function we have to take into account any possible evolution. Otherwise in the presence of strong evolution the luminosity function will appear flatter. A first order test, to assess cosmological evolution is the number counts. The lack of deviation from the Euclidean ($\gamma = 1.5$) slope suggests that evolution, if present, is weak in the redshift range of the IRAS AGN (the vast majority of objects have redshift $z < 0.1$). Note however, that this test is not very powerful as combination of the universe's expansion and AGN evolution could accidentally result in a Euclidean slope.

Another test for evolution is the V/V_{max} volume test. The results from this test are rather puzzling. The volume test gives 0.39 ± 0.02 for the Seyfert $1 + 2$ sample revealing probably that Seyferts are inhomogenously distributed, many of them being in a nearby cluster. Dividing the sample according to Galactic coordinates into North and South we find that this inhomogeneity is present in both South and North Galactic hemispheres. The result of the volume test, although not easily interpreted, implies that AGN evolution cannot be very strong in the small IRAS redshift range. Nevertheless in order to minimize the effects of evolution in the derivation of the luminosity function, only objects with redshift $z < 0.1$ are considered. If Seyferts evolve strongly like QSOs, then the luminosity evolution within this redshift range is at most 30% (Boyle *et al.* 1988) which is quite low compared to the width of the luminosity bins chosen in the derivation of the luminosity function.

2.5   The IR luminosity function

We can now construct the IR luminosity function separately for each galaxy group. In figure 2.2 we present the luminosity functions for the Seyfert $1 + 2$,
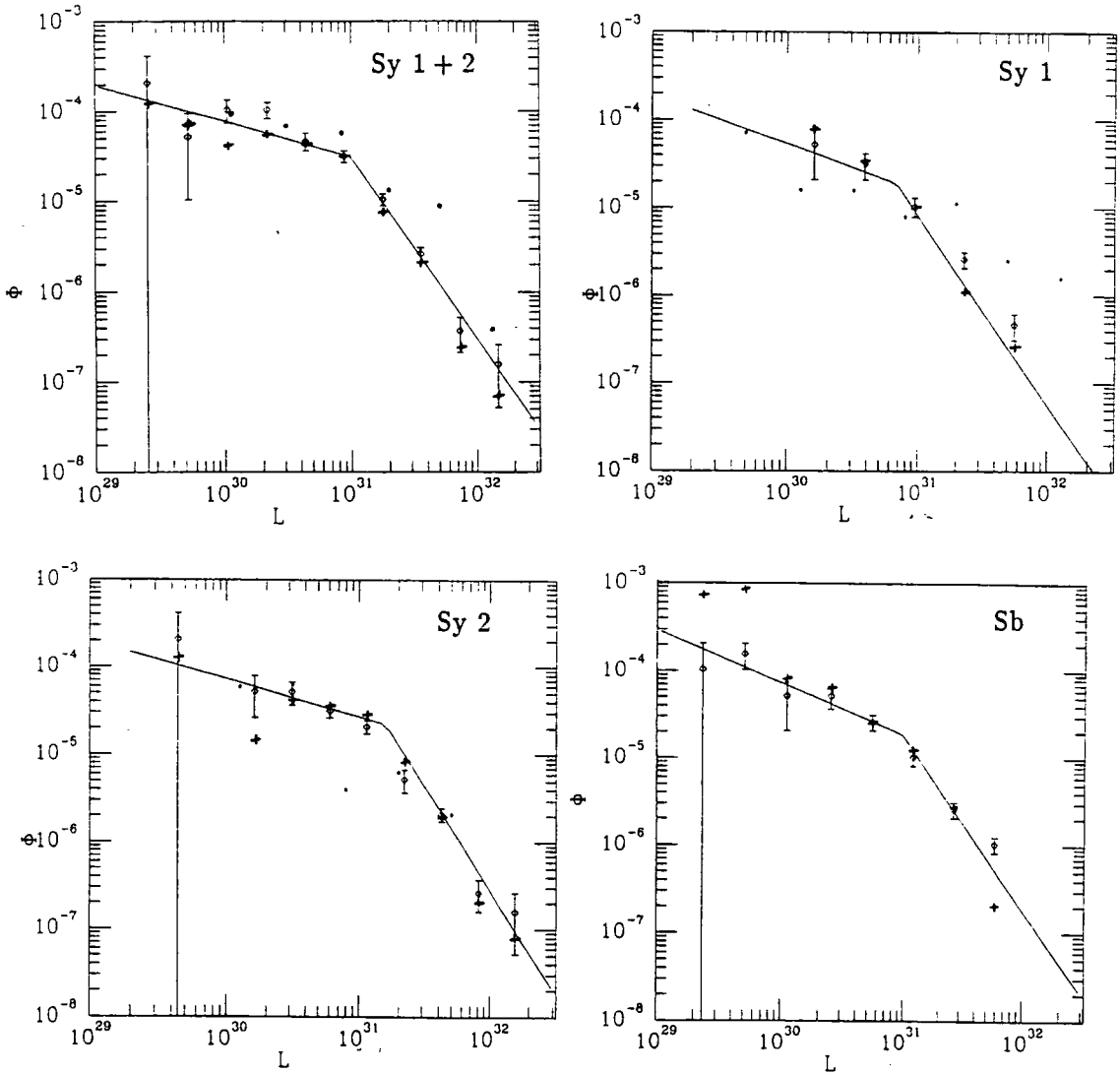
Figure 2.2: The far infrared (60μm) luminosity function of the Seyfert 1 + 2, Seyfert 1, Seyfert 2 and starburst galaxies with $z < 0.1$ and $f_{60} > 0.5$ Jy. Crosses represent the Peebles method points; diamonds represent the $1/V_{max}$ points. The solid line denotes the best fit double power law function to the crosses. Dots denote the CfA Seyfert luminosity function. The luminosity function is in Mpc^{-3} $(\delta \log L)^{-1}$ and the luminosity in erg sec^{-1} Hz^{-1} units.

Table 2.1: The Kolmogorov-Smirnov best fit to the AGN luminosity function points derived from the Peebles method.

Sample	α	β	L_*	Prob
Seyfert 1 + 2	-1.4	-3.0	31	0.45
Seyfert 1	-1.4	-3.0	30	0.10
Seyfert 2	-1.4	-3.2	31	0.96
Starburst	-1.6	-3.0	31	0.86

Seyfert 1, Seyfert 2 and starburst samples. The luminosity functions above are derived using the $1/V_{max}$ and the Peebles method. A parametric expression was fitted to the luminosity function derived by the Peebles method. This best fit was estimated by comparing the predicted cumulative, with the observed luminosity distribution using a Kolmogorov - Smirnov test (Press et al. 1986). The χ^2 test although simpler to use has the disadvantage that it produces unstable results when the number of objects per luminosity bin is small. The best fit values of the double power law parametric form according to Kolmogorov-Smirnov are given in table 2.1 together with the probability that the observed and predicted cumulative luminosity distributions are drawn from the same population.

In table 2.2 we present the best fit values for the luminosity function parameters α, β together with their 90% level of confidence errors, as derived with the maximum likelihood method (Sandage et al. 1979). L_* was fixed to the value derived from the $1/V_{max}$ method. This was necessary to ensure that stable results are obtained as unfortunately the number of objects in each sample is rather low. Comparison of the results in table 2.1 and 2.2 shows that the two maximum likelihood estimators yield consistent results.

It is interesting to compare the IRAS with the CfA Seyfert luminosity func-

Table 2.2: The AGN luminosity function as derived from the Sandage et al. (1979) Maximum Likelihood method.

Sample	α	β	L_*	$2\sigma_a$	$2\sigma_b$
Seyfert $1 + 2$	-1.2	-2.9	31.0	0.30	0.25
Seyfert 1	-1.5	-3.0	30.7	0.45	0.50
Seyfert 2	-1.1	-2.9	31.1	0.30	0.27
Starburst	-1.5	-2.5	31.0	0.28	0.30

tion at 60μm (Edelson, Rieke and Malkan 1987) and (Spinoglio and Malkan 1989). The CfA Seyfert sample was compiled by Huchra and Burg (1990); 48 Seyfert galaxies (26 Sy1 and 22 Sy2) were selected on the basis of emission lines from the CfA redshift survey (Huchra *et al.* 1983) down to a magnitude limit of $B = 14.5$. The agreement between the IRAS and the CfA Seyfert 2 galaxies is good. The Seyfert 1 samples are discrepant at the bright end of the luminosity function implying that the IRAS warm sample could be deficient in high luminosity Seyfert 1 galaxies.

2.6 The Seyfert blue luminosity function

We now compare the Seyfert galaxy luminosity function with the QSO luminosity function at higher redshifts. The aim of this comparison is to check if there is continuity between the properties of Seyfert galaxies and QSOs.

Boyle *et al.* (1988) have investigated this issue by comparing the QSO luminosity function derived at $z > 0.3$ with the Markarian Seyfert 1 galaxy luminosity function derived by Cheng *et al.* (1985). They found a rough agreement between the form and normalization of the two luminosity func-

tions. This agreement strongly argues in favour of a pure luminosity evolution model. The Markarian galaxies are selected on basis of the presence of ultraviolet excess in their spectra. Although this criterion is successful in discovering many Seyferts it fails to provide complete samples. Therefore having now a new independent selection criterion for Seyfert galaxies it is interesting to study afresh the relation between the QSO and the Seyfert luminosity function.

We first have to transform the IR luminosities at 60μm to B absolute magnitudes, in accordance to Boyle et $al.$ (1988) and Cheng et $al.$ (1985). Xu et $al.$ (1988) have investigated the relation between 60μm and the 4400Å luminosity using a sample of 28 Markarian Seyferts. The relation found was $log L_{60} = a + b \log L_B$ with $a = -2.5 \pm 3.95$ and $b = 1.17 \pm 0.39$; L_{60} and L_B are the rest frame monochromatic luminosities at 60μm and 4400 Å respectively expressed in erg sec^{-1} Hz^{-1}. Use of this small sample not only makes the relation statistically uncertain but also probably introduces a bias as it is based solely on Markarian galaxies.

To explore further the relation between L_{60} and L_B we use a subsample of 42 Seyfert galaxies from the de Grijp catalogue that have V magnitudes and B-V colours in the Veron and Veron (1987) catalogue. The magnitudes refer to the smallest possible aperture (usually 16″) to isolate the nuclear component. In the derivation of luminosities we consider that K-corrections in the IR and B are negligible. This certainly holds well for the IR where the spectral index is approximately unity and therefore just cancels out the bandwidth correction; assuming an optical spectral index of 0.5 similar to QSOs (Richstone and Schmidt 1980) the blue K-corrections are less than 1%. The relation between L_{60} and L_B for our sample is presented in figure 2.3. The results for the slope and the regression constant between L_{60} and L_B are $b = 0.72 \pm 0.15$ and $a = 10.55 \pm 4$ respectively. The scatter
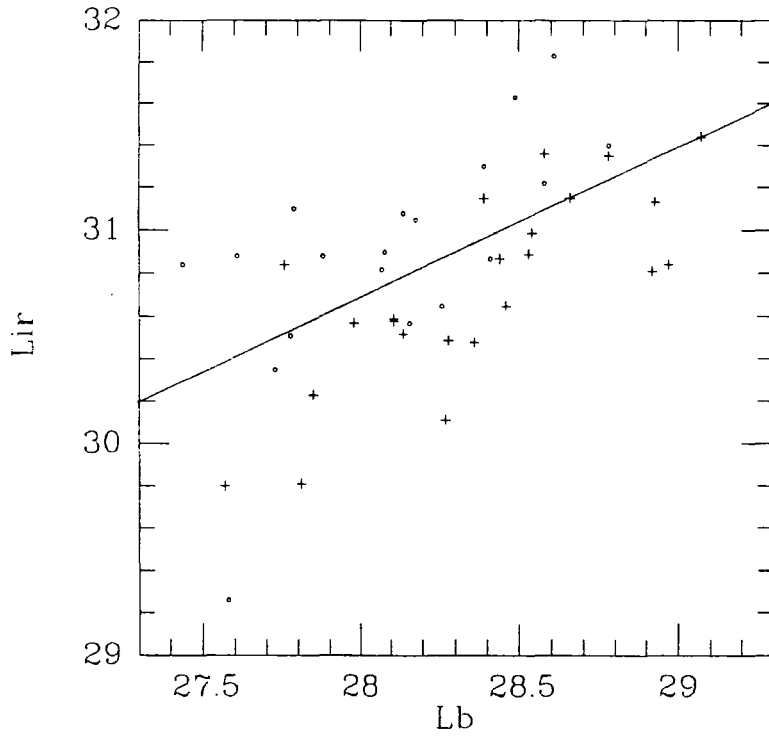
Figure 2.3: Monochromatic infrared luminosity 60μm vs. blue monochromatic luminosity (4400 Å). Dots and crosses represent Seyfert 1 and Seyfert 2 galaxies respectively. The solid line represents the best linear fit with slope $b = 0.7$. Luminosity is in erg sec^{-1} Hz^{-1} units.

around the best fit line is $\sigma = 0.40$. According to the Xu *et al.* (1988) relation, objects with luminosity around the characteristic luminosity L_* of the Seyfert luminosity function, are ~ 0.5 magnitudes brighter in the blue compared with the magnitudes estimated on basis of the relation derived here.

The effect of a non linear relation between L_{60} and L_B is to make the blue luminosity function to have a steeper slope than that of the IR luminosity function. To avoid such complicated effects given the uncertainty in the L_{60} to L_B relation it is preferable to fix the slope at $b = 1$. Then the L_{60} to L_B relation becomes $logL_{60} = 2.55 + logL_B$. Using the relation between blue absolute magnitude and monochromatic blue luminosity (Marshall *et al.* 1984) the relation between IR luminosity and blue magnitude becomes

$$M_B = -2.5 \ logL_{60} \ + \ 58.095 \qquad (2.23)$$

Using this expression we transform the IR $1/V_{max}$ luminosity function of Seyfert $1 + 2$ galaxies to the blue luminosity function; the latter is plotted in figure 2.4. The Hubble constant used here is $H_0 = 50$ km sec^{-1} Mpc^{-3} after Boyle, Shanks and Peterson (1988) and Cheng *et al.* (1985). The Boyle, Shanks and Peterson (1988) QSO luminosity function (slopes $\alpha = -1.44$ and $\beta = -3.79$, and $M_* = -22.42$) evolved back at $z \sim 0$, and the Cheng *et al.* (1985) luminosity function are also plotted on the same figure. The normalizations of the QSO and Seyfert luminosity functions seem to be in fair agreement. In this comparison, we have to bear in mind both the fact that the IRAS Seyfert luminosity function is based on a 30% incomplete sample and the uncertainties in the l_{60} to M_B transformation.
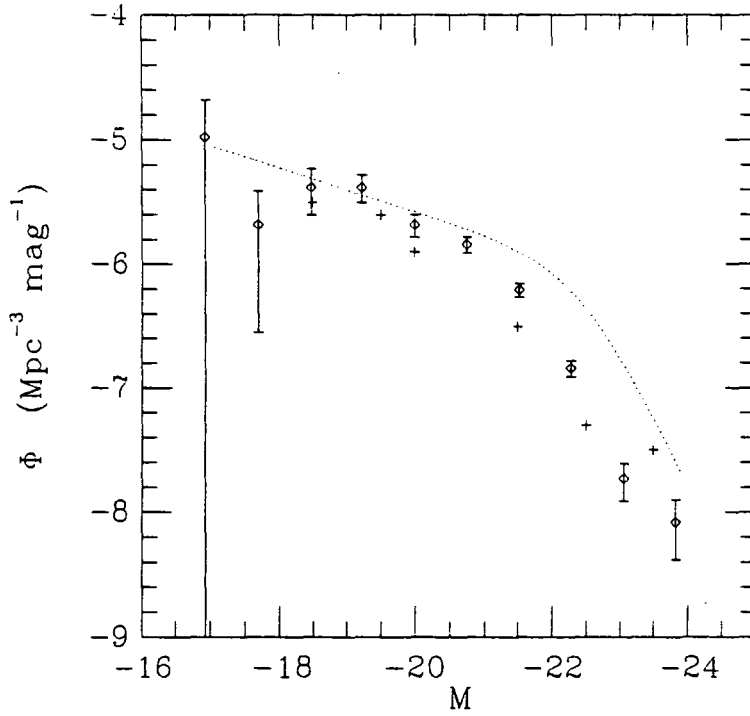
Figure 2.4: The IRAS Seyfert (diamonds) compared with the Cheng *et al.* (1985) (crosses) and the Boyle *et al.* (1988) QSO luminosity function evolved back to $z \sim 0$ (dotted line).

Chapter 3

The Clustering of IRAS Seyferts

3.1 Introduction

In this chapter we present the clustering analysis of the IRAS Seyfert galaxy
sample of de Grijp *et al.* (1987). We compare the clustering properties
of Seyfert and normal galaxies. This comparison provides information on
whether AGN randomly select the galaxy distribution. This is particularly
important as it helps us to understand if the AGN activity is related to
a certain kind of environment. Finally an important aim of the Seyfert
clustering analysis is the understanding of the AGN clustering evolution.
Comparison between the IRAS Seyfert galaxy sample and the Durham QSO
survey at higher redshifts provides a unique way to study the evolution of
structure in the universe.

3.2 Clustering Analysis

The usually applied and most sensitive statistical technique is probably the correlation function. Its use in astronomy dates back to Holmberg (1937). It was widely used in the fifties (Neyman and Scott 1952, Limber 1953, Rubin 1954). The finding by Peebles and Hauser (1974) that the distribution of the nearby one million galaxies in the Shane-Wirtanen (1954), (1967) catalogue can be characterized by a single power law demonstrates how powerful this technique is. The correlation function is defined as follows. For a random distribution of galaxies the probability δP_1 of finding a galaxy in an infinitesimal volume δV_1 is proportional to the mean number density of galaxies n, i.e. $\delta P_1 = n\, \delta V_1$. In the same way, for a random distribution, the joint probability δP_{12} of finding an object in both of the volume elements δV_1 and δV_2 is given by $\delta P_{12} = n^2 \delta V_1 \delta V_2$. Any departure from a random distribution makes the joint probability δP_{12} to differ from a simple product and this difference is what defines the two-point correlation function. The correlation function at separation r_{12} is defined by

$$\delta P_{12} = n^2 \, \delta V_1 \, \delta V_2 \, [1 + \xi(r_{12})] \tag{3.1}$$

The correlation function, ξ, is a function of separation r_{12} and does not depend on the location of the galaxy pair. From the definition of ξ (Eqn. 3.1) it is obvious that an excess probability over a random distribution, i.e. clustering, yields a positive correlation function. For a Poisson distribution, ξ is zero while negative ξ implies anti-clustering. Approximating now the distribution of objects with a continuous density function $\rho(r)$, with mean $\langle \rho(r) \rangle = n$, the joint probability δP_{12} of finding a galaxy in δV_1 at $r + r_1$ and in δV_2 at $r + r_2$ is alternatively given by

$$\delta P_{12} = \rho(r + r_1) \, \rho(r + r_2) \, \delta V_1 \delta V_2 \tag{3.2}$$

Averaging this probability over the whole sample yields the probability of observing an object in both volume elements δV_1 and δV_2 which are separated by $x = r_2 - r_1$:

$$\delta P_{12} = 1/V \; \delta V_1 \; \delta V_2 \int_V \rho(r) \; \rho(r + x) \; dV \qquad (3.3)$$

Comparing with Eqn. 3.1 yields

$$n^2[1 + \xi(x)] = 1/V \int \rho(r) \; \rho(r + x) \; dV \qquad (3.4)$$

The last relation is quite useful for it provides an estimator of the correlation function:

$$\xi(r) = \frac{N_p^o}{N_p^r} - 1 \qquad (3.5)$$

N_p^o is the number of catalogue pairs observed at separations $r - \delta r/2$ to $r + \delta r/2$. N_p^r is the number of pairs found in a random catalogue. To minimize statistical errors we have to create a catalogue with at least ten times as many objects as in the observed catalogue. A fast way to obtain $\xi(r)$ for a particular separation, r, is to count the number of neighbours that the first galaxy in the catalogue has in distance $r - \delta r/2$ to $r + \delta r/2$. Repeat the same for the second galaxy excluding from the counting the first galaxy and so on. The same procedure is followed for the random catalogue. Therefore $\frac{1}{2}N(N-1)$ pairs are counted with N the number of objects in the catalogue. Since the random catalogue contains a higher number of galaxies compared with the observed, we need to normalize the number of random pairs found. This normalizing factor is given by $f = N_o(N_o - 1)/N_r(N_r - 1)$ where N_o and N_r are the number of objects in the observed and random catalogue respectively.

At low redshifts, the distance between galaxies can be accurately estimated using Euclidean geometry. When the redshifts are not negligible it is preferable to work on a comoving system of coordinates. Osmer (1981) describes a way to find the comoving separation between two galaxies. For $q_o = 0.5$

42

the comoving separation reduces to the standard Euclidean cosine rule

$$r = \frac{c}{H_o}(s_1^2 + s_2^2 - 2s_1 s_2 cos\theta)^{0.5} \tag{3.6}$$

where s_1 and s_2 denote the distance of the first and second galaxy respectively from the observer and θ denotes the angular separation of the two galaxies on the sky.

Next, we describe the techniques used to construct the random catalogue (see also Shaver 1988). The random catalogue objects must be distributed on the sky according to Poisson statistics and must follow the observed redshift distribution. To obtain the same redshift distribution with the observed, we can draw random numbers from the observed redshift histogram. The problem with this method is that spikes in the observed redshift distribution, i.e. clusters, are reproduced in the random catalogue and therefore clustering is underestimated. To prevent this it is better to use a 'smoothed' version of the redshift distribution. This smoothed redshift distribution can be produced either by fitting a polynomial to the observed redshift distribution or by using the luminosity function. The redshift distribution is then expressed as

$$\frac{dN(z)}{dz} = \int_{z_1}^{z_2} \int_{L_{min}(z)}^{\infty} \Phi(L) \frac{dV}{dz} \, dz \, dL \tag{3.7}$$

where z_1 and z_2 define the redshift bin and $L_{min}(z)$ is the minimum luminosity that can be detected at redshift z. Alternatively the random catalogue can be constructed by reshuffling the observed redshifts. The angular coordinates remain unchanged. In this way a large number of random catalogues can be created. Then the number of pairs N_p^r between $r - \delta r/2$ and $r + \delta r/2$ is the mean number of pairs at this distance bin averaged over the total number of random catalogues. Finally, the 'boot strap' method keeps the observed redshifts unchanged but the angular coordinates on the sky are assigned random values. As both the 'reshuffling' and the 'boot strap' method use the exact observed redshift distribution to create the random catalogue,

43

they tend to underestimate clustering when the redshift distribution is not smooth.

Assuming that the errors in the number of observed pairs are Poissonian the error in the correlation function, ξ, from Eqn. 3.5, is:

$$\epsilon = \frac{\sqrt{N_p^o}}{N_p^r} = \sqrt{\frac{1+\xi}{N_p^r}} \qquad (3.8)$$

Poissonian errors are expected to underestimate the actual errors if the pairs are not independent e.g. if all pairs come from a single cluster of galaxies.

3.3 IRAS AGN Correlation Function

Before applying an elaborate statistical tool as the correlation function on the IRAS sample, it is useful to inspect the AGN distribution on the sky. The equal area (Aitoff) projections of all extragalactic objects and of all Seyferts with $z < 0.1$ and $f_{60} > 0.5$ Jy are given in figure 3.1. The Aitoff projection of a 5000 object random catalogue is presented on the same figuere as well; here the IRAS mask can be clearly seen. Inspection of the IRAS AGN distribution on the sky shows some clustered regions and voids. The correlation function should now place some statistical significance to this empirical finding.

The IRAS point source catalogue and consequently the de Grijp *et al.* catalogue does not cover the whole sky. As explained earlier a large strip of the sky with Galactic latitude $|b| < 20°$ was avoided. Also smaller parts like the 5° gap and small patches of the sky containing bright sources were not included. All these regions, the so called IRAS mask, have to be taken into account into the production of the random catalogue: random objects should avoid the parts of the sky defined by the IRAS mask.
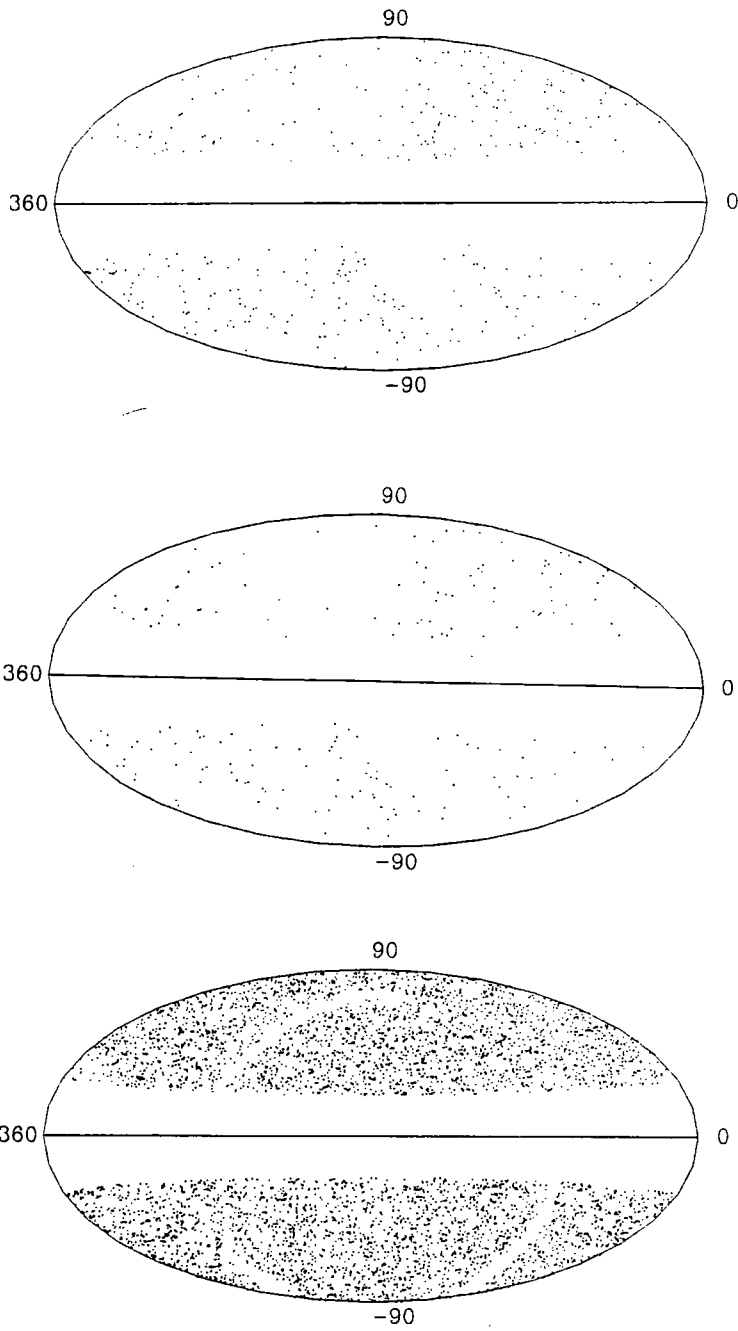
Figure 3.1: Aitoff projection of (top to bottom): all extragalactic objects from the IRAS AGN catalogue; IRAS Seyferts with $z < 0.1$ and flux at $60\mu m$, $f > 0.5$ Jy; a random catalogue of 5000 objects.

Relativistic corrections in the evaluation of galaxy separations were taken into account. Using the recipe of Osmer (1981) the comoving galaxy separations were evaluated through Eqn. 3.6. The effect on the correlation function was found to be negligible. This is more or less expected as our galaxies have low redshifts, $z < 0.1$. Thus, for simplicity, galaxy separations are approximated by Euclidean distances.

The estimation of the correlation function sensitively depends on the redshift distribution of the random catalogue. The small scale clustering results are solely affected by the catalogue's redshift distribution at low redshifts. As an example consider the Seyfert $1 + 2$ sample; there are 20 pairs of galaxies with separation below 10 h^{-1} Mpc. All of the galaxies in these pairs have redshift $z < 0.02$, i.e. the small scale clustering results come from the nearby Seyferts. As a consequence, an innacurate redshift distribution, especially at low redshifts, used in the construction of the random catalogue, may appear as excess (less) clustering detected above (below) the actual amount of clustering.

To explore further the effect of the random catalogue redshift distribution on the detected clustering and to ensure that we obtain the true clustering amplitude we compare the correlation function of the Seyfert $1 + 2$ sample derived with various different techniques. The luminosity function, the polynomial fit and the bootstrap method give very similar results. The exact observed n(z) distribution and the reshuffling method seem to underestimate the clustering by as much as 30%. However, the detection of some clustering even with these two methods ascertains that the AGN clustering detected here, by no means is an artifact of a poor fit to the observed redshift distribution. In the following we use the luminosity function as derived from the Peebles method to produce the random catalogue. Note however, that the choice of the luminosity function derivation method hardly affects

the present results. The predicted and observed redshift distributions are shown in figure 3.2.

In figure 3.3 we present the correlation function for the Seyfert $1+2$, Seyfert 1, Seyfert 2 and Starburst sample. The errorbars plotted are Poissonian and are derived through Eqn. 3.8. This is justified as in e.g. the Seyfert $1 + 2$ sample around 70% of the pairs below 10 h^{-1} Mpc are independent. To check if Poissonian errors give a fair representation of the actual errors, we divide the Seyfert $1 + 2$ sample in two subsamples according to Galactic coordinates (South and North) and we derive the correlation function separately for these two subsamples. We find that these field to field errors are in reasonable agreement with Poissonian errors.

Inspection of the Seyfert $1 + 2$ and Seyfert 2 sample correlation function indicates that Seyferts cluster strongly on scales below 20 h^{-1} Mpc. Unfortunately the correlation function of Seyfert 1 galaxies cannot be examined on this scale as there are not enough close pairs. Starbursts do not seem to present significant clustering around 10 h^{-1} Mpc although their correlation function is very noisy. At large scales ($> 20h^{-1}$) Mpc there is no significant evidence for clustering in all samples. The only hint for large scale structure is a bump around 100 h^{-1} Mpc. This bump is not an artifact of the random catalogue redshift distribution as this feature is still present even when the random catalogue follows the exact observed redshift distribution or when the sample is divided in South and North subsamples.

The small scale clustering result can be quantitatively assessed by measuring the number of observed (O) pairs below 20 h^{-1} Mpc (where the correlation function falls to zero) and comparing it with the expected number of random (P) pairs; the results are presented in table 3.1. There is a clear 5σ detection of Seyfert clustering. Independently, Seyfert 2 galaxies show clear evidence
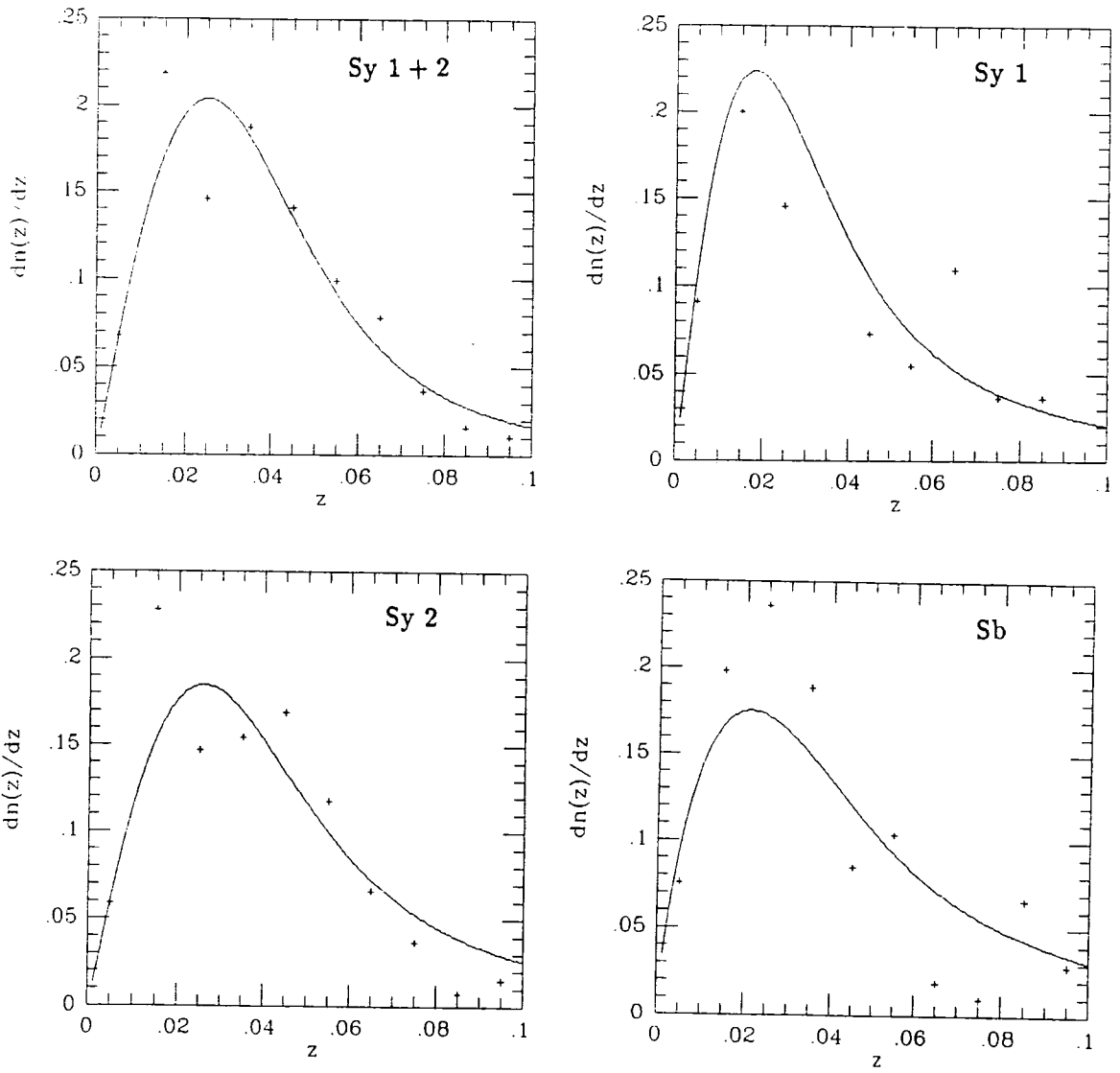
Figure 3.2: The observed (crosses) and predicted (solid line) redshift distribution of the IRAS Seyfert and Starburst galaxies.
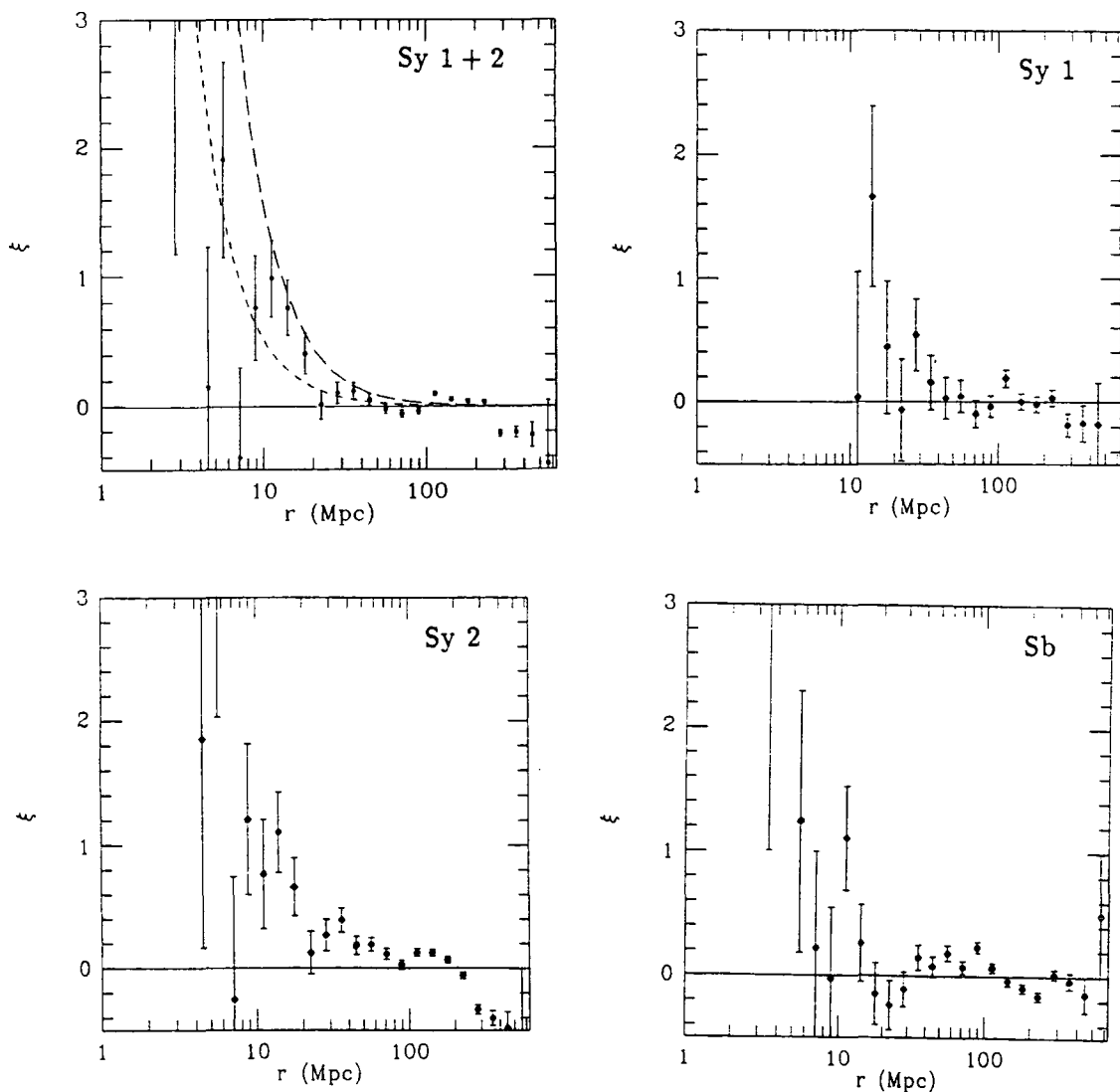
Figure 3.3: The correlation function of the Seyfert 1 + 2, Seyfert 1, Seyfert 2 and the Starburst sample. The Seyfert 1+2 correlation function is compared with the QSO correlation function evolved back to $z \sim 0$ according to the comoving (short dash) and the stable model (long dash).

Table 3.1: Integral AGN correlation function

Sample	< $10h^{-1}$Mpc				< $20h^{-1}$Mpc			
	O	P	ξ	σ	O	P	ξ	σ
Sy 1 + 2	20	13.6	0.47	1.7	142	93.4	0.52	5
Sy 1	0	1.8		1.4	11	12.1	-0.10	0.3
Sy 2	12	5.5	1.2	2.8	71	38.1	0.86	5.3
Starburst	9	6.6	0.36	0.9	50	41.4	0.21	1.3

(5.3σ) of clustering below 20 h^{-1} Mpc. Starbursts present, if at all 1.3σ, very weak clustering on scales less than 20 h^{-1} Mpc.

We next compare the Seyfert and the optical galaxy correlation function. It has long been established (e.g. Groth and Peebles 1977) that the galaxy correlation function at small scales can be well represented with a power law of slope $\gamma = 1.8$. At larger scales the correlation function may present a break to a steeper power law (slope $\gamma = 3$). Recent results from large galaxy redshift surveys suggest that the galaxy correlation function is actually more complicated presenting a shoulder feature at small scales (Shanks *et al.* 1989). According to Shanks *et al.* (1989) the galaxy correlation function can be expressed as

$$
\begin{aligned}
\xi(r) &= 16(rh)^{-1.8} & r < 2h^{-1}\ Mpc \\
\xi(r) &= 33(rh)^{-1.8} & 2 < r < 7h^{-1}\ Mpc \\
\xi(r) &= 343(rh)^{-3} & r > 7h^{-1}\ Mpc
\end{aligned}
\tag{3.9}
$$

We compare the Seyfert and optical galaxy correlation function by comparing the number of observed Seyfert and random galaxy pairs below 10 and $20h^{-1}$ Mpc. The number of galaxy pairs is evaluated considering that the mean number of neighbours within distance r of a randomly chosen galaxy exceeds the number expected for a uniform distribution by the fractional

Table 3.2: The Seyfert and optical galaxy integral correlation function

Sample	< 10Mpc	< 20Mpc
Seyfert 1 + 2	20	142
Optical Galaxy	25	115

amount

$$\frac{\delta N}{N_r} = \frac{3}{r^3} \int_0^r \xi(r')\, r'^2\, dr' \tag{3.10}$$

(Peebles 1981). Then the number of galaxy pairs expected below r is given by

$$N_G = \frac{\delta N}{N_r}\, N_r + N_r \tag{3.11}$$

The number of Seyfert pairs actually observed is compared with the predicted number of galaxy pairs at scales below 10 and 20 h^{-1} Mpc in table 3.2. The amplitude of the Seyfert correlation function agrees, within 1σ, with the amplitude expected for normal galaxies below $10h^{-1}$ Mpc. Below 20 h^{-1} Mpc, the Seyfert galaxies appear to cluster more strongly than the galaxies at the $\sim 2\sigma$ level of confidence assuming Poissonian statistics.

To investigate further the relation between the Seyfert and the galaxy clustering properties, we use the Seyfert - IRAS normal galaxy cross correlation function. Provided that the IRAS sample contains a number of galaxies much higher than the number of Seyferts, the cross correlation function can be derived with small statistical uncertainties. Then comparison between the Seyfert - IRAS galaxy and the IRAS galaxy autocorrelation function can provide strong constraints on the strength of the Seyfert clustering.

3.4 The AGN - IRAS Galaxy cross - correlation function

To derive the cross correlation function we need a galaxy sample covering the same area on the sky with the IRAS AGN sample. An ideal sample is the QMC-Cambridge-Durham (QCD) survey (Lawrence *et al.* 1989). This is a sample of IRAS galaxies obtained with a 1 in 6 random selection. There are $\sim$ 1600 galaxies with $|b| > 20°$ and $z < 0.1$ in this sample with fluxes $f > 0.6$ Jy.

The cross correlation function is derived in much the same way with the (auto) correlation function. We first estimate the number of actually observed AGN-galaxy pairs within distance $r - \delta r/2$ and $r + \delta r/2$. Then we count the number of AGN - random galaxy pairs over the same range in separations after normalizing for the respective number of objects in the observed and random catalogue. The random galaxy catalogue is obtained, as in the case of the correlation function, by randomly distributing points on the sky over the surveyed areas. The random redshifts are drawn from the exact observed redshift distribution histogram. As the observed redshift distribution of $\sim$ 1600 galaxies is relatively smooth this technique is not expected to underestimate the actual amount of clustering. The AGN-galaxy cross correlation function, at distance r, is given by the ratio of observed number of AGN-galaxy pairs over the number of AGN-random galaxy pairs, minus one (Eqn. 3.5).

The Seyfert 1 + 2, Seyfert 1, Seyfert 2, Starburst galaxy versus QCD galaxy cross correlation functions are presented in figure 3.4. For comparison the QCD galaxy correlation function is ploted on the same figure. The entries of table 3.3 list the number of AGN-galaxy observed and expected pairs
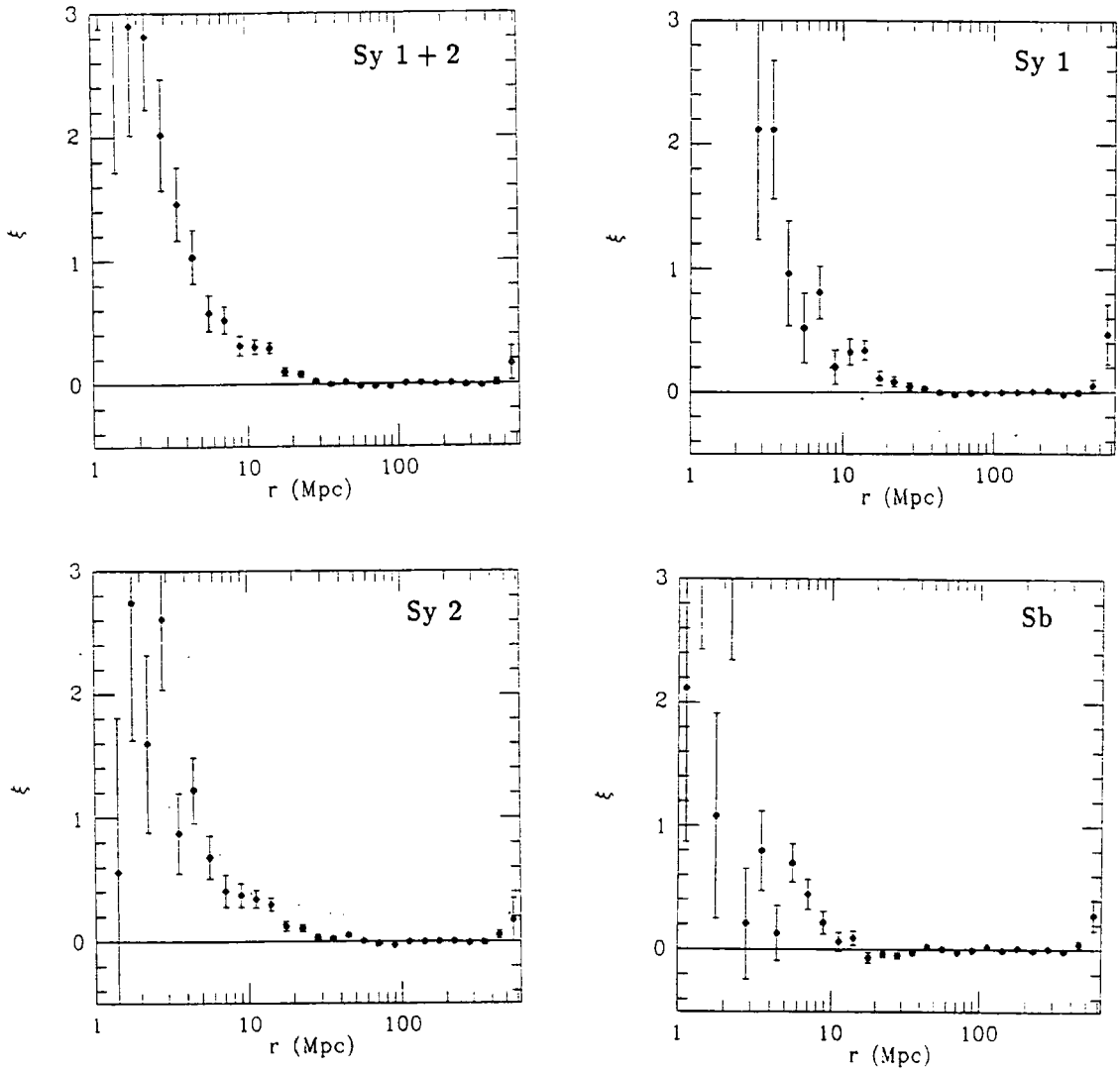
Figure 3.4: The cross correlation function of the IRAS AGN - QCD galaxy sample.

Table 3.3: The IRAS AGN - QCD galaxy cross - correlation and the QCD galaxy correlation function below 5, 10 and 10 h^{-1} Mpc

Sample	$< 5h^{-1}$Mpc			$< 10h^{-1}$Mpc			$< 20h^{-1}$Mpc		
	O	P	ξ	O	P	ξ	O	P	ξ
Sy 1 + 2	108	44	1.5	520	330	0.58	2682	2114	0.27
Sy 1	33	11	2.0	154	98	0.58	829	655	0.26
Sy 2	70	30	1.3	361	234	0.55	1848	1460	0.27
Starburst	31	19	0.6	371	265	0.40	1492	1385	0.08
QCD	867	505	0.7	4277	3051	0.40	18760	15984	0.17

below 10 and 20 h^{-1} Mpc; The random (P) and observed (O) number of QCD galaxy pairs is given in the last row of this table. Inspection of this table suggests the following.

The amplitude of the Seyfert - IRAS galaxy cross correlation function appears higher than that of the IRAS galaxy correlation function. Below $5h^{-1}$ Mpc the number of observed Seyfert - normal galaxy pairs is 2.5 times higher than the number expected, and this is a 4σ result. However, this result could just be a consequence of the poorly defined IRAS galaxy correlation function below $5h^{-1}$ Mpc. This is not unreasonable as the QCD sample selects randomly 1 out of 6 galaxies and this might have introduced some bias at close separations. Below 10 and $< 20h^{-1}$ Mpc the amplitude of the Seyfert - IRAS galaxy correlation function is still higher than that of the galaxy correlation function at the $\sim 3\sigma$ level of confidence.

There is no difference between the Seyfert 1 - IRAS galaxy and the Seyfert 2 - IRAS galaxy cross correlation function. This suggests that Seyfert 1 and Seyfert 2 galaxies have very similar environments.

The amplitude of the Starburst - IRAS normal galaxy cross correlation function is similar to the galaxy correlation function below 10 h^{-1} Mpc. This picture slightly changes when we make a comparison at larger scale, below 20 h^{-1} Mpc, as the galaxy correlation function presents more power than the Starburst - normal galaxy cross correlation function at this scale. This difference is statistically significant at the 3σ level of confidence assuming Poissonian statistics.

3.5 QSO versus Seyfert correlation function

A major aim of the Seyfert clustering analysis is the comparison of the Seyfert correlation function with that of QSOs at higher redshifts. This probes the AGN clustering evolution and thus the evolution of structure in the universe, provided that AGN are good tracers of the mass distribution. We emphasize that comparison between the Seyfert and QSO clustering involves the following assumptions. First, Seyferts and QSOs are the same objects observed at different cosmic epochs i.e. the Seyfert phenomenon is the endpoint of QSO evolution. Second, IRAS selects Seyferts without introducing any bias towards low density regions: comparison of the clustering properties of optical and IRAS galaxies suggests that IRAS avoids dense regions. This is because, elliptical galaxies that are found in high density regions are not strong infrared emitters. However, this is not the case for Seyfert nuclei that are associated with spiral galaxies.

The simplest models for clustering evolution are the comoving and the stable model. According to the stable model, AGN trace clumps of mass that have gravitationally collapsed in bound units and have ceased to take part in the general expansion of the universe. On the other hand, recent theories of galaxy formation are in favour of biased galaxy clustering where AGN, even

at small scales where clustering is strong, are expanding with the Hubble flow. According to this comoving model of AGN clustering the amplitude of the correlation function remains constant as a function of redshift.

The QSO correlation function was analysed by Shanks *et al.* (1987) and Shanks *et al.* (1988). This analysis was based on $\sim$ 400 QSOs from the Durham Ultraviolet excess (UVX) survey (Boyle *et al.* 1990). The results show that the QSO correlation function at small comoving scales, $< 10h^{-1}$ Mpc, can be represented by a power law with a slope of $\gamma = 1.8$ and an amplitude of $B = 33 \ Mpc^{1.8}$, where this result refers to the mean redshift, $\overline{z} = 1.5$, of the Durham QSO survey. At larger scales a break might occur to a steeper power law. This steeper power law represents the region where the galaxies have not collapsed to form bound units and still take part in the Hubble expansion. Theoretically in this regime the correlation function is expected to be $\xi(r) \propto (rh)^{-3-n}$ where n is the power of the spectrum of mass density fluctuations (Peebles 1980). For random initial fluctuations $n = 0$. Therefore the correlation function at $\overline{z} = 1.5$ can be expressed as:

$$\begin{aligned}
\xi(r) &= 33(rh)^{-1.8} \qquad r < 7h^{-1} \ Mpc \\
\xi(r) &= 343(rh)^{-3} \qquad r > 7h^{-1} \ Mpc
\end{aligned} \qquad (3.12)$$

As it will be demonstrated below, the results up to 20 h^{-1} Mpc are hardly affected by the presence of such a break.

As in the stable model the AGN correlation function evolves with redshift we cannot directly compare the QSO and Seyfert correlation function at the same comoving separations. Instead we have to evolve the QSO correlation function at present epoch. The form of the correlation function evolution depends on the cosmological model adopted and thus we will have to consider separately the case of an open and a closed universe. In the case of a closed $q_o = 0.5$ universe the comoving break, r_o, of the correlation function increases with cosmic time due to gravitational growth as $r_o \propto (1 + z)^{-3/2}$,

Peebles (1980). Ensuring that the break still occurs at $\xi = 1$ the QSO correlation function becomes at $z \sim 0$:

$$\xi(z=0) = (1+z)^{1.2} \, B(z) \, (rh)^{-1.8}, \qquad r < (1+z)^{1.2/1.8} r_o(z) \qquad (3.13)$$

where $B(z)$ and $r_o(z)$ are the correlation function's amplitude and break respectively at redshift z. The evolved QSO correlation function is thus given by:

$$\xi(r) = 100(rh)^{-1.8}, \qquad r < 13h^{-1} \, Mpc$$

$$\xi(r) = 2200(rh)^{-3}, \qquad r > 13h^{-1} \, Mpc \qquad (3.14)$$

On the other hand, in the case of an open universe, the break of the correlation function remains constant from $z \sim 1/\Omega$ to $z \sim 0$ in proper coordinates (Peebles 1980). This can be explained intuitively by considering that in the open universe the expansion counteracts gravity, thus preventing clumps to grow gravitationally by attracting surrounding mass. However, the clustering amplitude will increase as a function of cosmic time since the density within the clump increases compared with the background density. The amplitude B evolves in exactly the same way as in the case of a closed universe, $B \propto (1+z)^{1.2}$ in comoving coordinates. Thus the QSO correlation function becomes

$$\xi(z=0) = (1+z)^{1.2} \, B(z) \, (rh)^{-1.8}, \quad r < (1+z)r_o(z) \qquad (3.15)$$

In the open universe the QSO correlation function takes the following form at $z \sim 0$.

$$\xi(r) = 100 \, (rh)^{-1.8} \qquad r < 17.5h^{-1} Mpc$$

$$\xi(r) = 2200 \, (rh)^{-3} \qquad r > 17.5h^{-1} Mpc \qquad (3.16)$$

Next, we compare the expected QSO with the observed number of Seyfert pairs, for the comoving and the stable model (table 3.4). We distinguish

Table 3.4: Predicted and data AGN pairs out to separations of 10 and 20 h^{-1} Mpc.

	QSO		Seyfert	
	< 10	< 20	< 10	< 20
Stable ($q_o = 0.5$)	60(12)	190(27)	20	142
Stable ($q_o = 0$)	60(12)	194(27)	20	142
Comoving	27(4)	115(10)	20	142

between the case of an open and a closed universe. The number of QSO pairs is evaluated from Eqn. 3.11. The error on the number of predicted QSO pairs is evaluated on basis of a QSO correlation function error of $8.5Mpc^{1.8}$ (Boyle $et\ al.$ 1991) and is given in brackets in table 3.4.

Below $20h^{-1}$ Mpc, the comoving model provides a reasonable fit to to the data while the stable model is rejected at the $\sim 5\sigma$ level of confidence. Note however, that the disagreement between the stable model and the data comes mainly from scales $< 10h^{-1}$ Mpc where the number of pairs is small and therefore the statistical uncertainty high. At scales $10 < r < 20h^{-1}$ Mpc the stable model does not provide a bad fit to the data. Therefore, although the comoving model is more consistent with the data the results do not allow yet a conclusive answer.

Chapter 4

QSO CCD observations

4.1 Introduction

The luminosity function of QSOs was recently derived from the Durham UVX survey by Boyle, Shanks and Peterson (1988). This is the largest, complete QSO survey and contains ~ 400 QSOs with redshifts up to 2.2. It is an ultraviolet excess (UVX) survey, i.e. QSOs are selected through their abnormally low U-B colour. To obtain a large number of QSO candidates, photographic plates were used. They were scanned using the COSMOS microdensitometer and then objects with stellar appearance were selected. Calibration of the COSMOS magnitudes was attempted using a limited number of CCD sequences (Boyle et al 1990).

However, in many fields the U magnitudes were based only on bright sequences which were extrapolated to fainter magnitudes. This extrapolation was based on the assumption that the peak of the U-B colour distribution remains at the same colour as B magnitude becomes fainter. In one field (QSI) no U CCD sequences existed. In addition, the fact that the turnover

of the QSO luminosity function occurs at all redshifts at the same magnitude ($B \sim 20^m$) is worrying, as systematic errors at faint magnitudes could introduce an apparent turnover. Indeed, systematic errors not only affect the magnitudes of the already confirmed QSOs, but, more importantly, introduce a systematic error in the U-B colour which is used in the selection of QSO candidates. As an example, consider the case where the U magnitudes are, erroneously, found ~ 0.3 mag fainter than the actual ones; then if the chosen UVX limit is e.g. $U - B = -0.5$ this translates to a true UVX limit of $U - B = -0.8$. This leads to a loss of QSO candidates and thus introduces incompleteness. If the errors are independent of magnitude, incompleteness will just affect the normalization of the luminosity function. If, however, systematic errors occur at faint magnitudes only, then the faint luminosity tail of the luminosity function is preferrentially affected by incompleteness.

As the Durham QSO catalogue forms the basis of all our models on the QSO contribution to the X-ray background, its validity must first be firmly established. Moreover, it is important to check the Durham catalogue photometry since this catalogue has had significant impact on many other fields of QSO astronomy, such as physical models for QSO evolution and QSO clustering. Here, we re-calibrate the photometry of the Durham UVX survey using new, faint CCD observations.

4.2   The CCD Data and their reduction

Dr. T. Shanks and Dr. R. Fong obtained U, B and R observations of 38 QSO targets on eight successive nights (2-9 August 1989) at the 0.9−m telescope of the Cerro Tololo Interamerican Observatory in Chile. The detector used was a TI CCD which has a high U efficiency. Its field of view is approximately $3'.3 \times 3'.3$ while the pixel size is $\sim 0''.494$. In total

~ 200 CCD frames with exposure time varying from 60 to 1200 *sec* were obtained. Several hundred stellar images can be found on these frames. These images are used for the recalibration of the U and B magnitudes of the Durham UVX survey. The R frames are necessary in order to obtain the standard Johnson magnitudes (Johnson and Morgan, 1953) from the CCD magnitudes. Of the total of eight nights allocated, four were of sufficient photometric quality, while during one night no observations were obtained due to bad weather conditions. The reduction of the CCD data described here was done in collaboration with Dr. R. Fong and Dr. T. Shanks.

The first stage of CCD reduction involves the debiasing and flatfielding of the frames. Debiasing ensures that any instrumental offset is subtracted while flatfielding wipes out any possible nonuniformity in the sensitivity of the detector, e.g. bad pixels due to the chip's response.

Displaying the CCD frames and using the cursor one can easily record the X and Y positions of stellar images. Instead of separating the galaxy and stellar images on the CCD frames visually, we used the results of a star-galaxy separation routine applied to the COSMOS scans of the relevant photographic plates (Boyle 1986): if a Gaussian of width σ is fitted to the images then on a σ vs. magnitude diagram the tight stellar locus is clearly visible with the extended, non-stellar images lying above this locus.

Once the stellar image positions are recorded, they are fed automatically to an aperture photometry program (PHOTOM, Eaton 1988) to obtain raw magnitudes. An aperture radius of 5 pixels is used. This aperture provides a reasonable reconciliation between good photon statistics and high signal-to-noise ratio. The background is measured using an annulus with inner and outer radius equal to the aperture and twice the aperture radius respectively. It should be noted that on the fifth, sixth and eighth nights the conditions
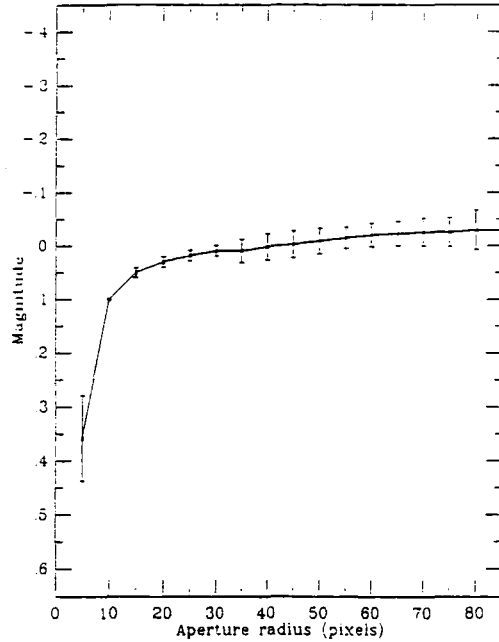
Figure 4.1: A light growth curve in B, FWHM=2″

were not always photometric. On these occasions short exposures of the same targets were subsequently taken in order to calibrate these few non-photometric frames.

The raw magnitudes above have to be corrected to take into account the proportion of photons from the star falling outside of the 5 pixel aperture. This correction depends on the point spread function and therefore on each frame's "seeing". The full width half maximum (FWHM) of the "seeing" profile is estimated by fitting a two-dimensional Gaussian to the bright stellar images. To estimate the magnitude correction, light growth curves (magnitude vs. aperture size diagrams) are constructed for various "seeing" values using several bright stars. A typical blue light growth curve is shown in figure 4.1.

Corrections for atmospheric extinction and exposure time have also to be

taken into account. Then the CCD magnitudes are given by:

$$m_{CCD} = m_{PHOTOM} + 2.5 \ \log T - A(\lambda) \ a \qquad (4.1)$$

where T is the exposure time, and $A(\lambda)$ and a are the atmospheric extinction (in magnitudes per air mass) and the air mass respectively (Hayes and Latham 1975).

As the CCD magnitudes refer to a particular detector + filter spectral response, they have to be transformed to magnitudes refering to a conventional response function; the standard photometric system most often used is that defined in Johnson and Morgan (1953). The relations between CCD and Johnson magnitudes are derived examining the colours of standard stars from the lists of of Graham (1982) and Landolt (1983). We plot the following colour diagrams (figure 4.2)

$$
\begin{aligned}
r - R &= \alpha(B - R) \\
b - B &= \beta(B - R) \\
u - U &= \gamma(U - B)
\end{aligned}
\qquad (4.2)
$$

where U, B denote the Johnson ultraviolet and blue magnitude, R denotes the Cousins red magnitude and u, b, r denote the corresponding CCD magnitudes. Using least squares we find that the coefficients above have values $\alpha = 0.014$, $\beta = -0.118$, $\gamma = -0.009$. From the above set of equations we obtain the following relations for the standard U and B magnitudes:

$$
\begin{aligned}
U &= u - 0.009(u - b) + 0.001(b - r) \\
B &= b + 0.122(b - r)
\end{aligned}
\qquad (4.3)
$$

Therefore, to obtain U and B, the $b - r$ and $u - b$ colours have to be first derived. In most cases where multiple frames of the same target were obtained we use the median magnitude (instead of the mean); this reduces
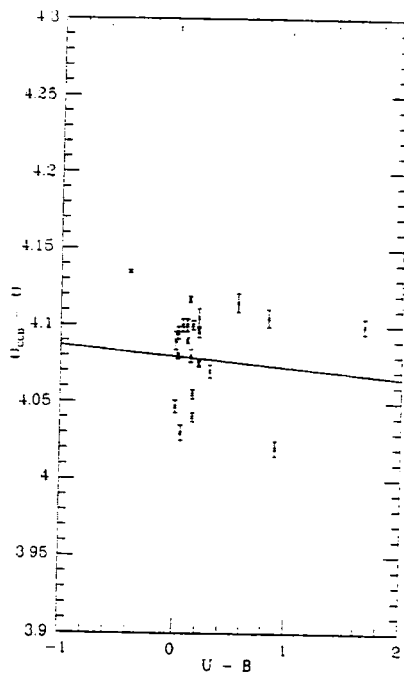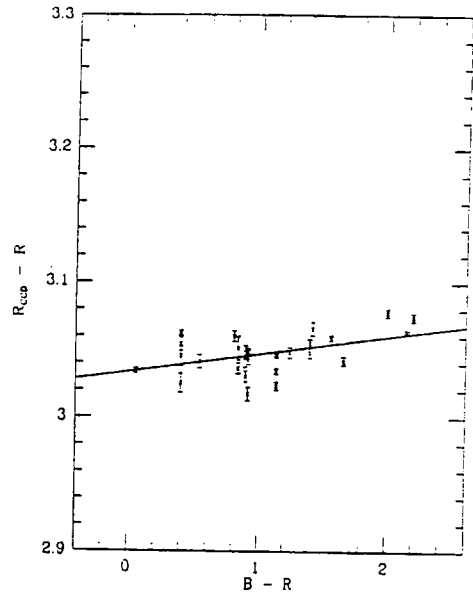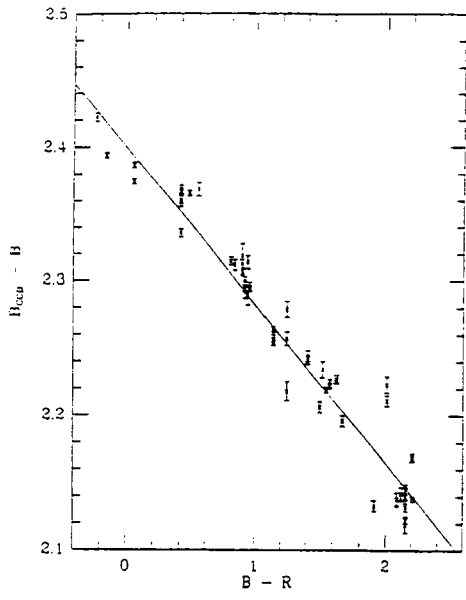
Figure 4.2: Colour correction plots for the standard stars

64

the possibility that outlying CCD observations affect the final magnitude estimation.

Finally, we plot our new Johnson magnitudes versus the old calibrated COS-MOS magnitudes of Boyle et al. (1990); The deviations from a 45° straight line quantify the possible photometric errors of the old calibration. To match the new with the old calibrated magnitudes an automated algorithm is used that transforms the CCD to COSMOS coordinates in order to find the COSMOS counterpart of a given CCD stellar image. Despite the relatively high tolerance value adopted ($\sim 6''$), image mismatching is highly unlikely as we are dealing with high galactic latitude, uncrowded fields. The few exceptional cases, where some crowding of stellar images is present, are individually checked in order to completely rule out the possibility of image mismatching.

4.3   Results

All the information needed for the evaluation of the Boyle *et al.* original calibration is contained in the CCD versus old COSMOS magnitude plots. The B and U plots for all fields are presented in figure 4.3 and 4.4 respectively. A few points relevant to these figures should be elucidated.

We plot the magnitude of a given object as the median over the different exposures. In this way the magnitudes plotted are all independent.

Some outliers discrepant by more than one magnitude can be clearly seen. Their errorbars are small enough that they may be attributed to variable objects.

The error bars are derived as follows. In the case where multiple frames exist
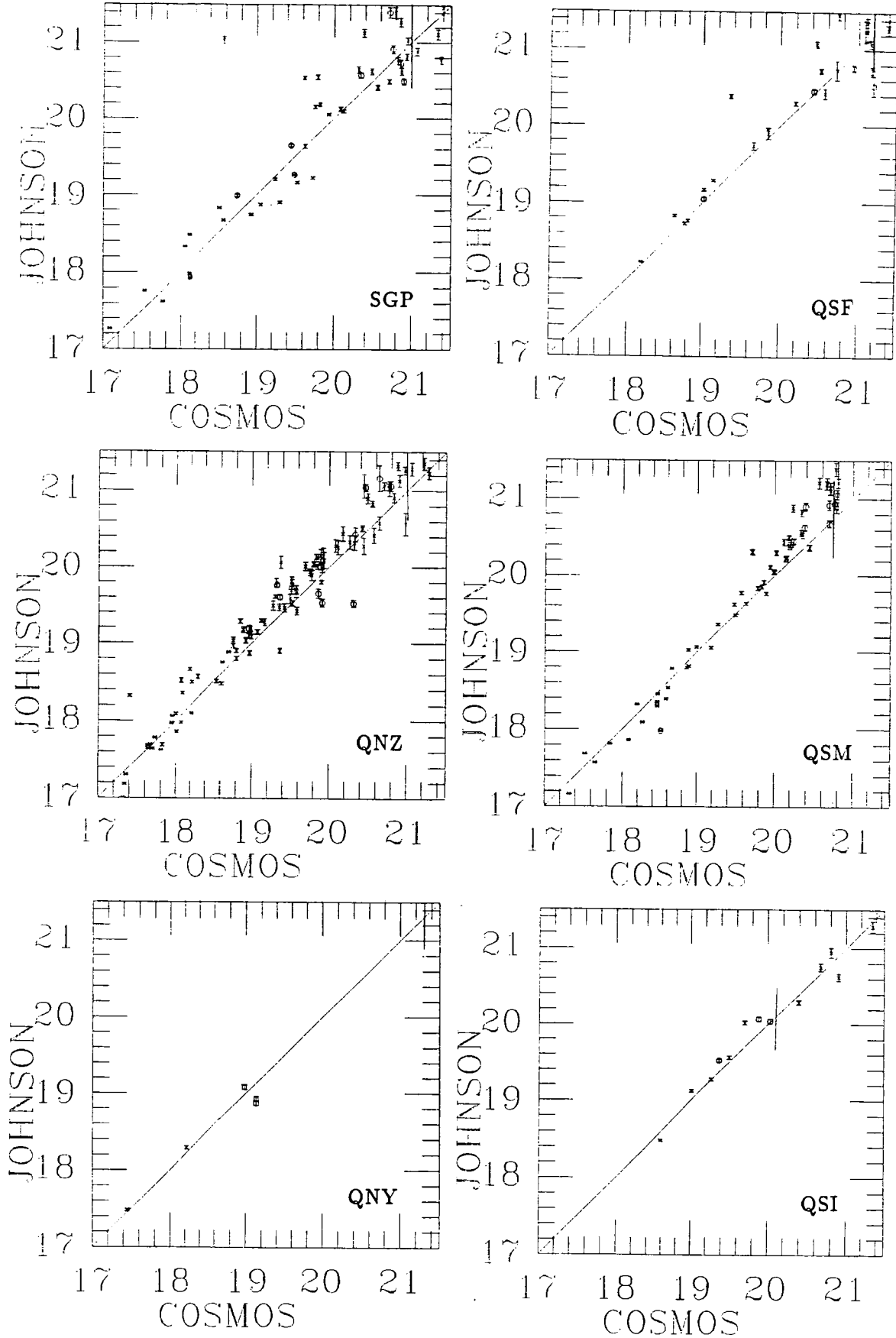
Figure 4.3: New vs. old calibrated B magnitudes for all stars

66
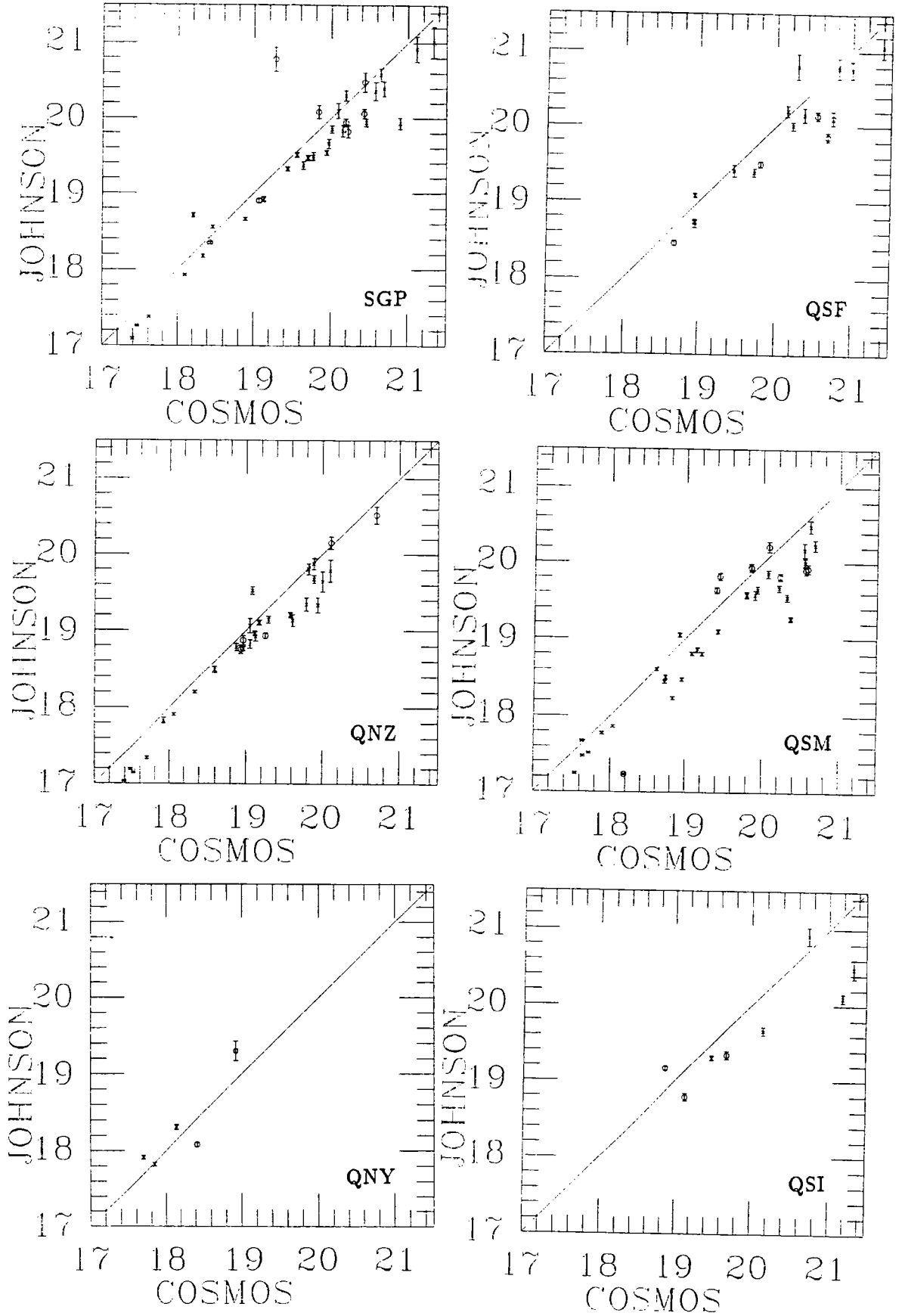
Figure 4.4: New vs. old calibrated U magnitudes for all stars
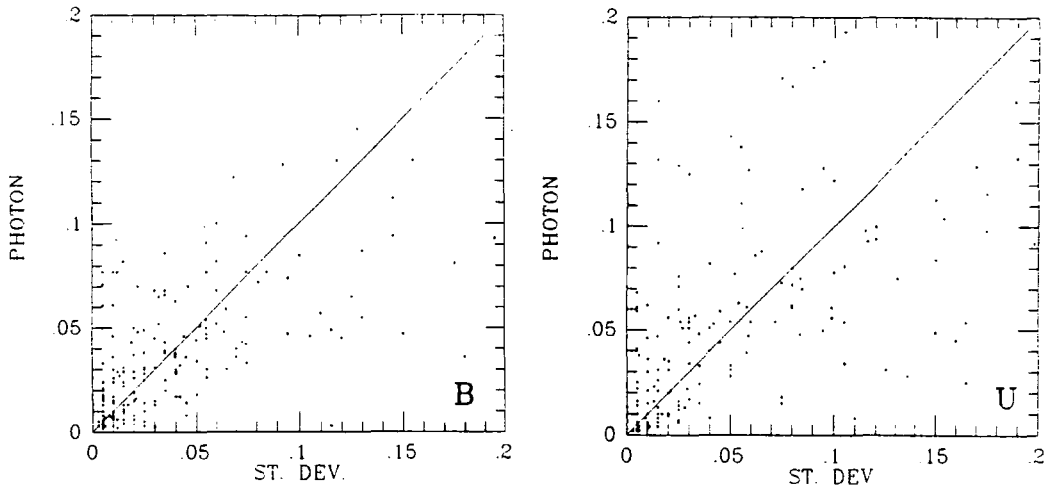
Figure 4.5: Photon noise vs. standard deviation for the multiple frames

the error is the standard deviation of the magnitudes on the different frames. In the very few cases where only one frame was obtained the error was taken to be the photon noise error derived by PHOTOM. Plotting photon noise for the multiple frames against the standard deviation (figure 4.5), we find that there is reasonable agreement between standard deviation and photon noise especially in the blue band. In the vast majority of cases, the frame to frame B magnitude errors are below 0.1 *mag*. In U, the standard deviation-photon noise diagram occasionally shows errors as high as 0.2 *mag*.

Inspection of the magnitude plots reveals that, despite its lack of faint CCD observations, the Boyle et al (1990) calibration is in general accurate. The following notes can be made discussing the fields individually, starting with the blue band.

QSF: The rms errors are low (0.1 mag) for $B < 20^m$ but at fainter magnitudes ($B < 21^m$) increase to 0.2 mag. No significant systematic offset is

present.

SGP: The observed scatter is larger than that found by Boyle *et al.* (1990), with errors of $\sim \pm 0.15$ mag even for the relatively bright ($B < 18^m$) stars. No significant systematic offset is present.

QNZ: In this field where a photoelectric sequence (Arp 1962) was used by Boyle *et al.* (1990), there is a systematic offset of $+0.1^m$ at all magnitudes.

QSM: In contrast to all previous fields, QSM seems to present a scale error (actual magnitudes are fainter than the ones estimated by Boyle *et al.* (1990), with the magnitude of this offset progressively increasing at faint magnitudes. The B magnitudes on this field are corrected using a second order polynomial fit.

QNY: Here the limited number of faint stars does not allow a conclusive photometry test.

QSI: There is a good agreement between the Boyle *et al.* magnitudes and our own even beyond the field's magnitude limit. Again no systematic offset is present.

In all U fields (except QNY) there appears to be a systematic trend; namely, our U magnitudes are found to be brighter when compared with the Boyle *et al.* (1990) calibration. The B and U magnitude offsets together with their errors, estimated on the basis of the CCD magnitude errors, are given in table 4.1. These offsets shift the UVX limits of each field to lower values and introduce some incompleteness.

Taking into account the new UVX limits we attempt to quantify the incompleteness of the Durham QSO survey. The incompleteness can be easily assessed by having knowledge of the relation between U-B and redshift for QSOs. Such a relation was derived by Veron (1983) using a sample of objective prism detected QSOs. The dispersion of the $U - B$-z relation was $\sigma = 0.25$. Originally, the ~ 170 QSOs of the first Durham QSO survey

Table 4.1: U and B offsets for all fields

Field	U_{offset}	error	B_{offset}	error
SGP	-0.20	0.045	-0.002	0.020
QNZ	-0.20	0.050	0.1	0.020
QSF	-0.15	0.040	0.02	0.030
QSM	-0.30	0.030	0.003	0.016
QSI	-0.35	0.040	0.08	0.020
QNY	+0.15	0.035	-0.11	0.030
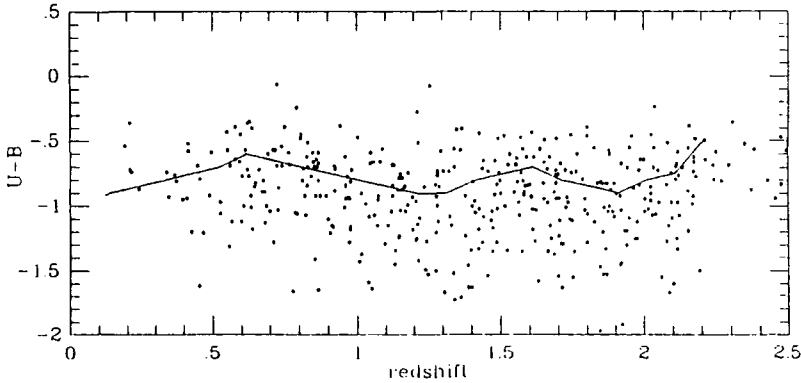
Figure 4.6: U - B colour vs. redshift relation for QSOs

(Boyle *et al.* 1987) were found to agree fairly well with the Veron (1983) relation. However, when comparing with the U-B colours derived here, one obtains a more scattered relation (figure 4.6). The dispersion σ of the U-B versus z relation was estimated in three equal redshifts bins ($z = 0 - 2.2$) on each field separately. The dispersion is similar from field to field for each redshift bin and therefore we can adopt the same value of σ for all fields. We found σ =0.28. 0.34 and 0.33 magnitudes for the three redshift bins respectively. We derive the incompleteness as a function of redshift for each field separately, integrating a Gaussian function around the mean U-B value from $-\infty$ to the U-B limit of each field. The results are presented in
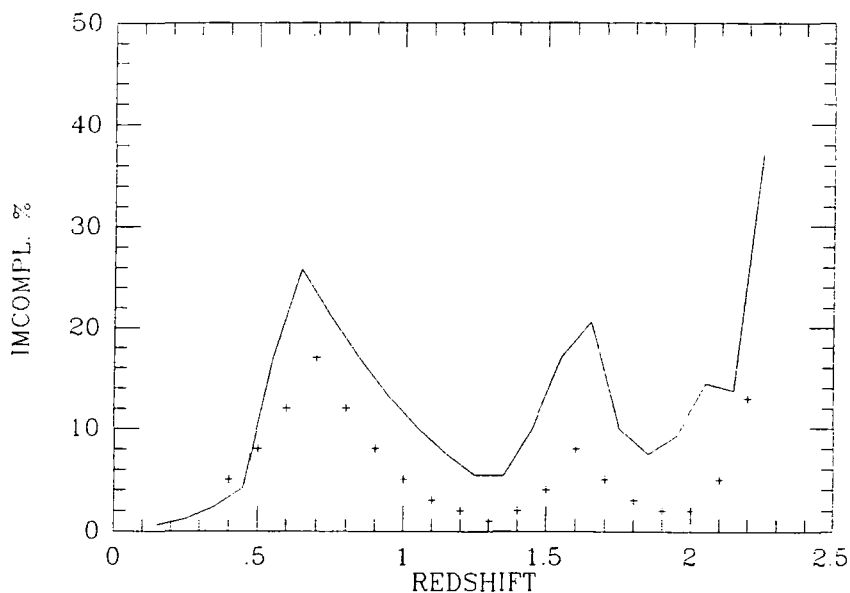
Figure 4.7: Incompleteness vs. redshift for U - B = -0.40 limit (solid line). Crosses represent the Boyle (priv. comm.) points.

table 4.2. In figure 4.7 we plot the survey's incompleteness as a function of redshift using a mean UVX limit of $U - B = -0.4$. On the same figure we compare with the Boyle (priv. comm.) incompleteness estimate. Two peaks are prominent on this diagram at $z \sim 0.7$ and $z \sim 1.6$. The incompleteness around these redshifts is high because the $MgII$ (at $z \sim 0.7$) and the CIV (at $z \sim 1.6$) emission line enter the B band making the QSO ultraviolet excess less prominent.

The mean survey incompleteness over all redshifts can be estimated by weighting the incompleteness-redshift relation with the QSO normalized redshift distribution (Boyle, Shanks and Peterson 1988). We find that the incompleteness is around 10%. The amount of incompleteness is low because the UVX limits of the Durham QSO survey were conservatively chosen.

71

Table 4.2: Incompleteness as a function of redshift for each field

redshift	SGP	QNZ	QSF	QSM	QSI	QNY
0.15	1	0	0	0	2	1
0.25	2	0	0	1	5	2
0.35	3	0	0	2	8	4
0.45	5	0	1	3	13	7
0.55	21	6	10	16	31	23
0.65	32	11	18	25	43	33
0.75	26	8	14	20	37	28
0.85	21	6	10	16	31	23
0.95	16	4	8	12	25	18
1.05	13	3	6	9	20	14
1.15	10	2	4	7	16	11
1.25	7	1	3	5	12	8
1.35	7	1	3	5	12	8
1.45	13	3	6	9	20	14
1.55	21	7	12	16	29	22
1.65	25	9	15	2	34	26
1.75	13	3	6	9	20	14
1.85	10	2	4	7	16	11
1.95	12	3	6	9	17	12
2.05	18	6	10	14	25	19
2.15	17	5	8	13	26	19
2.25	44	19	28	36	56	46

To summarize, since in all fields except QSM, no scale errors were present, the survey's incompleteness will mostly affect the normalization (Φ_*) of the luminosity function (by approximately 10%). Only the QSM field can introduce some magnitude dependent incompleteness. However, inspection of the Boyle, Shanks and Peterson (1988) luminosity function reveals that for an artificial break to be produced the incompleteness at faint magnitudes should rise to $\sim 50\%$. Therefore, we conclude that the small amount of incompleteness detected here cannot affect the form of the luminosity function at faint luminosities.

Chapter 5

The X-ray Background

5.1   Introduction

The straightforward way to estimate the contribution of discrete sources to the X-ray background is to resolve as many sources as possible with a long enough exposure. In this way, Griffiths *et al.* (1988) have estimated that the AGN contribution to the 2 keV background rises to at least 30%. This approach, however, only provides us with information about the contribution of AGN with flux higher than the survey's flux limit, and thus it is only a lower limit to the total AGN contribution.

Alternatively, one may use optical observations. The sky density of optically selected QSOs is $\sim$ 200 deg^{-2} at the $B \sim 22.5^m$ limit of optical observations (Koo, Kron and Cudworth 1986), compared with $\sim$ 30 deg^{-2} for the X-ray surveys (Griffiths *et al.* 1988). Obviously there is more information on number counts and luminosity functions in the optical and this may be used to estimate the AGN contribution even beyond the limiting flux of the existing X-ray surveys. The way to do this is to combine the optical

luminosity function with the relation between the X-ray and optical luminosity. Previous attempts to derive the AGN X-ray emission in this way (e.g. Marshall *et al.* 1983) have been hampered by insufficient knowledge of the optical luminosity function. Recently, the optical luminosity function form and evolution was derived from the Durham QSO survey (Boyle, Shanks and Peterson 1988). Combination of the well constrained QSO luminosity function with the optical to X-ray luminosity relation (Avni and Tananbaum, 1986) based on ~ 200 optically selected QSOs, provides a firm statistical basis for the estimation of the AGN contribution to the X-ray background.

5.2   The X-ray luminosity function

The first step in the estimation of the X-ray emission from AGN is the derivation of the X-ray luminosity function. The X-ray luminosity function can be obtained from the optical luminosity function and the optical to X-ray luminosity relation as follows. The bivariate optical, X-ray luminosity function is

$$\Phi(l_o, l_x) = \Phi(l_o) \ \phi(l_x|l_o) \tag{5.1}$$

where l_o and l_x denote the logarithms of the monochromatic luminosities at 2500 Å and 2 keV respectively; $\phi(l_x|l_o)$ is a conditional probability function expressing the probability that the X-ray luminosity of a QSO with known optical luminosity, l_o, is l_x. To determine the conditional probability function, $\phi(l_x|l_o)$, we only need to know the relation between l_x and l_o, which is usually described through the X-ray to optical spectral index, a_{ox}. To obtain the X-ray luminosity function one integrates the bivariate luminosity function (Eqn. 5.1) over optical luminosity

$$\Phi(l_x)dl_x \ = \ \int \Phi(l_o) \ \phi(l_x|l_o) \ dl_o \ dl_x = \int \Phi(l_o)\phi(a_{ox}|l_o) \ dl_o \ da_{ox}$$

$$= \frac{1}{2.605} \int \Phi(l_o)\phi(a_{ox}|l_o) \; dl_o \; dl_x \qquad (5.2)$$

For a double power law optical luminosity function the X-ray luminosity function has to be derived numerically. To gain some insight in the relation between the optical and the X-ray luminosity function let's consider the simple case where the optical luminosity function is represented by a single power law,

$$\Phi(l_o) = \Phi_* dex[(l_o - l_o^*)(\gamma + 1)] \qquad (5.3)$$

Then if $\phi(l_x|l_o)$ has a simple analytic form, Eqn. 5.2 can be integrated analytically to yield $\Phi(l_x)$.

The simplest possible analytic form would be obtained if the observed a_{ox} values presented negligible scatter around the mean a_{ox} value, $\langle a_{ox} \rangle$. In this case the conditional probability distribution, $\phi(l_x|l_o)$, is a delta function. As $\langle a_{ox} \rangle$ depends on luminosity, l_o, according to the relation $\langle a_{ox} \rangle = A_l l_o + A$ (Avni and Tananbaum 1986) and by definition $a_{ox} = (l_o - l_x)/2.605$, the conditional probability distribution $\delta(a_{ox} - \langle a_{ox} \rangle)$ is written as

$$\delta(a_{ox} - \langle a_{ox} \rangle) = \delta[l_o(\frac{1 - A_l 2.605}{2.605}) - (\frac{l_x + A2.605}{2.605})] \qquad (5.4)$$

Then the X-ray luminosity function can be expressed as

$$\begin{aligned} \Phi(l_x)dl_x &= \frac{1}{2.605} \int \Phi(l_o)dl_o\delta(a_{ox} - \langle a_{ox} \rangle)dl_x \\ &= \Phi_* n dex[((l_x + A2.605 - \frac{l_o^*}{n})(\gamma + 1)n] \; dl_x \qquad (5.5) \end{aligned}$$

where $n = (1 - 2.605A_l)^{-1}$. Avni and Tananbaum (1986) found $A_l = 0.07$ and thus $n \approx 1.2$. From Eqn. 5.5 it is inferred that the slope of the X-ray luminosity function, per unit logarithmic luminosity interval, is $\beta = (\gamma + 1)n$ i.e. steeper than the slope of the optical luminosity function since $n > 1$. Only in the case where $L_x \propto L_o^1$, and thus $n = 1$, have the optical and the X-ray luminosity function equal slopes. According to Eqn. 5.5 the normalization is $\Phi_x^* = \Phi_o^* n$ i.e. higher than the optical.

76

In actuality the conditional probability distribution, $\phi(l_x|l_o)$, presents some dispersion around $\langle a_{ox}\rangle$. Let's assume that at a given optical luminosity, l_o, the a_{ox} distribution around $\langle a_{ox}\rangle$ is well described by a Gaussian with dispersion σ

$$
\begin{aligned}
\phi(a_{ox}|l_o) &= \frac{1}{\sigma\sqrt{2\pi}}e^{-(a_{ox}-\langle a_{ox}\rangle)^2/2\sigma^2} \\
&= \frac{1}{\sigma\sqrt{2\pi}}e^{-[(l_o-n(l_x+2.605A))^2/(2\sigma'^2 n^2)]}
\end{aligned}
\tag{5.6}
$$

where $\sigma' = 2.605\sigma$. Adopting, again for the sake of simplicity, a single power law expression for the optical luminosity function, and substituting Eqn. 5.6 in 5.5, we have for $\Phi(l_x)$

$$
\Phi(l_x) = \frac{\Phi_o^\star 10^{-l_o^\star(\gamma+1)}}{\sigma'\sqrt{2\pi}} \int e^{\left[-[(l_o-n(l_x+2.605A))^2-2(\gamma+1)ln10l_o\sigma'^2 n^2]/2\sigma'^2 n^2\right]}dl_o
\tag{5.7}
$$

To solve this integral analytically, we write the expression within the integral as a Gaussian function of variable l_o. Then $\Phi(l_x)$ becomes

$$
\Phi(l_x) =
\tag{5.8}
$$
$$
\frac{\Phi_o^\star 10^{-l_o^\star(\gamma+1)}}{\sigma'\sqrt{2\pi}}exp[\frac{1}{2}((\gamma+1)ln10\sigma'n)^2 + (\gamma+1)ln10(\frac{l_x+2.605A}{A_l})]
$$
$$
\int_0^\infty exp[-[l_o - ((\gamma+1)\ln 10(\sigma'n)^2 + (\frac{l_x+2.605A}{A_l})]^2/2\sigma'^2 n^2]dl_o
\tag{5.9}
$$

Integration is now straightforward and yields

$$
\Phi(l_x) = \frac{\Phi_o^\star}{2\sigma'\sqrt{2}}e^{\frac{1}{2}((\gamma+1)ln10\sigma'n)^2 - ln10l_o^\star(\gamma+1)}10^{(\gamma+1)n(l_x+2.605A)}
\tag{5.10}
$$

From this expression it can be seen that the X-ray luminosity function is a power law with slope $\beta = (\gamma+1)n$, i.e. steeper than the optical luminosity function slope, given that $L_x \propto L_o^{0.8}$. The normalization of the X-ray luminosity function strongly depends on the dispersion σ' of the $\phi(l_x|l_o)$ conditional probability distribution; the higher the dispersion the higher the power law normalization. As of course the area under the luminosity function remains the same, only the normalization at high luminosities increases as low luminosity objects move to the high luminosity part of the

77
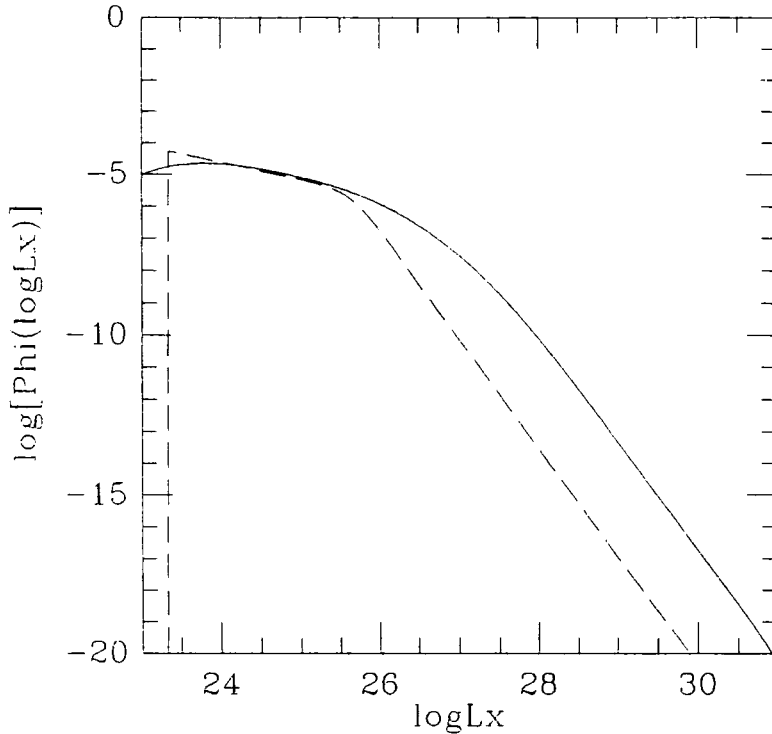
Figure 5.1: The 2 keV X-ray luminosity function, predicted from the Boyle, Shanks and Peterson optical luminosity function, using dispersion $\sigma = 0.2$ and $a_{ox} = 0.07l_o - 0.62$

luminosity function for large σ values; this results in the decrease of the low luminosity part of the luminosity function. This can be visualized in figure 5.1 where a double power law, X-ray luminosity function is plotted for $\sigma = 0$ and $\sigma = 0.2$.

To evaluate the AGN emissivity the evolution of the X-ray luminosity function has to be derived. The X-ray luminosity evolution can be evaluated by combining the optical luminosity evolution with the X-ray to optical luminosity relation (Avni and Tananbaum 1982). The relation between optical and X-ray luminosity is non-linear, $L_x \propto L_o^b$, with $b = n^{-1} = 1 - 2.605A_l$. At redshift z the X-ray luminosity is

$$L_x(z) \propto L_o^b(z) = (L_o(0)(1 + z)^{k_o})^b \propto L_x(0)(1 + z)^{k_o b} \qquad (5.11)$$

For $k_o = 3.2$ (Boyle Shanks and Peterson 1988) and $b = 0.8$ (Avni and Tananbaum 1986) one obtains $L_x(z) \propto L_x(0)(1 + z)^{2.5}$. This means that the X-ray luminosity evolves at a slower rate than the optical luminosity (Avni and Tananbaum 1982).

Now the X-ray background intensity, I (flux per unit solid angle), from AGN can be easily calculated. Let $j(E_e)$ denote the AGN emissivity (luminosity per unit volume) at energy E_e. The X-ray flux observed at energy $E_o = E_e(1 + z)^{-1}$ originating from volume dV is

$$f(E_o) = \frac{j(E_o)dV}{4\pi d_L^2(z)} \tag{5.12}$$

$d_L(z)$ is the luminosity distance and dV is the comoving volume element. For an assembly of sources with differential luminosity function at redshift z, $\Phi(L, z)$ the emissivity is

$$j(E_e) = \int \Phi(L, z)L dL \tag{5.13}$$

We need to refer to a standard restframe energy E_o at all redshifts. The emissivities at energies E_e and E_o are related through $j(E_e) = j(E_o)(1 + z)^{-a_x+1}$, with a_x denoting the X-ray spectral index ($f \propto \nu^{-a_x}$). Combination of Eqn. 5.12, 5.13 and of the volume element expression (Weedman 1986) yields for the X-ray background intensity

$$I = \frac{c}{H_o} \int_0^{z_{max}} \int_0^\infty \frac{\Phi(L, z)\, L}{(1 + z)^{2+a_x}\sqrt{1 + 2q_o z}} dL\, dz \tag{5.14}$$

The following points are emphasized. The intensity does not depend on the Hubble constant H_o: luminosity L depends on H_o as $L \propto H_o^{-2}$ due to the inverse square law; the luminosity function depends on volume V and hence $\Phi(L)dL \propto r^{-3} \propto H_o^3$. Then from Eqn. 5.14 it follows that $I \propto H_o^{-1}\Phi(L)dL \propto H_o^{-1}H_o^3 H_o^{-2}$ i.e. independent of H_o. This is very convenient as the predicted AGN X-ray intensity does not involve the observational uncertainties associated with the determination of H_o.

79

The AGN X-ray emission is very sensitive to the X-ray spectral index. This is because at higher redshifts we observe progressively higher rest frame energies. A flat (hard) X-ray spectrum carries more luminosity at high energies and this translates to strong AGN X-ray emission. In contrast a steep X-ray spectral index suppresses the X-ray emission of high redshift objects.

The intensity is sensitive to the dispersion, σ, of the $\phi(l_x|l_o)$ distribution. To understand this let's consider the simple case where the optical luminosity function is a delta function and the conditional probability distribution $\phi(l_x|l_o)$ is a Gaussian of dispersion σ. Then the X-ray luminosity function and the emissivity are not Gaussian but skewed towards higher luminosities. The reason is merely that the $\phi(l_x|l_o)$ distribution is a Gaussian around $\langle \log L_x \rangle$ and not around $\langle L_x \rangle$. The skewness of the L_x distribution around $\langle L_x \rangle$ increases with dispersion. As a consequence, a high dispersion σ translates to a high value of the emissivity j. Combination of the optical luminosity function and the relation between X-ray and optical luminosity without taking into account the observed dispersion will underestimate the X-ray emission.

5.3 The X-ray Number Counts

Before we use the predicted X-ray luminosity function to evaluate the X-ray emission from AGN we have to check that this luminosity function is in agreement with the existing X-ray observations. Previous attempts to check the consistency between X-ray and optically selected samples have been performed by Franceschini *et al.* (1986) and Avni and Tananbaum (1986); using the then available optical luminosity function, they found that the predicted X-ray number counts far outnumbered the observed ones. The available X-

ray data consist mainly of bright luminosity sources populating the steep power law part of the X-ray and optical luminosity functions. As the bright part of the Durham optical luminosity function agrees with the previous optical luminosity functions used by Franceschini et al. (1986) and Avni and Tananbaum (1986), we do not expect here to obtain strikingly different results. Rather, the reason we evaluate the exact discrepancy between the X-ray and optically selected samples is to adjust our X-ray luminosity function so that it agrees with the observed X-ray data. More specifically we test which form of the a_{ox} distribution gives good agreement between the predicted and observed X-ray luminosity and redshift distributions.

The most appropriate test is to bin the X-ray data in luminosity and redshift; then the agreement of the observed and predicted number of objects in each bin could be evaluated using a χ^2 test. However, the limited amount of X-ray data available does not allow for such a detailed test. The most obvious X-ray sample to be compared with our predictions is the Medium Sensitivity Survey (MSS) sample (Maccacaro et al. 1984, Gioia et al. 1984) which contains only 23 QSOs. The simplest test we can perform with such low numbers is merely to compare the total number of objects observed and predicted. We restrict comparison to QSOs. Low luminosity AGN are excluded because our predicted X-ray luminosity function is based on the QSO optical luminosity function whereas the MSS contains many low luminosity AGN with reddish colours (Stocke et al. 1983) which are not represented in the colour selected optical luminosity function. In estimating the predicted QSO number we use the detailed flux limit of the MSS as a function of sky coverage given in Gioia et al. (1984). We predict 1.1 sources deg^{-2} in comparison with 0.26 ± 0.05 sources deg^{-2} observed. This large discrepancy was also noted by Avni and Tananbaum (1986) and Franceschini et al. (1986). Let's consider some possible reasons that could account for the observed discrepancy.

A first possibility is that X-ray and optical surveys do not sample the same parent population. For instance, there could be a class of X-ray quiet QSOs in analogy with radio quiet QSOs. This issue can in general be addressed by inspection of the a_{ox} vs. L_o diagram; if some QSOs are actually X-ray quiet then on the $a_{ox} - L_o$ diagram the a_{ox} upper limits should form a separate sequence from the X-ray loud QSO locus. Such a trend is not observed on the $a_{ox} - L_o$ diagram. Kriss and Canizares (1985), using a sample of 177 AGN, found that the probability that the non X-ray detected, optically selected AGN are drawn from the same population as the ones with X-ray detections is 90%. (However, if QSOs only are considered this probability falls to $\sim 60\%$). Avni and Tananbaum (1986) confirmed this finding using a large (~ 150 QSOs) sample. These results probably suggest that X-ray quiet QSOs, if they exist, constitute a small part of the QSO population.

Another plausible reason to account for the observed and predicted X-ray number count discrepancy could be that soft X-ray surveys might fail to detect some AGN e.g. due to absorption. Maccacaro and Gioia (1986) examined the possibility of strong galactic absorption. They found a mean hydrogen column density of $N_H = 3 \times 10^{20} \mathrm{cm}^{-2}$ towards the MSS fields and therefore excluded this possibility. On the other hand QSOs do not seem to present large intrinsic absorption. While some low luminosity AGN present considerable amount of absorption (Turner and Pounds, 1989), the QSO spectra are consistent with zero intrinsic column densities (Tananbaum et $al.$ 1986, Wilkes and Elvis 1987). Therefore, it is unlikely that absorption, galactic or intrinsic, could affect the observed QSO X-ray number counts.

The remaining possibility is that we made some wrong assumptions in the derivation of the X-ray luminosity function. Our assumptions involved the form and evolution of the optical luminosity function and the form of the a_{ox} distribution. While the former is well constrained, this is not the case

for the latter. Avni and Tananbaum (1986) found some indication for an a_{ox} distribution skewed towards high a_{ox} values, i.e. low X-ray luminosities. They pointed out that the discrepancy between the predicted and observed number counts is relaxed in the case of such a skew a_{ox} distribution. Franceschini *et al.* (1986) have shown that the discrepancy between predictions and observations disappears for values of the dispersion σ lower than the observed $\sigma = 0.2$. In agreement with their result, we find that for $\sigma = 0.12$ the total number of QSOs predicted equals the number observed in MSS. In the case of the skew distribution found by Avni and Tananbaum (1986), agreement is obtained for dispersion $\sigma = 0.14$. To explore further the effects of dispersion we construct the predicted redshift and luminosity distributions for the Gaussian and the skew distribution model for different values of dispersion. This skew distribution can be represented by two half Gaussians of width σ_L and σ_R glued together at their maxima (Avni and Tananbaum 1986). Thus the distribution of $r \equiv a_{ox} - \langle a_{ox} \rangle$ is described by

$$f(r) = H exp[-\frac{1}{2}(\frac{r-d}{\sigma})^2] \qquad (5.15)$$

where $\sigma = \sigma_L$ for $r \leq d$ and $\sigma = \sigma_R$ for $r \geq d$. The relation between the σ_L, σ_R and H parameters is defined by the following equations

$$
\begin{aligned}
H &= \frac{1}{\sqrt{2\pi}}\frac{2}{\sigma_L + \sigma_R} \\
d &= -\sqrt{\frac{2}{\pi}}(\sigma_R - \sigma_L) \\
\sigma^2 &= (1 - \frac{2}{\pi})(\sigma_L^2 + \sigma_R^2) + (\frac{4}{\pi} - 1)\sigma_L\sigma_R \qquad (5.16) \\
\sigma_L &= \sigma[(1 - \frac{2}{\pi})(R^2 + 1) + (\frac{4}{\pi} - 1)R]^{-1/2} \\
\sigma_R &= \sigma R[(1 - \frac{2}{\pi})(R^2 + 1) + (\frac{4}{\pi} - 1)R]^{-1/2}
\end{aligned}
$$

with $R = \sigma_R/\sigma_L$. Thus two parameters are sufficient to define the skew distribution; R and σ to measure the skewness and dispersion respectively. The predicted and observed redshift and luminosity distributions are shown
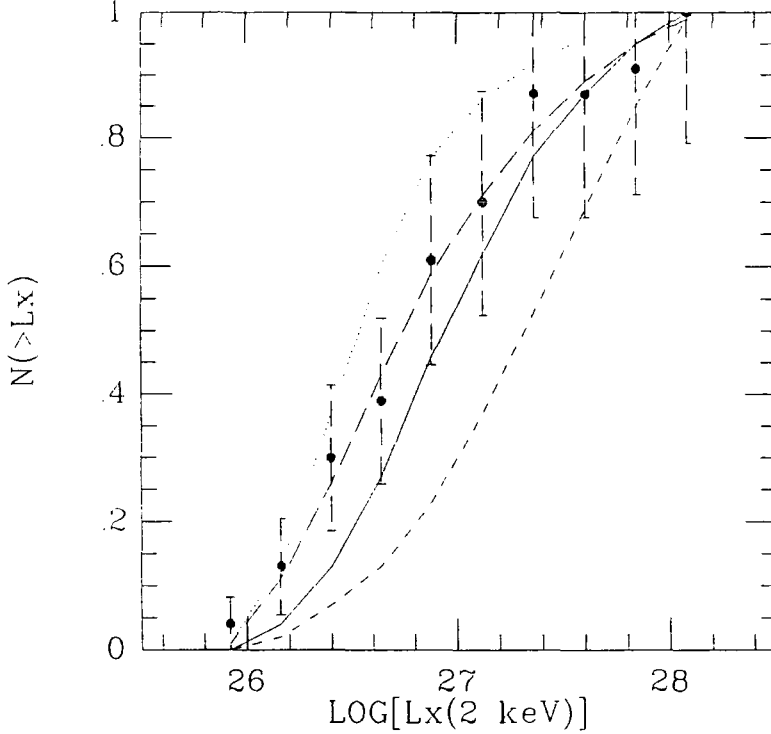
Figure 5.2: The predicted and observed cumulative luminosity distribution for various a_{ox} models. Filled circles: the MSS observations; solid line: skew a_{ox} distribution with $R = 3.3$ and $\sigma = 0.21$; long dash: skew distribution with $\sigma = 0.12$; dotted line: Gaussian a_{ox} distribution with $\sigma = 0.14$; short dash: Gaussian distribution with $\sigma = 0.2$

in figures 5.2 and 5.3 respectively. Comparison by eye suggests that a low dispersion ($\sigma = 0.12$) Gaussian model provides an acceptable fit to the data.

Nevertheless, before adopting a low σ value one has to understand how it could be possible to reduce arbitrarily the dispersion, σ, which is after all an observed quantity. The argument is simply that the a_{ox} distribution could be broadened due to the presence of noise. This noise, σ_n, has to be subtracted from the observed σ in order to obtain the intrinsic a_{ox} dispersion, σ_{in}, which reflects the true physical properties of the AGN central engine. Therefore in the convolution of the optical luminosity function and the a_{ox} conditional probability distribution, the intrinsic dispersion should
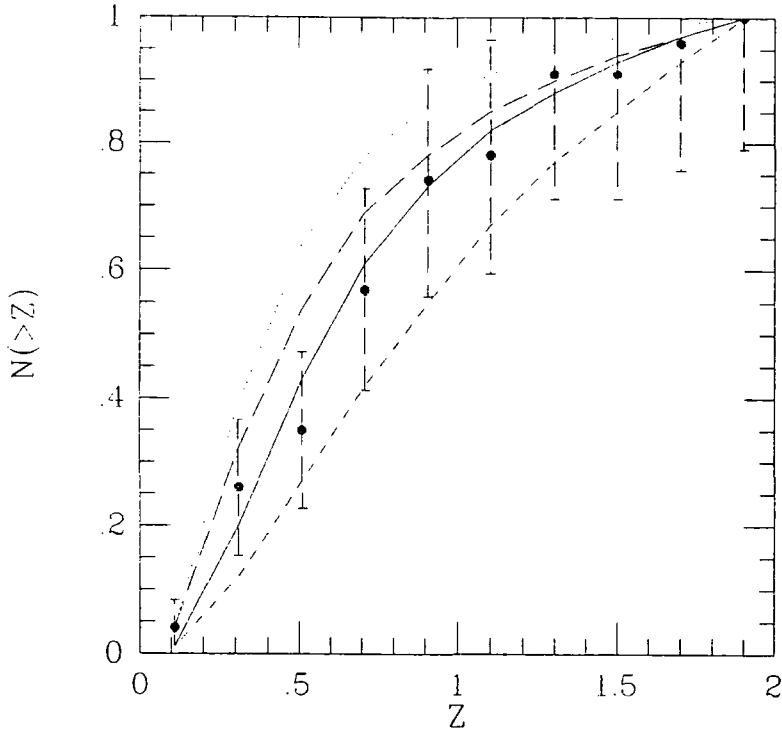
Figure 5.3: The predicted and observed cumulative redshift distribution for various a_{ox} models. Filled circles: the MSS observations; solid line: skew a_{ox} distribution with $R = 3.3$ and $\sigma = 0.21$; long dash: skew distribution with $\sigma = 0.12$; dotted line: Gaussian a_{ox} distribution with $\sigma = 0.14$; short dash: Gaussian distribution with $\sigma = 0.2$

well errors in the derivation of luminosities arising from the uncertainty in spectral indices.

Quadratic summation of the noise due to the effects above yields a value for the total noise of $\sigma_n \approx 0.1$. It is difficult to envisage how the total noise could amount to $\sigma_n \approx 0.14$ which is the value required to bring in agreement the data with the predictions. However, Einstein (Griffiths et al. 1988) and, recently, ROSAT results (Georgantopoulos et al. 1991, Shanks et al. 1991) from X-ray selected QSO samples give a value $\sigma \sim 0.1$ for the observed dispersion. This could suggest that dispersion is a function of luminosity with brighter QSOs having lower values of dispersion. Intrinsic photoelectric

from X-ray selected QSO samples give a value $\sigma \sim 0.1$ for the observed dispersion. This could suggest that dispersion is a function of luminosity with brighter QSOs having lower values of dispersion. Intrinsic photoelectric absorption could block some of the soft X-ray emission, resulting in the broadening of the a_{ox} distribution for an optically selected sample. The uncertainty in the form of the a_{ox} distribution has some impact on the size of the AGN contribution to the X-ray background.

5.4   The AGN X-ray emission

The optical QSO luminosity function is well constrained in the redshift range $z < 2.2$ where QSOs can be selected due to their abnormally low $U - B$ colour. At $z \sim 2.2$ the Lyα line enters the B band, reddening the $U - B$ colour and thus rendering QSOs non UVX. Other techniques have to be employed to detect high redshift, $z > 2.2$, QSOs. For example in objective prism surveys QSOs are discovered by their strong emission lines (Weedman 1986a) whilst in multicolour surveys several colours are used to distinguish QSOs from the stellar locus (see Warren *et al.* 1988). Despite the use of these techniques the QSO luminosity function at high redshifts is highly uncertain. Work by Schmidt *et al.* (1987) and Warren *et al.* (1988) has shown that there is scarcity of QSOs beyond $z \sim 2.5$. It is not certain if this number decline reflects changes in the spatial density of QSOs or if it just represents an apparent cut-off due to the presence of dust associated with e.g. primeval galaxies. Indeed, dust could absorb the optical radiation while leaving unaffected the hard X-ray radiation. In other words QSOs, not detected in optical surveys could contribute significantly to the X-ray intensity (Heizler and Ostriker 1988). In our calculations we take into account this possibility. We distinguish between the following models: in

the first model the $z < 2.2$ luminosity function evolves according to Pure Luminosity Evolution up to the redshift formation $z_{max} \sim 4$. In the other model we assume that the luminosity function evolution stops at $z \approx 2.5$, with the luminosity function preserving its form and normalization at higher redshifts.

As already discussed, the predicted intensity is sensitive to the choice of X-ray spectral index, a_x. The results on the AGN X-ray spectral index are as yet inconclusive. The X-ray spectrum of low luminosity AGN can be represented with a power law of slope $a_x \sim 0.7$ at energies > 1 keV (Turner and Pounds 1989). On the other hand, radio quiet QSOs seem to present steeper spectra in the same energy range (Canizares and White 1989, Wilkes *et al.* 1989). Maccacaro *et al.* (1988) studied the spectra of both low luminosity AGN and QSOs in the energy range 0.3-3.5 keV. They showed that the mean spectral index is $a_x = 1.03$. In order to investigate the effect of the spectral index on the predicted X-ray intensity we distinguish between two cases, namely $a_x = 0.7$ and $a_x = 1$. However, dealing here with the contribution of both low luminosity AGN and QSOs we believe that we obtain a more realistic estimate of the AGN X-ray emission for $a_x \approx 1$.

We choose a low luminosity cut-off for the luminosity function corresponding to $M_B \approx -15$. In this way we include low luminosity AGN as Seyfert galaxies in our estimation. Anyway, the choice of a low luminosity cut-off does not affect significantly our calculations. Altering the cut-off from $M_B = -15$ to -21 reduces the AGN X-ray emission at 2 keV by less than 20%. This is because for a double power law luminosity function with flat faint slope, the bulk of the contribution comes from luminosities around the characteristic luminosity, L_*.

In our calculations there are two inherent assumptions. First, we assume

Table 5.1: The fractional AGN contribution to the 2 keV X-ray background for Pure Luminosity Evolution models

	$a_x = 1$		$a_x = 0.7$	
	$z_c = 2.5$	$z_c = 4$	$z_c = 2.5$	$z_c = 4$
$R = 3.3, \sigma = 0.21$	0.60	0.64	0.75	0.82
$R = 3.3, \sigma = 0.14$	0.43	0.46	0.54	0.59
$R = 1, \sigma = 0.2$	0.66	0.72	0.84	0.93
$R = 1, \sigma = 0.12$	0.38	0.45	0.53	0.59

that there is continuity between the properties of low luminosity AGN and QSOs. In other words, we assume that the QSO luminosity function evolved back to $z \sim 0$ describes adequately the low luminosity AGN luminosity function. Indeed, this was demonstrated previously by comparison of the luminosity functions of Seyfert galaxies and QSOs. Second, we assume that the relation between optical and X-ray luminosity derived by Avni and Tananbaum (1986) for QSOs applies to low luminosity AGN as well. Despite the fact that a_{ox} in low luminosity AGN can be affected by contamination from the host galaxy starlight and by large intrinsic absorption (Kriss and Canizares 1985), it appears that a_{ox} follows the same relation as in QSOs (Kriss and Canizares 1985, Mushotzky and Wandel 1988, Kruper and Canizares 1989). We use four different forms for the a_{ox} distribution: a skew distribution, $R = 3.3$, with dispersion $\sigma = 0.21$ as derived by Avni and Tananbaum (1986); a Gaussian distribution with $\sigma = 0.2$; a skew distribution with $\sigma = 0.14$; and a Gaussian with $\sigma = 0.12$. These latter two are the values of dispersion required to bring into agreement the predicted and observed X-ray luminosity and redshift distributions. The coefficients A_l and A of the relation $\langle a_{ox} \rangle = A_l l_o + A$ for both the Gaussian and the skew distribution are given in Avni and Tananbaum (1986). The results are

Table 5.2: Mean and standard deviation of the AGN X-ray emission parameters.

A_o	-0.62	0.03
σ	0.20	0.02
a_x	1.0	0.03
β	1.44	0.20

presented in table 5.1. The following points are stressed.

AGN cannot produce the whole of the 2 keV X-ray background intensity. Only in the extreme case where the X-ray spectral index was relatively flat ($a_x = 0.7$), the luminosity evolution continued up to $z \sim 4$ and the a_{ox} dispersion was high did AGN produce the bulk of the X-ray intensity. However, this cannot be the case since it was shown earlier that comparison between predicted and observed number counts rules out a Gaussian high dispersion ($\sigma = 0.2$) model. For more realistic forms of the a_{ox} distribution the contribution of AGN seems to amount to $\sim 50\%$ of the observed intensity.

The error on this figure can be estimated using Monte Carlo simulations. We assign random values to the parameters A_o and dispersion σ of the a_{ox} distribution, the X-ray spectral index a_x and the faint end slope, (β), of the optical luminosity function. The parameters above are assumed to follow Gaussian distributions with mean and standard errors as given in table 5.2 (Avni and Tananbaum 1986, Anderson and Margon 1987, Maccacaro *et al.* 1988, Boyle Shanks and Peterson 1988). One hundred simulations of the predicted X-ray intensity are created in this way, yielding a standard error for the AGN fractional contribution $\sim \pm 0.25$.
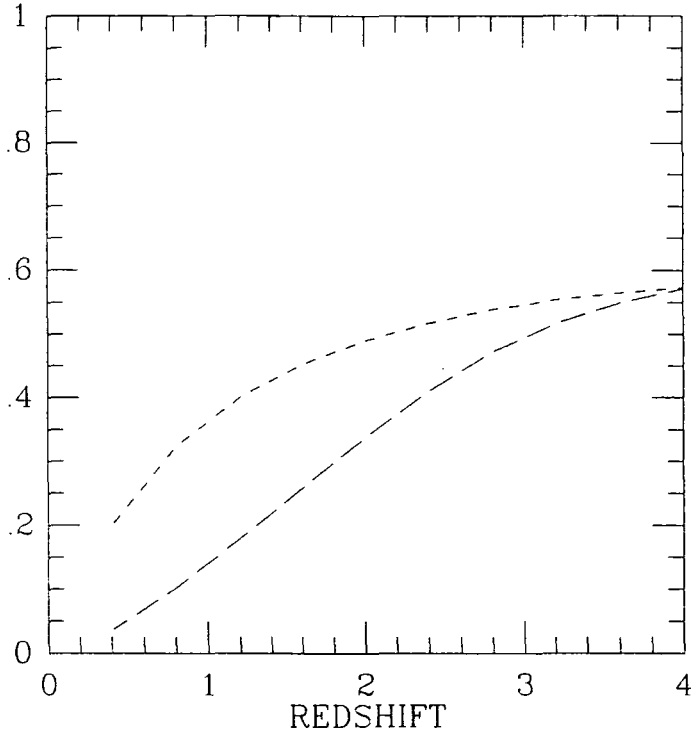
Figure 5.4: The X-ray emission arising from low luminosity AGN ($M_B >$ -23) (short dash) and QSOs ($M_B < -23$) (long dash), with redshift lower than z as a fraction of the total AGN emission

case where $R = 3.3$ and $\sigma = 0.21$ the difference between the X-ray emission when evolution stops at $z_c = 2.5$ and 4 amounts to only 4% of the X-ray background intensity. Therefore, dust obscured QSOs at high redshifts cannot be significant contributors to the X-ray background. This is at odds with the predictions of Heizler and Ostriker (1988).

It is interesting to see from which redshifts the bulk of the AGN X-ray emission emanates. In figure 5.4 we plot the fraction of the total AGN 2 keV X-ray intensity arising from redshifts lower than z. It can be seen that almost two thirds of the X-ray emission comes from redshifts $z < 2$. Note that in the case of a hypothetical no evolution model ($k_o = 0$) all emission would arise from $z < 1$. To understand better the redshift dependence of the X-ray emission, consider the simplest case where all of the X-ray emission

almost two thirds of the X-ray emission comes from redshifts $z < 2$. Note that in the case of a hypothetical no evolution model ($k_o = 0$) all emission would arise from $z < 1$. To understand better the redshift dependence of the X-ray emission, consider the simplest case where all of the X-ray emission arises from AGN with luminosities around the break luminosity, $L_\star$; $L_\star$ evolves with redshift as $L_\star(z) = L_\star(z)(1+z)^{2.5}$; therefore the intensity from redshift z is, according to Eqn. 5.14,

$$I(L_\star, z) = \Phi_\star L_\star(z)(1 + z)^{-(2.5+a_x)} = \Phi_\star L_\star(0)(1 + z)^{-a_x} \qquad (5.17)$$

which tells us that the X-ray emission decreases with redshift, purely as a function of the X-ray spectral index a_x. We also plot in figure 5.5 the fraction of the observed 2 keV intensity arising from redshift lower than z, separately for low luminosity AGN and QSOs. QSOs and AGN contribute equally to the 2 keV X-ray background (cf Setti 1990).

Next, we explore the effect of intrinsic absorption on our estimates of the AGN X-ray emission. Many low luminosity AGN present strong absorption (Lawrence and Elvis 1982, Mushotzky 1982, Petre et $al.$ 1984, Reichert et $al.$ 1985, Elvis and Lawrence 1985, Turner and Pounds 1989). Thus at low redshifts intervening material is expected to block the soft X-rays, reducing the AGN contribution to the X-ray background. It is difficult to make any detailed prediction for the effect of such intrinsic absorption because there is not an exact correlation between X-ray luminosity and hydrogen column density N_H. While some AGN present N_H higher than $10^{23} \mathrm{cm}^{-2}$ others present no absorption at all (Turner and Pounds 1989). Here we consider a simple model where all low luminosity AGN with $L_x < 3 \times 10^{43}$ erg sec^{-1} (2-10 keV) have hudrogen column densities of 10^{22} cm^{-2}; this value is higher than the typical value of N_H in Seyfert galaxies as can be seen from figure 9 of Turner and Pounds (1989). We use the photoelectric absorption cross section, $\sigma(E)$, derived by Morrison and McCammon (1983). Even adopting

91
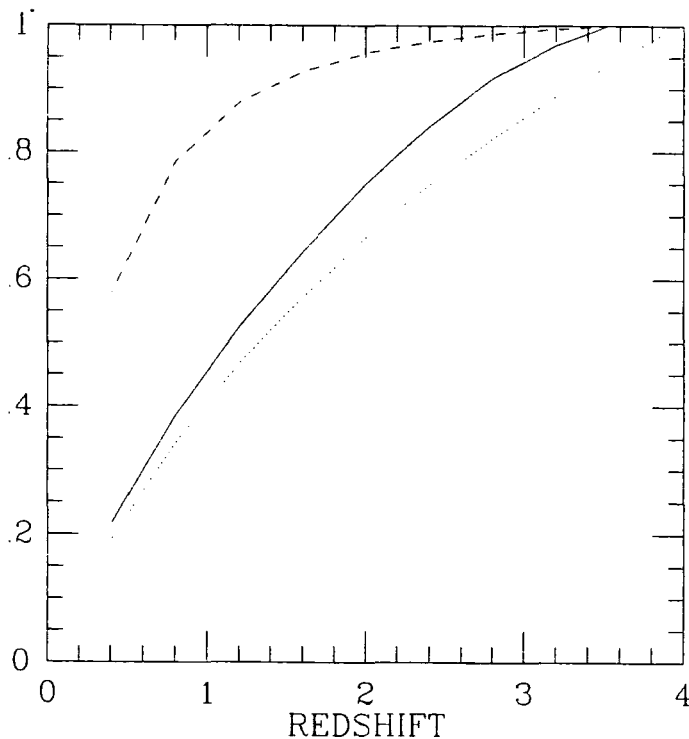
Figure 5.5: The fraction of the total 2 keV X-ray intensity from AGN, arising from redshifts lower than z, for different evolution models. Solid line: pure luminosity evolution stops at z=2.5. Dotted line: pure luminosity evolution continues up to the redshift of source formation $z_{max} = 4$. Dash: Hypothetical model of no evolution ($k = 0$). In all three models a Gaussian a_{ox} model, ($\sigma = 0.12$), and a spectral index, $a_x = 1$, are adopted.

this high value of N_H, we find that absorption has a very small effect on the AGN 2 keV X-ray emission (the X-ray emission is affected by less than 10%). This small effect is due to the fact that absorption is important only at low redshifts. At higher redshifts we observe higher restframe energies which are not susceptible to absorption because the photoelectric absorption cross section rapidly falls with energy.

For the sake of completeness we estimate the AGN X-ray emission on the basis of Luminosity Dependent Density Evolution (LDDE) models as well. Although the results from the optical QSO surveys are strongly in favour

of PLE models, there are two problems with this interpretation. First, if QSOs are not short lived, there is a problem with the creation of super-massive black holes. Second, there is evidence that radio loud QSOs do not follow a PLE pattern (Peacock 1986, Yee and Green 1988). (However, note that more recent data, Peacock priv. comm., do not appear to rule out PLE models). These reasons urged Schmidt and Green (1986) to propose a LDDE model, where the rate of evolution depends on source luminosity, i.e. low luminosity QSOs increase in number with redshift, at a slower rate than the luminous ones.

Based on the Palomar BQS survey, Schmidt and Green (1983) constructed a LDDE model for the optical luminosity function; according to Green (1988) new results from the faint QSO surveys proved that the original parameterization of the Schmidt and Green (1983) luminosity function gave too strong an evolution for high luminosities and too weak for low luminosities. Taking into account the new results, Green (1988) proposes a LDDE model with the following parameterization:

$$\Phi(l_o, z) = \Phi(l_o, 0) exp[0.78(-17.13 + 2.5l_o - c)\tau] \qquad (5.18)$$

for $H_o = 50$ km sec^{-1} Mpc^{-3} and $\Omega = 1$. In the last expression τ denotes the fractional look-back time, l_o is, as usual, the monochromatic luminosity at 2500 Å and c is the constant of the M_B to l_o relation (Marshall et al. 1984). The local QSO luminosity function $\Phi(l_o, 0)$, is given in Boyle, Shanks and Peterson (1988). We use the skew a_{ox} distribution with $\sigma = 0.21$, described before, and a Gaussian with $\sigma = 0.20$. We do not use the lower dispersion models since they were derived on basis of the PLE model and thus are not applicable here. We use a low luminosity cut-off of $M_B \approx -15$. The redshift of source formation is chosen at $z_{max} = 4$. We distinguish, as in the case of PLE, between two different models for high redshift evolution: in the first case evolution ceases at $z_c = 2.5$, while in the other case evolution

Table 5.3: The fractional AGN contribution to the 2 keV X-ray background for Luminosity Dependent Density Evolution models

	$a_x = 1$		$a_x = 0.7$	
	$z_c = 2.5$	$z_c = 4$	$z_c = 2.5$	$z_c = 4$
$R = 3.3, \sigma = 0.21$	0.67	0.68	0.83	0.84
$R = 1, \sigma = 0.2$	0.74	0.75	0.92	0.93

continues up to $z_c = 4$. The results are presented in table 5.3. It can be seen that the AGN emission in the case of LDDE models is comparable with the one predicted for PLE models. Note that the results do not depend on the choice of evolution redshift cut-off z_c. Indeed, the contribution of QSOs with luminosity L_* at redshift z is

$$I(L_*, z) = e^{4\tau}(1 + z)^{-(2.5+a_x)}(\Phi_* L_*) \qquad (5.19)$$

As a result of the competition between the $e^{4\tau}$ and the $(1 + z)^{-(2.5+a_x)}$ term the bulk of the AGN contribution comes from low to moderate redshifts.

Finally, for comparison, we make an evaluation of the AGN X-ray emission based on the local luminosity function of X-ray selected low luminosity AGN (Schmidt and Green 1986). This luminosity function is derived by means of 20 Seyfert 1 galaxies from the hard (2-10 keV) HEAO1-A2 extragalactic sample (Piccinoti *et al.* 1981). Schmidt and Green (1986), on the basis of this luminosity function, claim that, even without evolution, AGN contribute $\sim 30\%$ to the 2 keV X-ray background. They further assert that with some mild evolution AGN saturate the X-ray background intensity and therefore that PLE models are not viable (Schmidt 1988). Since we derived earlier that AGN cannot produce the bulk of the X-ray background it is vital to investigate why this disagreement occurs. We derive the AGN contribution using the Schmidt and Green (1986) luminosity function and evolving

94
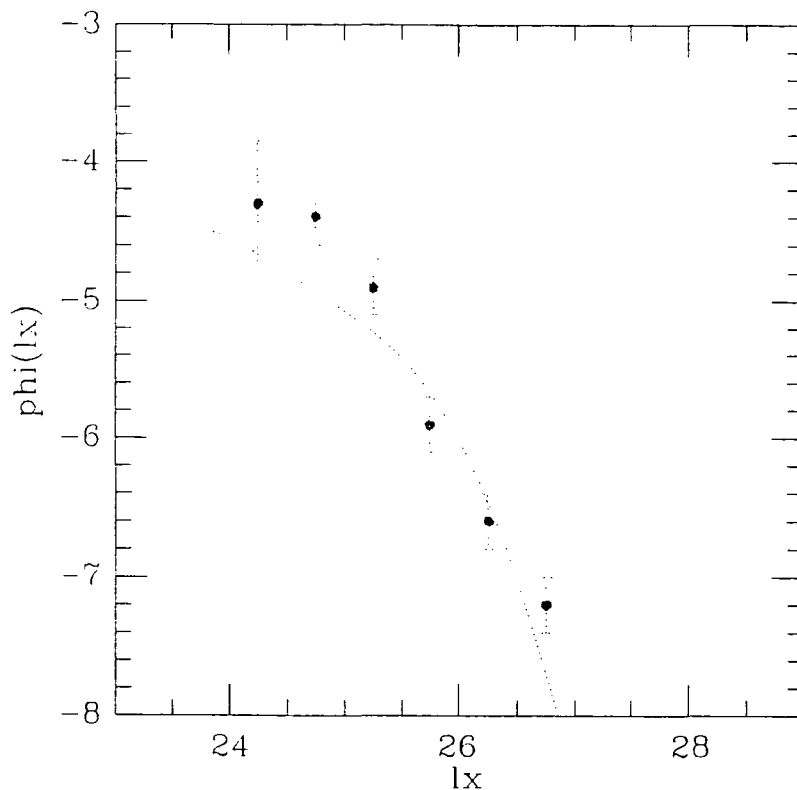
Figure 5.6: The predicted local ($z = 0$) AGN luminosity function (dotted line) and the observed Schmidt and Green (1986) low luminosity AGN X-ray luminosity function (filled circles).

it according to PLE models (Eqn. 5.11). Assuming that the X-ray luminosity function presents an abrupt cut-off at $L_x = 3 \times 10^{24}$ erg sec^{-1} Hz^{-1} (2 keV), the lower bound of the direct determination by Piccinoti et al. (1981), AGN are found to contribute $\sim 60\%$ for $a_x = 0.7$; this is roughly in agreement with our results. However, extrapolating this luminosity function an order of magnitude fainter in luminosity we find that AGN overpredict the X-ray intensity. It is evident that the cause of the saturation is the steep faint-end slope of the Schmidt and Green (1986) luminosity function; this is $\beta_x \approx -2$, compared with $\beta_x = -1.55$ for our predicted X-ray luminosity function. This discrepancy can be visualized in figure 5.6. It appears that the low luminosity AGN X-ray luminosity function samples excess objects at low luminosities. The discrepancy between the two luminosity functions

can be attributed to the following reasons. X-ray and optically selected surveys do not sample the same class of objects at faint luminosities. Stephens (1987), examining spectroscopically a small sample of X-ray selected QSOs, concludes that all of them show UVX and thus they would be detectable in colour surveys. Griffiths *et al.* (1988) find that four X-ray selected QSOs in their sample do not present UVX implying an incompleteness of 20% for the UVX surveys. However, these X-ray QSOs have redshifts in the range 0.5-0.9 (Griffiths priv. comm.), which is most susceptible to incompleteness. Incompleteness of 20% in this redshift range is in good agreement with our previous estimates. Recent ROSAT observations of the Durham QSO survey detect only two non UVX QSOs out of 19 and therefore imply a low level of incompleteness. At low luminosities some level of incompleteness is quite plausible. Dust or contamination by starlight could easily make some low luminosity AGN avoid detection in UVX surveys. Spectroscopic surveys can also miss some low luminosity AGN because of the difficulty in recognising AGN properties when the nuclear emission is weak. Again, the rough agreement of the IRAS Seyfert and the QSO luminosity function provides independent evidence that the incompleteness of optical surveys at low luminosities cannot be very high. Alternatively, the slope of the X-ray luminosity function may not be estimated accurately. Note that the faint end slope of the Schmidt and Green (1986) luminosity function is derived from less than eight objects. However, very recently, Marshall (1991) derived the hard X-ray luminosity function from an extended HEAO1 sample ($\sim$ 500 AGN). Preliminary results indicate that the luminosity function could be as steep as Schmidt and Green (1986) find at faint luminosities. In addition, Ginga fluctuations (Warwick and Stewart 1989) again might suggest the presence of an absorbed population at faint luminosities.

5.5   The Anisotropy

We have shown that AGN are likely to contribute half of the X-ray background intensity at 2 keV. Although there is some appreciable uncertainty in this result, its validity can be independently checked via the observed anisotropy of the X-ray background.

The most simple, first order, constraint on the amount of X-ray emission from discrete sources comes from the variance of the number of photons falling onto a pixel. The idea is that if the individual sources are distributed randomly in space, then an experiment will detect fluctuations in excess of those expected on the basis of the photon counting statistics, due to the fact that the actual number of discrete sources varies in different solid angle elements. As a result the distribution of photon counts will be broader than the Poissonian, with the width of the distribution depending on the form of the number counts $N(f)df$. Let's assume that the mean number of unresolved sources with flux between f and $f + df$ on a pixel subtending solid angle Ω is $\mu = N(f)df\Omega$; $N(f)df$ denotes the differential number counts, $N(f)df = kf^{-\gamma}$. For a random distribution of sources over the sky the expected flux variance from sources with flux f, $f + df$ is

$$\sigma^2 = \sum (n_i - \mu)^2 f^2 \frac{e^{-\mu}\mu^{n_i}}{n!} = f^2\mu = N(f)f^2 df\Omega \qquad (5.20)$$

Denoting by C the flux to counts conversion factor, and by T the total exposure time, we obtain for the photon variance

$$\sigma^2 = \frac{\Omega T^2}{C^2} \int N(f)f^2 df \qquad (5.21)$$

Although this integral can be readily solved analytically for a power law number count model, it is more convenient to express the variance in terms of the X-ray luminosity function $\Phi(L)$: $\sigma^2 = \int \int f^2 \Phi(L) dL dV$ or

$$\sigma^2 = (4\pi)^{-2} \frac{H_o}{c} \int_0^{z_{max}} \int_{L_{min}}^{L_{max}} \frac{L^2 K^2(z)\Phi(L)}{d_L^2(z)\sqrt{1 + 2q_o z}(1 + z)^3} dL \, dz \qquad (5.22)$$

where d_L and $K(z)$ denote the luminosity distance and K corection respectively. The lower limit of integration over luminosity, L_{min}, is the minimum AGN luminosity i.e. the low luminosity cut-off of the luminosity function. $L_{max}(f_{lim}, z)$ is the luminosity that, at redshift z, yields a flux equal to the detection limit f_{lim}.

Comparing the predicted variance (Eqn. 5.22) with the data, we obtain information on whether the X-ray luminosity function, and thus the predicted X-ray intensity, is consistent with the X-ray background fluctuation measurements. Recently, Hamilton and Helfand (1987) and Barcons and Fabian (1990) analyzed the observed fluctuations at arcminute scales, in the $1 - 3$ keV band, using long exposure IPC fields from the Einstein High Sensitivity Survey. The observed variance for 1' and 4' pixels can be found in Hamilton and Helfand (1987) and Barcons and Fabian (1990) respectively. Considering the width of the Point Spread function ($\sim$ 1'.5 FWHM), we choose to use 4' pixels; this ensures that adjacent pixels will not be significantly dependent. For the Eridanus field I3558, the mean number of counts is $\approx$ 58. Extrapolating the $3 - 40$ keV observed intensity (Marshall *et al.* 1980), Barcons and Fabian (1990) estimate that $\sim$ 37 counts are due to non cosmic counts e.g. geomagnetic particles and detector induced events. The variance observed is $\sigma^2 \approx 88 \pm 26$ where the error of the variance is $2\sigma^2/\sqrt{n-2}$ (Barford 1989).

To estimate the expected variance we use the Boyle, Shanks and Peterson (1988) optical luminosity function and an a_{ox} relation with $R = 1$, $\sigma = 0.12$. For an exposure time of $t \sim 20000$ sec and a flux limit of $\sim$ 78 counts or 2×10^{-31} erg cm^{-2} sec^{-1} Hz^{-1} at 2 keV, we predict a variance of $\sigma^2 \approx 85$ (for a Gaussian a_{ox} distribution with $\sigma = 0.12$). Note that this variance is solely due to cosmic X-ray photons. The variance due to non-cosmic counts σ_p^2, should be taken into account. Assuming that non
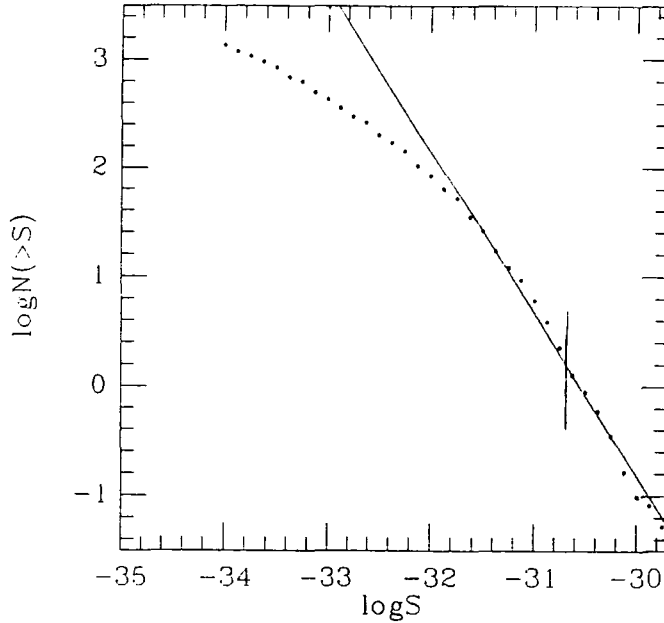
Figure 5.7: The predicted logN-logS relation at 2 keV for dispersion $\sigma = 0.12$. The solid line represents the $\gamma = 1.5$ slope. Vertical bar denotes the Einstein Deep survey Eridanus field flux limit.

cosmic counts are distributed uniformly the variance due to these events is $\sigma_p^2 = \mu_p = 37$ and thus the total predicted variance amounts to $\sigma^2 \approx 122$, i.e. 1.2σ above the observed value. The skew distribution ($\sigma = 0.14$) gives also $\sigma^2 \sim 120$ for the total variance. The rough agreement between the predicted and observed variance could be explained as follows. Hamilton and Helfand (1987) found that the number counts should flatten from the observed Euclidean slope, $\beta = -1.5$, to $\beta = -1.2$ or flatter. This finding is independently confirmed by Barcons and Fabian (1990). Indeed, our predicted X-ray number counts flatten drastically below the High Sensitivity Survey limit to $\beta \approx -0.5$ in agreement with their predictions (see Fig. 5.5). This flattening merely reflects the 'knee' feature of the luminosity function. Interestingly, the HEAO1 hard X-ray luminosity function yields a similar value ($\sigma^2 \approx 100$) for the variance due to AGN and thus an AGN

99

contribution of $\sim 100\%$ cannot be ruled out. Note, however, that if the luminosity function continues to have a slope of $\beta \approx -3$ down to $L_x \sim 10^{24}$ erg sec^{-1} Hz^{-1} (2 keV), then the variance would be overpredicted by a factor of two and therefore this model would be rejected at over the 99% confidence level.

More detailed predictions of the fluctuations have to take into account the clustering of AGN, as its effect is to decrease the effective number of source per beam and therefore to increase the anisotropy. To predict the variance, we assume that volume V is divided in infinitesimal volumes δV each containing one or no source. Then the variance is

$$\sigma^2 = \langle I \rangle^2 - \langle I^2 \rangle = \sum_i^N f^2 \Phi(L) \delta V_i + \sum_i^N \sum_k^N f^2 \Phi^2(L) \xi_{ik} \delta V_i \delta V_k \qquad (5.23)$$

The first term (I_1) gives the variance in the absence of clustering (Eqn. 5.22). The second term (I_2), that gives the excess variance if sources are clustered, is a double integral over the volume corresponding to the detector's pixel solid angle. Note that the term within the double sum is the autocorrelation function of the background intensity fluctuations (see Peebles 1980). A practical expression for I_2 can be obtained by assuming that objects are nearly all at the same distance, $u = |r_i - r_k| << r_i$ and that the angular separation θ_{ik} is small. At these limits

$$r_{ik}^2 = r_i^2 + r_k^2 - 2r_i r_k cos\theta_{ik} = r_i^2 + r_k^2 - 2r_i r_k (1 - \frac{\theta^2}{2}) = u^2 + (r\theta)^2 \qquad (5.24)$$

$\xi(r_{ik})$ at redshift z is expressed as $\xi(r_{ik}) = r_o^\gamma r_{ik}^{-\gamma} D(z)$ where r_o^γ is the present day correlation function amplitude and $D(z)$ allows for clustering evolution. $D(z)$ is expressed in proper coordinates. We discern between a stable and a comoving model for clustering evolution. In the stable model $D(z) \propto (1 + z)^{-3}$ while in the comoving model $D(z) \propto (1 + z)^{-1.8}$. Then

$$\begin{aligned} I_2 &= \frac{c}{H_o}(4\pi)^{-2} r_o^\gamma \int du(u^2 + (r\theta)^2)^{-\gamma/2} \\ &\quad \int j^2(1 + z)^{-2}(1 + 2q_o z)^{-0.5} D(z) dz d\Omega_i d\Omega_k \end{aligned} \qquad (5.25)$$

100

where j denotes the emissivity. The first integral was estimated by Totsuji and Kihara (1969). It can be expressed as a product of Gamma functions

$$H_\gamma = \int_{-\infty}^{+\infty} dx(1 + x^2)^{-\gamma/2} = \Gamma(1/2)\Gamma[(\gamma - 1)/2]/\Gamma(\gamma/2) \qquad (5.26)$$

For $\gamma = 1.8$, it yields $H_\gamma = 3.7$ and the final expression for I_2 is

$$I_2 = \quad \frac{c}{H_o}(4\pi)^{-2}r_o^\gamma H_\gamma$$
$$\int j^2(1 + z)^{-2}(1 + 2q_oz)^{-0.5}d_A^{1-\gamma}D(z)dz \int \theta^{-\gamma+1}d\Omega_i d\Omega_k \,(5.27)$$

where $d_A = d_L(1 + z)^{-2}$ is the angular diameter distance. The double integral over the solid angle that a pixel subtends is evaluated numerically. We find that the contribution of clustering to the expected variance is less than 2% for both the comoving and the stable evolution model. It is the first term, arising from the Poissonian fluctuations due to the finite number of sources per beam, that produces practically all the fluctuations at these small angular scales. This is not unreasonable: for the 4' pixels the expected number of QSOs, with $B < 26$, is around 4. In this regime the Poissonian fluctuations dominate the variance, while the I_2 term should make a significant contribution to the variance at angular scales larger than the one corresponding to the characteristic scale of clustering r_o, i.e. the separation at which the correlation function $\xi = 1$. The QSO characteristic clustering scale of $r_o = 7h^{-1}$ Mpc (Shanks *et al.* 1988) refers to the mean redshift of the Durham QSO survey, $\langle z \rangle = 1.5$; r_o corresponds to an angular distance on the sky θ given by

$$\theta = \frac{r_o}{d_a} = 0.33H_o r_o \frac{(z + 1)^2}{z + 1 - \sqrt{z + 1}} \qquad (5.28)$$

where θ is expressed in arcseconds, H_o in km sec^{-1}Mpc^{-1} and r_o in Mpc. Hence, $7h^{-1}$ Mpc correspond roughly to 10' on the sky. Therefore we expect that at pixels larger than 10' the clustering will have some impact on the expected variance.

Additional constraints on the AGN X-ray emission arise from the X-ray background autocorrelation function $C(\theta)$ (Peebles 1980)

$$C(\theta) = \langle \delta I(\mathbf{r})\delta I(\mathbf{r}') \rangle \qquad (5.29)$$

We next derive an expression for the autocorrelation function, in terms of the AGN two-point correlation function and luminosity function (see also De Zotti $et\ al.$ 1990). The probability that a galaxy with luminosity L in the range δL is found in the random volume element δV is $\delta P = \Phi(L)\delta L\delta V$. The probability that a galaxy with luminosity L_i in the range δL_i is found in the volume element δV_i and another galaxy of luminosity L_k is found in δV_k at distance r_{ik} is given by

$$\delta P = [\Phi(L_i)\Phi(L_k) + \Phi(L_i)\Phi(L_k)\xi(r_{ik})]\delta V_i\delta V_k \qquad (5.30)$$

where we assume that the luminosity of a galaxy is independent of its position relative to other galaxies. In exactly the same way the probability that the flux from δV_i is $f_i = \frac{\Phi(L_i)L_i\delta L_i}{4\pi d_L^2(z)}$ and the flux at δV_k is $f_k = \frac{\Phi(L_k)L_k\delta L_k}{4\pi d_L^2(z)}$ is given by

$$\delta P = f_i f_k \delta V_i \delta V_k (1 + \xi(r_{ik})) \qquad (5.31)$$

where the volume elements and luminosity functions are expressed in comoving coordinates. The probability of observing intensity I_i to $I_i + \delta I_i$ in solid angle element $\delta\Omega_i$ and intensity I_k to $I_k + \delta I_k$ in $\delta\Omega_k$ at angular distance θ_{ik} is found by integrating Eqn. 5.31 along the two lines of sight

$$\delta P = \int f_i f_k \delta V_i \delta V_k + \int f_i f_k \xi(r_{ik}) d_L^2(r_k)(1+z)^2 dr_i\ dr_k dL_i dL_k \delta\Omega_i\delta\Omega_k \qquad (5.32)$$

In exact analogy with the definition of the angular two-point correlation function (Peebles 1980), the second term defines the correlation function of the X-ray background intensity fluctuations, $C(\theta)$. The average value of $C(\theta)$ at given angle θ is obtained integrating over luminosities

$$C(\theta) = \frac{c}{H_o}(4\pi)^{-2} \int j^2(1+z)^{-2}(1+2q_o z)^{-0.5}\xi(r_{ik})dr_{ik}dz \qquad (5.33)$$

102

Table 5.4: The predicted $w(\theta)$ at $2°$

	optical	HEAO1
Stable	3×10^{-5}	1×10^{-3}
Comoving	1×10^{-5}	7×10^{-4}

where in the last expression j denotes the emissivity. Then it follows that

$$C(\theta) = \frac{c}{H_o}(4\pi)^{-2}r_o^\gamma H_\gamma \theta^{-\gamma+1}$$

$$\int j^2(1+z)^{-2}(1+2q_oz)^{-0.5}d_A^{1-\gamma}D(z)dz \qquad (5.34)$$

The normalized auto correlation function $w(\theta) = C(\theta)/\langle I \rangle^2$ was derived by Carrera *et al.* (1991) on degree scales ($> 2°$). These results come from the LAC detector on Ginga (4-12 keV) whose large collecting area and stability make these observations particularly suitable for the auto correlation function analysis. Carrera *et al.* (1991) derive an 95% confidence level upper limit of 10^{-4} for $w(\theta)$. We predict $w(\theta)$ again using the Durham optical ($R = 1, \sigma = 0.12$) and the HEAO1 hard X-ray luminosity function. We assume a QSO and a background X-ray spectral index of $a_x = 0.4$ and $a_x = 1$ respectively in order to extrapolate our 2 keV prediction down to the 4-12 keV region. The predicted values for $w(\theta)$ are given in table 5.4. Note that the optical luminosity function (and thus an AGN contribution of around 50%) is quite compatible with the data. On the other hand, the HEAO1 luminosity function $w(\theta)$ prediction is well above the 95% Ginga upper limit. Consequently, the X-ray background anisotropy seems to rule out the possibility that AGN produce the bulk of the X-ray background. This finding is in agreement with the results of Carrera *et al.* (1991) who used simpler models for the luminosity function and its evolution.

Chapter 6

ROSAT observations

6.1   Introduction

The only way to understand the origin of the X-ray background is to resolve as many sources as possible with a long enough exposure. This was attempted by Giacconi *et al.* (1979) and Griffiths *et al.* (1988) who found an X-ray source surface density of 25-30 $\deg^{-2}$, using Einstein High Sensitivity Survey fields. Giacconi *et al.* (1979) identified only 4 sources out of 43 as QSO due to the poor spatial resolution of Einstein's Imaging Proportional Counter (IPC) that translated to large amounts of telescope time for optical identification. In contrast Griffiths *et al.* (1988) using the high spatial resolution High Resolution Imager (HRI) in conjunction with multi object fibre spectroscopy, identified most of their 16 sources in Pavo with QSOs.

The Position Sensitive Proportional Counter (PSPC) (Pfefferman *et al.* 1986) on the new X-ray satelite ROSAT, is a soft X-ray detector (0.1-2 keV) ideal for the study of the X-ray background. With a 30000 sec expo-

sure the PSPC can reach at least a factor of three fainter than the deepest Einstein survey of Griffiths *et al.* (1988). This is the result of its very low particle background and its very good angular resolution ($\sim$ 5 times better than the Einstein's IPC).

6.2   The X-ray observations

A deep exposure (30000sec) was made with the PSPC in the pointed mode prior to the ROSAT all sky survey. The field selected is QSF3 from the Durham QSO survey (Boyle *et al.* 1990). The high galactic latitude of this field ($|b| \approx 50°$), minimizes galactic absorption problems ($N_H = 1.7 \times 10^{20}$ cm^{-2}) as well as stellar contamination problems in the optical identification of sources. An automated source detection algorithm detects 93 sources in the full 2° diameter field of view (FOV) at the $\sim 4\sigma$ level of confidence. The ROSAT image, integrated over the full energy range is shown in figure 6.1. The dark lines are due to obscuration from the detector's window support structure. At large off-axis angles the Point Spread function increases rapidly, the vignetting becomes severe and thus the sensitivity is significantly reduced. We therefore confine here the discussion to the central 20′ radius detector area. In this area, 39 sources were detected yielding a surface density of 111 ± 18deg^{-2}, to be compared with 36 ± 9 deg^{-2} for the Einstein High Sensitivity Survey (Griffiths *et al.* 1988).

Fluxes are obtained as follows. First, the number of photons falling on a 30″ radius aperture is measured for each source. The use of such small aperture ensures that a high value of signal to noise is obtained and also minimizes photon contamination from adjacent sources, which is a severe problem in such crowded field. As this aperture contains only a fraction of the total photon counts some correction has to be applied. This correction is
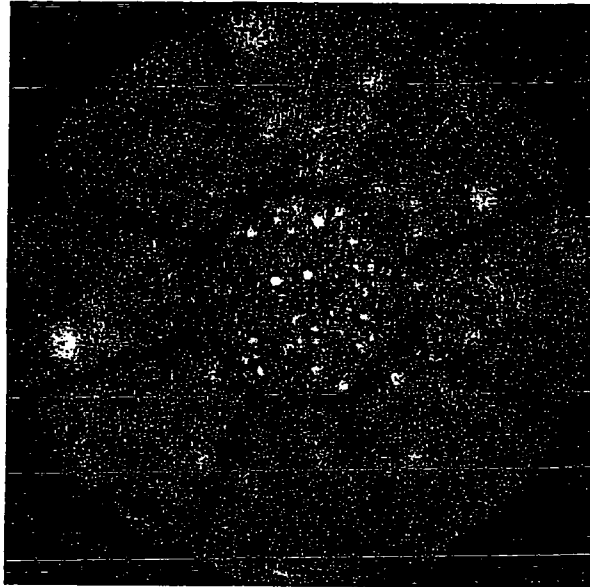
Figure 6.1: The full PSPC FOV (2° diameter), X-ray image (0.1-2 keV).

Table 6.1: Correction factor as a function of off axis angle

Off axis angle	5	9	13	15	19
Correction	1.5	1.8	2.0	2.2	3.0

estimated by measuring the Point Spread Function for a few bright sources at different off-axis angles; it is given in table 6.1. Measuring the background at different off-axis angles it is found that the vignetting correction within $20'$ radius is negligible ($< 10\%$). The photon counts are converted in flux by convolving the detector's energy response with the source spectrum. Since most of our sources are faint (< 100 counts) it is difficult to derive individual spectra. However, we can add the photon counts from all sources to derive a composite spectrum. We use only the 0.5-2 keV data, to avoid contamination from soft excesses at energies around 0.2 keV. Fitting a power law to the composite spectrum yields a best fit with energy spectral index

$a_x \sim 1$ (reduced $\chi^2 = 1.9$). This spectral form yields a counts to flux conversion factor of 9×10^{-12} $(erg~cm^{-2})^{-1}$.

6.3   Spectroscopic Follow Up Observations

We obtained spectroscopic follow up observations of the 39 sources in the central 20' FOV at the Anglo - Australian Telescope in November 1990. We used fibre optics (AUTOFIB) which enabled us to obtain spectra for all sources with $B < 22$ with a $\sim 20,000$ sec exposure. The spectral resolution was 10Å. As optical data already existed in this field it was easy to determine the absolute positions of X-ray sources with an accuracy better than 10''. No confusion problems arise as in most cases there is only one optical counterpart on the Schmidt plate within the X-ray error box.

Out of 18 optically selected QSOs in this field, 12 were detected in the X-ray, yielding a detection rate of $\sim 70\%$. Einstein observations showed that bright, nearby QSOs are X-ray emitters (Zamorani *et al.* 1981, Tananbaum *et al.* 1986). Now ROSAT extends this result to show that a 'typical' QSO (i.e. $B \sim 20, z \sim 1.5$) is also an X-ray emitter. In addition to the 12 optically selected QSOs there are 12 newly discovered QSOs bringing the total X-ray QSO number to 24 or a surface density of 69 ± 14 deg^{-2}. The redshift distribution of the 24 identified QSOs is shown in figure 6.2. It is clear that we detect high redshift QSOs (median z=1.5) instead of low luminosity, nearby Active Galactic Nuclei (AGN). The normalized redshift distribution of the Durham optical QSO survey is also shown on the same figure. It is evident that the two distributions are very similar suggesting that optical and X-ray surveys select the same class of objects. In addition 5 stars (mostly F stars and probably an O,G binary) and 2 galaxies were detected. The galaxy identifications include an elliptical galaxy at z=0.18

107
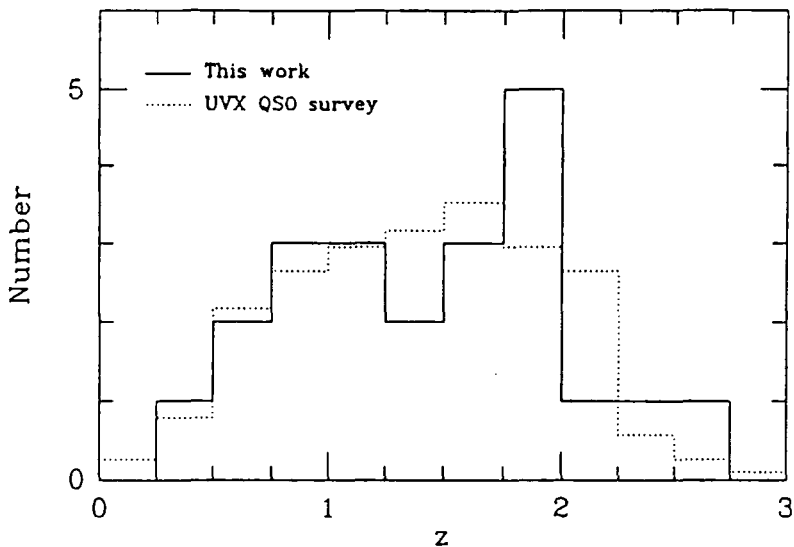
Figure 6.2: The redshift distribution of the 24 X-ray selected QSOs.

and an extended object on AAT plate with stellar nucleus, unusually blue $(U - B = -1.5)$ and with a featureless spectrum. None of these two objects present emission lines probably ruling out the possibility that these are starburst galaxies. Finally 8 faint X-ray sources remain unidentified. Out of these, 5 have no optical counterpart on the Schmidt plate. Interestingly, the unidentified objects have hardness ratios (ratio of the number of hard over soft photons) similar to QSOs. The full list of X-ray sources together with their X-ray fluxes, optical magnitudes and spectroscopic identification is given in table 6.2. The X-ray selected QSO spectra (Boyle priv. comm.) are given in figure 6.3.

Table 6.2: List of X-ray sources

IAU Name	Survey Name	$S(0.1\text{-}2.4\text{keV})$ $(\text{erg}\,\text{cm}^{-2}\text{s}^{-1})$	B (mag)	Spec. ID	z	N_{obj}	Comments
RX J0342.2−4350	XSF3:17	0.31×10^{-13}	18.4	Star	−	1	Composite spectrum
RX J0341.5−4351	XSF3:19	0.53×10^{-13}	−	?	−	0	
RX J0342.6−4353	XSF3:20	0.47×10^{-13}	19.7	QSO	0.564	1	
RX J0341.8−4353	XSF3:21	0.60×10^{-12}	10.0	Star	−	1	Spectral type F
RX J0342.3−4355	XSF3:23	0.36×10^{-13}	22.1	QSO	2.551	1	
RX J0343.3−4355*	XSF3:24	0.42×10^{-13}	20.3	?	−	1	Non-stellar image
RX J0343.0−4355	XSF3:25	0.12×10^{-12}	20.8	QSO	0.867	1	QSF3:01
RX J0341.0−4357	XSF3:28	0.20×10^{-13}	22.0	?	−	1	
RX J0341.2−4357	XSF3:29	0.41×10^{-13}	22.3	QSO?	0.66:	3	
RX J0340.9−4402	XSF3:32	0.49×10^{-13}	20.8	QSO	1.521	1	QSF3:29
RX J0341.2−4402	XSF3:33	0.18×10^{-13}	−	?	−	0	
RX J0340.6−4403	XSF3:35	0.20×10^{-13}	−	?	−	0	
RX J0342.0−4403	XSF3:36	0.29×10^{-12}	19.2	QSO	0.635	1	QSF3:13
RX J0343.8−4403	XSF3:37	0.91×10^{-14}	21.1	?	−	1	Star+Galaxy
RX J0342.6−4404	XSF3:38	0.30×10^{-12}	20.4	QSO	0.377	1	QSF3:39
RX J0341.2−4405	XSF3:42	0.24×10^{-13}	21.9	QSO	2.277	3	
RX J0343.4−4406	XSF3:44	0.24×10^{-13}	20.4	QSO	1.950	1	QSF3:40
RX J0341.0−4407	XSF3:45	0.57×10^{-13}	21.1	QSO?	1.76:	1	QSF3:20
RX J0342.5−4407	XSF3:46	0.16×10^{-13}	−	?	−	0	
RX J0342.0−4409	XSF3:48	0.13×10^{-13}	21.3	QSO	1.828	1	
RX J0341.3−4410	XSF3:51	0.33×10^{-13}	21.6	Star?	−	1	
RX J0341.6−4411	XSF3:53	0.29×10^{-13}	20.4	QSO	1.897	3	QSF3:27
RX J0341.0−4412	XSF3:54	0.67×10^{-13}	21.6	QSO	1.808	1	
RX J0343.9−4411	XSF3:56	0.13×10^{-13}	22.0	QSO?	2.21:	2	UVX
RX J0342.3−4412	XSF3:57	0.42×10^{-13}	21.8	QSO	1.091	1	
RX J0341.9−4414	XSF3:58	0.40×10^{-13}	20.1	QSO	1.478	1	QSF3:32
RX J0341.5−4414	XSF3:59	0.14×10^{-13}	22.2	QSO	1.09:	1	
RX J0341.1−4415	XSF3:61	0.24×10^{-13}	21.9	QSO	1.73:	1	
RX J0340.9−4415	XSF3:63	0.33×10^{-13}	19.4	Galaxy	0.180	1	Elliptical galaxy
RX J0343.0−4416	XSF3:64	0.56×10^{-13}	10.0	Star	−	1	Spectral type F
RX J0342.2−4416	XSF3:65	0.40×10^{-13}	19.2	QSO	2.077	2	Double QSO
	XSF3:65a			QSO	1.586		
RX J0341.9−4416	XSF3:66	0.33×10^{-13}	19.5	QSO	1.797	2	QSF3:31
RX J0341.1−4417	XSF3:67	0.38×10^{-13}	22.3	?	−	2	
RX J0342.4−4417	XSF3:68	0.25×10^{-13}	−	?	−	0	
RX J0343.2−4420	XSF3:70	0.45×10^{-13}	21.2	QSO	1.378	1	QSF3:45
RX J0341.9−4422	XSF3:71	0.70×10^{-13}	21.5	QSO	1.08:	1	
RX J0342.9−4422	XSF3:72	0.97×10^{-13}	19.8	QSO	0.897	1	QSF3:47
RX J0341.4−4425	XSF3:77	0.63×10^{-13}	19.5	QSO	0.794	1	QSF3:36
RX J0342.0−4425	XSF3:78	0.88×10^{-14}	20.6	?	−	2	Non-stellar image
	XSF3:78a		18.4	Star	−		Spectral Type F

: − Uncertain redshift
* − Uncertain optical position

109
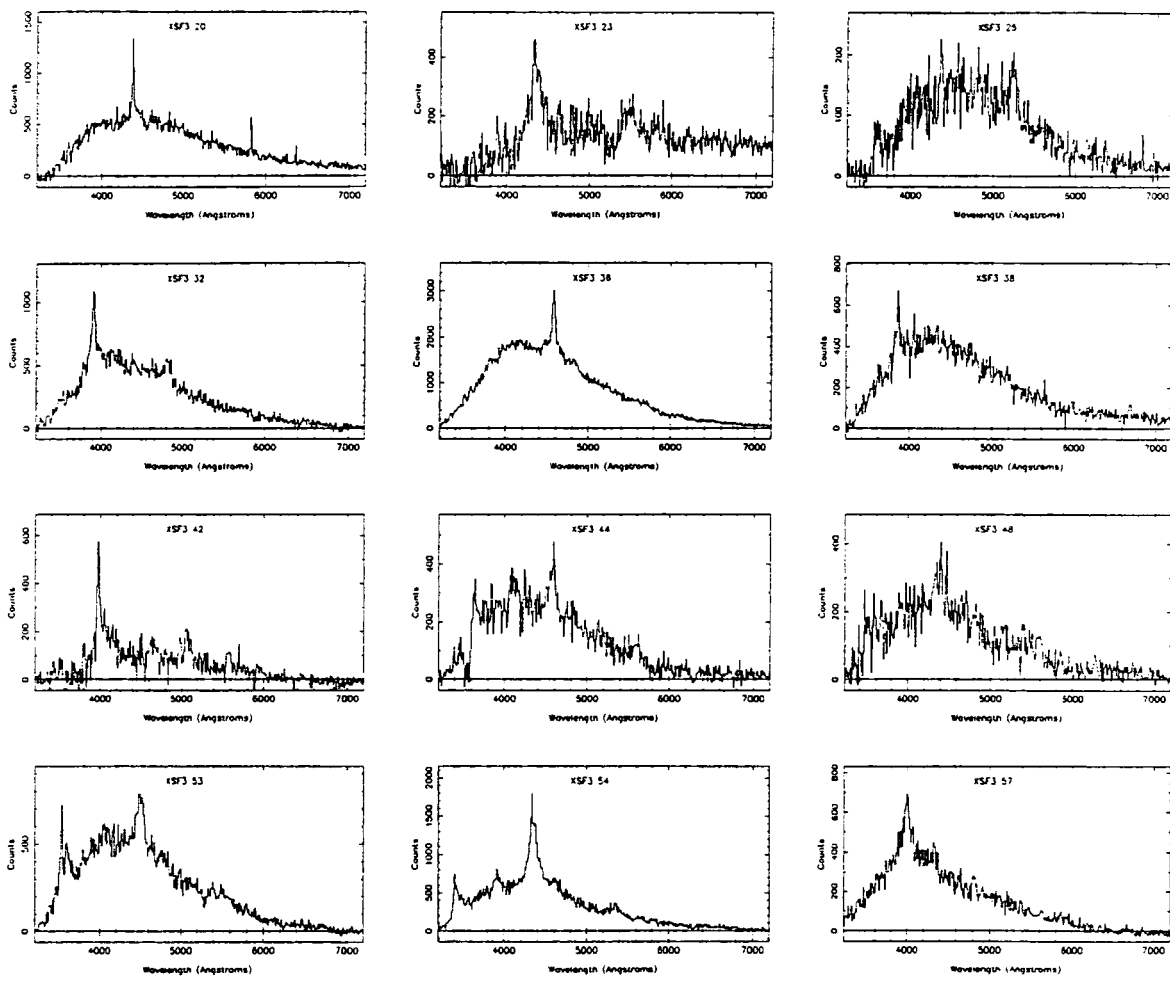
Figure 6.3: The 12 newly discovered QSO spectra.
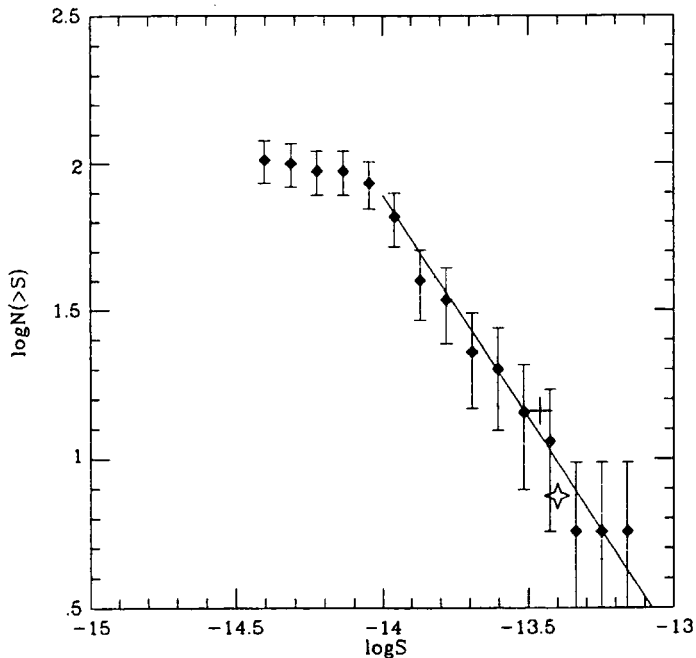
Figure 6.4: The integral number counts (0.5-2 keV) of all objects except the five identified with stars. The solid line represents the Euclidean slope. The cross denotes the deep survey of Primini *et al.* (1991) and the star denotes the Extended Medium Sensitivity Survey of Gioia *et al.* (1990).

6.4   The Number Counts

Here we present the integral number counts for all sources except the five identified with stars. We use the 0.5-2 keV flux, first because this overlaps with the Einstein's passband and second because in this energy region the source spectra can be approximated with a single power law and therefore flux conversions are straightforward. The integral counts are presented in figure 6.4. At bright fluxes the number counts are consistent with the Euclidean $\gamma = 1.5$ slope. Our data are consistent with the Einstein Extended Medium Sensitivity Survey (EMSS) of Gioia *et al.* (1990) and the Einstein Deep survey of Primini *et al.* (1991). There is an apparent break at faint

fluxes to a flatter power law. However, this break occurs close to our flux limit and therefore incompleteness and flux errors may be a problem. Note that this feature was also seen in a deep ROSAT exposure of the North Ecliptic Pole (Hasinger, Schmidt and Trumper 1991).

6.5 The ROSAT a_{ox}

The derivation of the a_{ox} spectral index is mainly based on observations of bright QSOs with Einstein. Due to their low space density these QSOs do not make significant contribution to the X-ray background. The bulk of the QSO contribution should emanate from the numerous, faint ($B > 20^m$, $z > 1$) QSOs; typical examples of these are the QSOs detected in our ROSAT survey. It is therefore important to derive a_{ox} for the ROSAT QSOs in order to check if the X-ray properties of 'typical' QSO are similar to these of bright QSOs. The 2 keV monochromatic flux is estimated using the average spectrum of sources in our field, i.e. an X-ray power law spectrum with spectral index $a_x = 1$. Then, the conversion factor between 0.5-2 keV photon counts and 2 kev monochromatic flux (erg cm^{-2} sec^{-1} Hz^{-1}) is 7×10^{-30}. The ROSAT QSOs have a mean a_{ox}, $\langle a_{ox} \rangle = 1.49$ with a standard deviation of $\sigma = 0.12$; a_{ox} strongly depends on optical luminosity L_o. A least squares regression analysis yields $A_l = 0.17 \pm 0.04$ and $A_o = -3.65 \pm 1.386$ ($a_{ox} = A_l \log L_o + A_o$) which implies a non linear relation between optical and X-ray luminosity ($L_x \propto L_o^{0.6}$). This is in very good agreement with the results of Griffiths et al. (1988) who used 14 X-ray selected QSOs from the Pavo field. a_{ox} for ROSAT QSOs is presented in figure 6.5. For comparison the Avni and Tananbaum (1986) a_{ox} best fit is also presented. One has to be cautious in comparing the Avni and Tananbaum (1986) with the present ROSAT result as the former refers to an optically selected while the latter
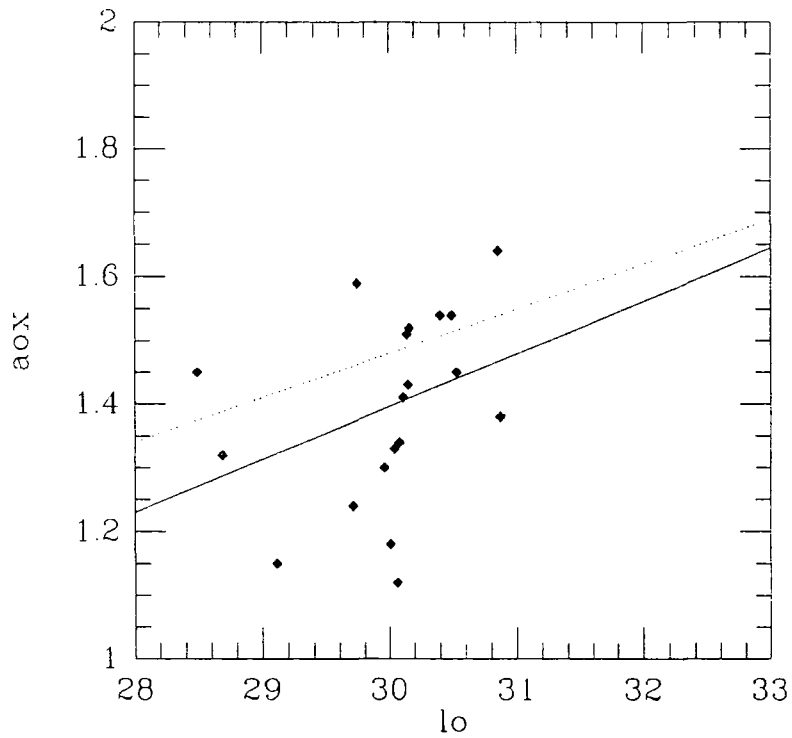
Figure 6.5: The a_{ox} spectral index for the 24 X-ray selected QSOs (diamonds). The solid line denotes the best linear fit to the data while the dotted line represents the a_{ox} found from Einstein data (Avni and Tananbaum 1986).

refers to an X-ray selected sample.

6.6 Detected QSO contribution to the X-ray background

The ROSAT 0.1-2 keV background lies above the extrapolated, extragalactic spectrum measured by HEAO-1 (Marshall *et al.* 1980). At 1 keV this excess is above 50%. We do not know the exact amount of galactic contribution in the ROSAT passband but we confine our discussion to the 0.5 - 2 keV range to minimize any such contribution. The particle background was subtracted assuming that the particle spectrum is flat and that all counts above 2 keV, where the reflectivity of the mirror falls drastically, are due to particles. The most straightforward way to estimate the QSO contribution to the X-ray background is simply to add up the 24 QSOs photon counts and divide with the total background counts in the central 20' radius detector area. This provides a model independent, estimate of 30% for the QSO contribution to the ROSAT background at 1 keV. Note that this is only a lower limit since it takes into account only the identified QSOs.

The key question is whether QSOs can produce all the X-ray background. The first step to answer this question is to compare the QSO and the background spectra. The most straightforward comparison is to plot the ratio of the QSO over the background counts in the central 20' as a function of energy (figure 6.6). If the QSO and background spectra were the same, then we would expect to see a straight line in contrast to what is observed here. The drop of the ratio below 1 keV is probably due to the gradual increase of the galactic background component (e.g. geocoronal component). However, the drop of the ratio above 1 keV suggests that the QSO and
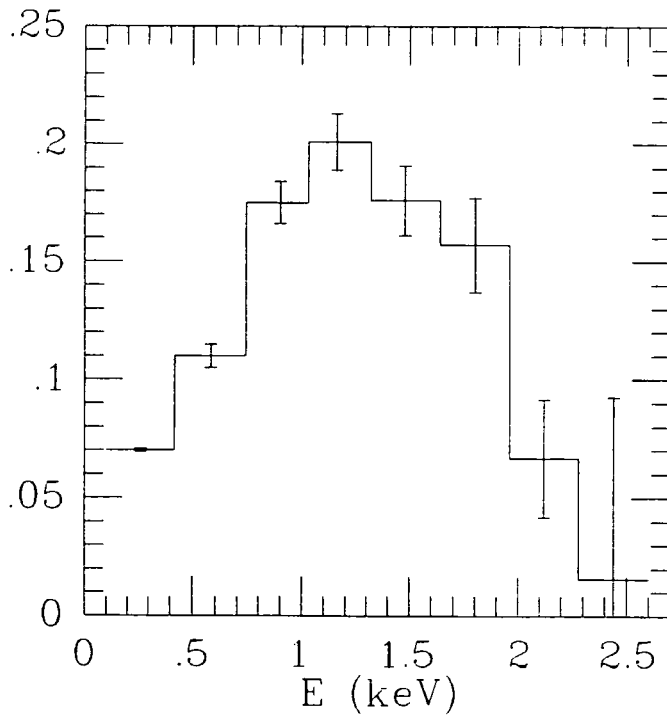
Figure 6.6: The ratio of the QSO over the background counts in the central 20′ of the PSPC FOV as a function of energy.

the background spectra are different. This represents only a $\sim 2\sigma$ result and has to be viewed cautiously as it comes only from one field. Note also, that Hasinger Schmidt and Trumper (1991) find a steeper spectrum for the background, which is more similar to the source spectrum.

Chapter 7

Conclusions

7.1   The Seyfert luminosity function

We verified the form of the Seyfert galaxy luminosity function: The luminosity function of Seyfert galaxies from the IRAS Point Source Catalogue is well represented by a two power law expression, in agreement with previous spectroscopic (Marshall 1987) and UVX surveys (Cheng *et al.* 1985). The optical QSO luminosity function, evolved back to $z \sim 0$ according to Pure Luminosity Evolution models, agrees well in shape and normalization with the IRAS Seyfert luminosity function. This suggests that Seyferts are the endpoints of QSO evolution, i.e. Seyferts and QSOs are the same objects viewed at different cosmic epoch. In particular, the faint part of the IRAS Seyfert luminosity function is flat ($a \approx -1.4$), similar to the optical QSO and soft X-ray luminosity function. This suggests that IR, ultraviolet excess and soft X-ray surveys select the same class of objects and therefore that optical and soft X-ray surveys do not suffer from severe incompleteness.

7.2   The Seyfert clustering

We demonstrated that Seyfert galaxies are clustered; their clustering is similar in strength to that of optical galaxies; the AGN clustering evolution is more consistent with a comoving model, where AGN are still expanding with the Hubble flow.

Using a sample of 192 IRAS selected Seyfert galaxies distributed over a large fraction of the sky ($\sim 8sr$), we found a clear detection, at the 5σ level, of Seyfert clustering on scales $< 20h^{-1}$ Mpc. At larger scales there is no clearcut evidence for clustering. We compared the strength of this Seyfert clustering with that of optically selected normal galaxies. This comparison suggests that Seyferts and normal galaxies have similar clustering properties. However, cross correlation of our Seyfert sample with the IRAS 'normal' galaxies shows that Seyferts cluster more strongly than the IRAS galaxies (at over the 99% confidence level).

We compared the IRAS Seyfert with the optical QSO correlation function in order to probe the AGN clustering evolution over a wide redshift range. We attempted to discriminate between the stable model, where AGN trace clumps of mass that have collapsed and ceased to expand with the Hubble flow, and the comoving model, where galaxies continue to expand with the Hubble flow even at regions where the clustering is strong. There are two inherent assumptions in such a comparison. First, Seyferts and QSOs are the same objects viewed at different cosmic epoch. Second, the IRAS selection of Seyfert galaxies does not introduce any bias, e.g. towards low density regions. The last assumption is not unreasonable as Seyfert nuclei are associated with spiral galaxies, which are probably selected by IRAS without any bias. Under the assumptions above we showed that a comoving model for clustering evolution is probably favoured by the data over

the $z = 0 - 1.5$ redshift range. This is suggestive of 'biased' theories of clustering where AGN cluster more strongly than the mass (Davies *et al.* 1985). However, this result comes mainly from small scales ($< 10h^{-1}$) where the number of pairs is small and thus the statistical uncertainty high. At larger scales ($10 < r < 20h^{-1}$ Mpc) the agreement of the stable model with the data is satisfactory and therefore the stable model cannot be definitely ruled out. At higher redshifts the picture is again controversial as Boyle *et al.* (1991) find no evidence for evolution while Iovino *et al.* (1991) find weak evidence (2σ) for stable clustering evolution.

Direct CCD imaging of the QSO environments may help to discriminate between the two clustering evolution models: as the optical galaxy correlation function agrees remarkably well with the QSO correlation function evolved back to $z \sim 0$ according to the comoving model (Shanks *et al.* 1988), QSOs and Seyferts should randomly select the galaxy population and should not reside in particularly rich environments. Yee and Green (1987) imaged QSO environments with CCD, and showed that this is not the case for radio loud QSOs at very small scales ($r < 1h^{-1}$ Mpc). Comparison of the amplitudes of the galaxy - radio quiet QSO and the galaxy - galaxy correlation functions (e.g. Ellington, Yee and Green 1991) at large scales $< 20h^{-1}$ Mpc can directly test the comoving model.

7.3   The optical QSO luminosity function

We verified the form and evolution of the optical QSO luminosity function of Boyle, Shanks and Peterson (1988). The turnover at faint luminosities cannot be attributed to incompleteness at faint magnitudes.

We recalibrated the photometry of the Durham UVX catalogue, using a

large number of faint CCD observations. This calibration was essential in order to check the completeness of the Durham QSO survey. We found that the mean incompleteness is around 10%, in rough agreement with the predictions of Boyle (1986). Such a low level of incompleteness cannot introduce an artificial break feature in the optical luminosity function. We therefore confirm the results on the form and evolution of the optical luminosity function derived by Boyle, Shanks and Peterson (1988).

7.4   The X-ray background

We made a new detailed estimation of the AGN contribution to the X-ray background using the optical luminosity function of Boyle, Shanks and Peterson (1988) in combination with the AGN X-ray to optical luminosity relation. An AGN contribution of $\sim$ 50% to the 2 keV X-ray background was derived. This is in good agreement with the predictions of Maccacaro *et al.* (1991) based on the EMSS luminosity function. The ROSAT data reveal a high number of AGN giving a direct lower limit of 30% for the AGN contribution consistent with our estimates above. The ROSAT results on the L_x/L_o ratio of high redshift, intrinsically faint QSOs agree remarkably well with the previous Einstein results of nearby, luminous QSOs confirming our predictions on the X-ray luminosity function and thus confirming that optically selected QSOs cannot easily account for over 50% of the soft X-ray background. This conclusion is further strengthened by the anisotropy of the residual background and the fact that the QSO and the background spectra appear to be discrepant in the 0.1-2 keV band. If AGN were to produce the bulk of the X-ray intensity, then AGN with a new 'face' have to be invoked e.g. highly absorbed, low luminosity Seyfert type nuclei, possibly present among the faintest sources in the hard surveys.

7.4.1 The soft X-ray background

The vast majority of extragalactic X-ray sources has been discovered by imaging instruments sensitive to soft X-rays. Therefore we focused our attention on predicting the AGN contribution to the soft X-ray background. We evaluated the AGN X-ray emission combining the optical luminosity function with the relation between the X-ray and the optical luminosity. Before evaluating the AGN X-ray emission, we had to make sure that the X-ray luminosity function, predicted from the optical luminosity function, agrees with the soft X-ray data. In accordance with Franceschini, Gioia and Maccacaro (1986), we found that to bring into agreement the predicted and observed X-ray luminosity and redshift distribution the dispersion, σ, of the $L_x : L_o$ relation should have a value of $\sigma = 0.12$, i.e. much lower than the observed $\sigma = 0.20$. Preliminary ROSAT results from an X-ray selected QSO sample suggest that the dispersion is low ($\sigma = 0.12$). This suggests that either the dispersion σ is a function of luminosity (in these ROSAT observations we observe intrinsically bright AGN) or alternatively that a small fraction of the AGN population is weak in soft X-rays. The latter is possible if some AGN have high intrinsic column densities that block some of the soft X-rays. This would then result in excess dispersion for an optically selected sample.

We derived that the AGN contribution to the X-ray background is $50 \pm 25\%$. The error on our estimate ($\pm 25\%$) arises mainly from the uncertainty in the faint slope of the optical luminosity function and secondly from the uncertainty in the $L_x : L_o$ relation. The error, although appreciable, is much lower than those quoted in previous estimates of the X-ray emission from optical data (e.g. Marshall *et al.* 1983) mainly due to the better constrained optical luminosity function. Maccacaro *et al.* (1991) using the EMSS soft X-ray luminosity function derive a 40% AGN contribution

in good agreement with our predictions. Note that the use of the optical luminosity function is advantageous as the slope of the faint end of the luminosity function and the evolution are very well determined. Half of the objects in the EMSS sample have $z < 0.4$ and thus the evolution and the shape of the luminosity function at high redshifts ($z > 1$) where the bulk of the X-ray emission comes from are difficult to derive.

We also derived the AGN X-ray emission using the hard (2-10 keV) X-ray local luminosity function of Schmidt and Green (1986), evolving it according to Pure Luminosity evolution models. The contribution derived is very sensitive to the luminosity function, low luminosity cut-off. It varies from over 60% for $L_x = 3 \times 10^{24}$ erg sec^{-1} Hz^{-1} at 2 keV (the lowest luminosity observed in the sample) to over 100% for $L_x = 10^{23}$ erg sec^{-1} Hz^{-1}. The discrepancy between the estimation using the optical (or the soft X-ray) and the hard X-ray luminosity functions is caused by the low luminosity objects; Although both luminosity functions are described by a broken power law, the faint end of the hard X-ray luminosity function is much steeper than the optical faint end. It is not yet clear whether this difference is due to statistical uncertainty or if it reflects some true excess density of objects in the hard X-rays. As the Einstein EMSS luminosity function comes from soft X-ray data, it is possible that high intrinsic column densities associated with low luminosity AGN (see Turner and Pounds 1989) might have introduced some incompleteness. Again, the ultraviolet excess optical luminosity function could miss a few objects e.g. due to intrinsic reddening. However, it is not clear whether high N_H is associated with high Balmer decrement and thus reddening (Turner and Pounds 1989). Furthermore, the IRAS should have easily detected such heavily reddened objects, while, as previously shown, the infrared luminosity function agrees remarkably well with the optical luminosity function. Alternatively, the poor statistics of the Schmidt and Green (1986) luminosity function at low luminosities

could account for the discrepancy between the hard X-ray and optical luminosity function. Note, however, that recently Marshall (1991) derived the hard X-ray luminosity function from an extended HEAO1 sample of $\sim$ 500 AGN. He claims (priv. comm.) that the luminosity function could still present a steep slope at faint luminosities. In addition, some evidence for an absorbed population of faint sources comes from Ginga background observations (2-10 keV). Warwick and Stewart (1989) constrain the X-ray logN-logS relation using the observed fluctuations and conclude that the normalization of this relation is three times higher than that of the Einstein EMSS survey, implying that EMSS could be substantially affected by absorption. If indeed absorption can account for the discrepancy between the hard and the soft X-ray luminosity functions, then at low redshifts, where absorption is important, the hard X-ray luminosity function will overpredict the AGN contribution to the soft X-ray background. However, at high redshifts ($z > 1.5$) where absorption of the 2 keV observed flux becomes unimportant the hard X-ray luminosity function might provide a more realistic estimate of the AGN contribution to the soft X-ray background.

Recent ROSAT observations helped to explore further the X-ray properties of AGN and their contribution to the soft X-ray background (0.1-2keV). The outstanding result from a deep ROSAT exposure is that the majority of sources detected are AGN. More specifically, out of 39 sources, 24 are spectroscopically identified AGN while 7 sources still remain unidentified. The identified QSOs contribute around 30% to the 1 keV X-ray background in agreement with our predictions based on the optical luminosity function. Out of 18 UVX selected QSOs in this field, 12 were detected in the X-ray. This is very important as it shows that moderate redshift, $z \sim 1.5$, faint, $B < 21^m$, AGN are typical X-ray emitters and therefore significant contributors to the X-ray background due to their high space density. The L_x/L_o ratio of these intrinsically faint AGN is very similar to that of the

brighter nearby QSOs observed by Einstein. Consequently the ROSAT results strongly confirm our previous estimates of the AGN contribution to the soft X-ray background.

Comparing the QSO with the background spectrum provides useful constraints on the AGN contribution to the background. The QSO spectrum appeared to be steeper than the background spectrum in the 0.5-2 keV region (as it appears to be steeper in the 2-10 keV energy range). However, this result should be viewed with caution as it comes from only one field and it is based on a limited spectral range. Note that our result is in disagreement with Hasinger, Schmidt and Trumper (1991) who find similar spectral slopes for QSOs and the background.

The estimates of the AGN X-ray emission above have to be consistent with the observed X-ray background fluctuations. We therefore predicted the variance of the X-ray photon distribution and compared it with the small angular scale data from the Einstein High Sensitivity survey. We found that the predicted variance is consistent (within $\sim 1\sigma$) with the observed variance. Therefore a QSO contribution of $\sim 50\%$ cannot be ruled out on the basis of the small scale anisotropy of the soft X-ray background. This is also consistent with the degree angular scale, high energy (2-10 keV) results of Shafer and Fabian (1983). A $\sim 50\%$ AGN contribution is compatible with the observed X-ray background anisotropy (4-12 keV) when clustering is taken into account. It was demonstrated that the Boyle *et al.* (1988) luminosity function is consistent with the autocorrelation function results at 2° for both the comoving and the stable model of clustering evolution.

7.4.2 The hard X-ray background (>3 keV)

This energy band is very important as it is here where the energy density of the background lies (around 40 keV). The AGN contribution is difficult to assess as only few tens of objects have been detected mainly with HEAO1 and Ginga. Thus the X-ray luminosity function is not well constrained while the spectral properties are known only for few bright nearby AGN that contribute less than 1% to the X-ray background. Extrapolation of our 50% estimate for the AGN contribution at 2 keV, assuming a spectral index of $a_x = 0.7$ yields a contribution of 35% in the 2-10 keV band and only 20% in the 30-40 keV band. Nevertheless AGN could contribute a substantial fraction of the hard background if their spectra flattened at hard energies. Additional constraints on the AGN X-ray emission emanate from the anisotropy of the hard X-ray background. Results from the autocorrelation function (De Zotti *et al.* 1990, Carrera *et al.* 1991) show that only $\sim 50\%$ of the hard background can be accounted for AGN provided that the clustering length of these objects is similar to that of optically selected QSOs.

The picture emerging from the current observations is that optically selected AGN cannot account for the X-ray intensity, the spectrum and the anisotropy of the 0.1-40 keV background. However, AGN with a new 'face', for example highly absorbed low luminosity AGN, could possibly make the intensity provided that their luminosity function is steep at faint luminosities. Although the AGN contribution to the X-ray background is still subject to some uncertainty, at least it was shown that Pure Luminosity Evolution models are consistent with both the X-ray background intensity and anisotropy constraints, in disagreement with Schmidt and Green (1986) who asserted that Pure Luminosity Evolution overpredicted the X-ray background intensity.

7.5   Epilogue

7.5.1   What makes the other 50%?

If the AGN and background spectra are indeed discrepant, then some other component with a flat spectrum ($a_x < 0.4$) makes a significant contribution to the background at fluxes fainter than our ROSAT survey flux limit, $S_o = 5 \times 10^{-15}$ erg cm^{-2} sec^{-1} (0.5-2keV). Possible candidates are starburst galaxies, as Einstein observations have shown that these are strong X-ray emitters (Fabbiano 1989). Griffiths and Padovani (1989) have showed that massive X-ray binaries can produce the flat spectra required. If, however, the bulk of X-ray emission comes from supernova remnants, then the spectra are expected to be steep. Combination of the galaxy logN-B magnitude relation with the f_x/f_o flux ratio observed for normal galaxies, yields a 13% contribution to the 2 keV background (Giacconi and Zamorani 1987). Considering that the starburst f_x/f_o ratio could be an order of magnitude higher than that of normal galaxies, it is evident that starbursts can easily produce 50% of the X-ray background (Griffiths and Padovani 1990) provided that were abundant in the past. Indeed, deep optical surveys (Broadhurst, Ellis and Shanks 1987) reveal a large amount of blue, starburst galaxies. Possibly these galaxies are associated with the sub-mJy radio sources that dominate the radio number counts at deep fluxes. A significant starburst galaxy contribution to the X-ray background would not be incompatible with the smoothness of the X-ray background at arcminute scales: with normal galaxies reaching a surface density of 10^6 deg^{-2} at $B \sim 26$, starburst galaxies could easily have the high surface density required to produce the very low level of fluctuations observed. Fluctuation constraints are further relaxed as starburst galaxies probably do not cluster as strongly as AGN, as suggested by this work (see also Iovino and Shaver 1988).

126

Alternatively, if the AGN spectrum flattens at high energy it is possible for AGN to reproduce exactly the observed background spectrum at 1-10 keV (Schwartz, Qian and Tucker 1989). Such a flattening of the X-ray spectrum was observed in Ginga results (Nandra 1991). This is due to a hump at around 10 keV caused by Compton down-scattering of high energy photons and photoelectric absorption of the low energy ones. Fabian *et al.* (1990) demonstrated that this spectrum fits very well the observed X-ray background spectrum, even at high energies, where it reproduces the 30 keV background turnover. As shown previously, AGN can produce the total intensity of the X-ray background only if the HEAO1 hard X-ray luminosity function has a steep slope at low luminosities i.e. there is a numerous population of heavily absorbed sources at low luminosities. This may be suggested directly by the extended HEAO1 AGN sample (Marshall 1991) and indirectly by the Ginga hard X-ray (2-10 keV) fluctuations. If AGN produce the bulk of the X-ray background, they should be consistent with its isotropy. A 100% AGN contribution is just compatible with the arcminute angular scale fluctuations, provided that the luminosity function presents a knee feature to a flatter power law. However, the autocorrelation function at degree scale appears to rule out a 100% AGN contribution at the 3σ confidence level, even in the case of mild (comoving) clustering evolution. This was also demonstrated by Barcons and Fabian (1988), De Zotti *et al.* (1990) and Carrera *et al.* (1991), who used more simplistic models for the luminosity function and its evolution.

7.5.2 The Future

If the logN-logS relation of X-ray sources flattens, as the predictions from the optical luminosity function and the first ROSAT results seem to indicate, then we will have to probe three orders of magnitude fainter in flux before

we resolve the X-ray background, i.e. not even AXAF will be able to resolve it. However, there are a few crucial tests that can help us to understand the nature of the X-ray background.

The first step is to compare, with good statistics, the spectra of QSOs and the background at soft energies. If QSO and background spectra are found to be different then a QSO origin of the X-ray background would be hard to envisage. The test above can be performed with ROSAT and the answers should not be long in emerging. Of course, before making such comparison, one has to make sure that the soft background observed is not heavily contaminated by galactic emission. This can be easily tested with 'shadowing' techniques using molecular clouds at high distance (> 500 pc). These clouds must have high N_H so that shadowing in the 0.5-2 keV band can be detected. The first observations (e.g. cloud MBM41) show some shadowing but cannot rule out the possibility of an appreciable local galactic emission.

The next step is to study the anisotropy of the soft X-ray background with ROSAT. The PSPC is ideal for such studies due to its very efficient background rejection and very good angular resolution. Preliminary studies of the fluctuations of the ROSAT background have been reported in Shanks *et al.* (1991). The fluctuations imply that a surface density of 4000 deg^{-2} is necessary to reproduce the smoothness of the background observed, in agreement with the previous Einstein results of Hamilton and Helfand (1987). It is difficult for AGN to account for this high surface density but not entirely unreasonable. Thus the constraints imposed by the fluctuation analysis are not very powerful. Correlation analyses probably will provide a more efficient tool for testing the AGN contribution to the residual background. The autocorrelation function derived from ROSAT (Georgantopoulos *et al.* 1992) shows that AGN with clustering length of $6h^{-1}$ Mpc cannot contribute

over 40% of the residual ROSAT background.

Although, thanks to ROSAT and Einstein, we have some idea of the nature of the soft background, the hard X-ray background is less well explored. The background spectrum in this energy region is well measured but less than one source per square degree is resolved (mostly Seyfert galaxies). As these AGN are bright, nearby objects it is unreasonable to extrapolate their X-ray properties to the distant faint QSOs that contribute the bulk of the AGN X-ray emissivity. Astro-D and JET-X will be the first instruments to resolve the hard X-ray background to flux limits comparable with that of the ROSAT PSPC. The major scientific quest is to understand the nature of the sources that appear in the Ginga fluctuations. Are they heavily absorbed AGN? Can their spectra mimic the flat ($a_x \sim 0.4$) background spectrum in this energy region? JET-X and Astro-D with both imaging and spectroscopy capabilities have the potential to provide definite answers to these questions.

References

Anderson, N., Kunth, D., Sargent, W.L., 1988. *Astron. J.*, **95**, 644.

Anderson, S.F., & Margon, B., 1987. *Astrophys. J.*, **314**, 111.

Arp, H., 1962. *Astron. J.*, **135**, 311.

Avni, Y., 1976. *Astrophys. J.*, **210**, 642.

Avni, Y., Soltan, A., Tananbaum, H., Zamorani, G., 1980. *Astrophys. J.*, **238**, 800.

Avni, Y. & Tananbaum, H., 1982. *Astrophys. J.*(Letters), **262**, L17.

Avni, Y. & Tananbaum, H., 1986. *Astrophys. J.*, **305**, 83.

Baldwin, J.A., Philips, M.M., Terlevich, R., 1981. *Pub. Astron. Soc. Pacific*, **93**, 5.

Barcons, X., 1987. *Astrophys. J.*, **313**, 547.

Barcons, X. & Fabian, A.C., 1988. *Mon. Not. R. astr. Soc*, **230**, 189.

Barcons, X. & Fabian, A.C., 1989. *Mon. Not. R. astr. Soc*, **237**, 119.

Barcons, X. & Fabian, A.C., 1990. *Mon. Not. R. astr. Soc*, **243**, 366.

Barford, N.C., 1985. *Experimental measurements: precision error and truth*, Wiley.

Bean, J., 1983. Ph.D. thesis, University of Durham.

Beichman, C., 1988. *IRAS Explanatory Supplement*, NASA.

Binggeli, B., Sandage, A., Tammann, G.A., 1988. *Ann. Rev. Astron. Astroph.*, **26**, 509.

Boesgard, A.M., Steigman, G., 1985. *Ann. Rev. Astron. Astroph.*, **23**, 319.

Bok, B.J., 1934. *Harvard Obs. Bull*, No 8951.

Boldt, E., 1987. *Phys. Rep.*, **146**, 215.

Bonoli, F., Braccesi, A., Federici, L., Zitelli, V., 1979. *Astron. Astroph. Sup. Ser.*, **35**, 391.

Boyle, B.J., 1986. Ph.D. thesis, University of Durham.

Boyle, B.J., Fong, R., Shanks, T., Peterson, B.A., 1987. *Mon. Not. R.*

astr. Soc, **227**, 717.

Boyle, B.J., Shanks, T., Peterson, B.A., 1988. *Mon. Not. R. astr. Soc*, **235**, 935.

Boyle, B.J., Fong R., Shanks, T., Peterson, B.A., 1990. *Mon. Not. R. astr. Soc*, **243**, 1.

Boyle, B.J., Jones, L.R., Shanks, T., Marano, B., Zitelli, V., Zamorani, G., 1991. in *Space Distribution of Quasars*, ed. Crampton, Publ. Astron. Soc. Pacific.

Broadhurst, T.J., Ellis, R.S., Shanks, T., 1988. *Mon. Not. R. astr. Soc*, **235**, 827.

Burrows, D.N., McCammon, D., Sanders, W.T., Kraushaar, W.L., 1984. *Astrophys. J.*, **287**, 208.

Canizares, C.R., & White, J.L., 1989. *Astrophys. J.*, **339**, 27.

Carrera, F.J., Barcons, X., Butcher, J.A., Fabian, A.C., Stewart, G.C., 1991. *Mon. Not. R. astr. Soc*, **249**, 698.

Cheng, F.Z., Danese, J., De Zotti, G., Franceschini, A., 1985. *Mon. Not. R. astr. Soc*, **212**, 857.

Christensen, C.G., 1975. *Astron. J.*, **80**, 282.

Cowie, L.L., 1989. in *23rd ESLAB Symposium on X-ray Astronomy*, ed. Hunt & Battrick, ESA Publ. Division.

Cowsik, R. & Kobetich, E.J., 1972. *Astrophys. J.*, **177**, 585.

Dahari, O., & De Robertis, M.M., 1988. *Astrophys. J. Sup. Ser.*, **67**, 249.

de Grijp, N.H.K., Miley, G.K., Lub, J., de Jong, T., 1985. *Nature*, **314**, 240.

de Grijp, M.H.K., Miley G.K., Lub, J., 1987. *Astron. Astroph. Sup. Ser.*, **70**, 95.

de Grijp, M.H.K. *et al.* , 1990. *in preparation.*

de Voucouleurs, G., 1971. *Pub. Astron. Soc. Pacific*, **83**, 113.

De Zotti, G., Persic, M., Franceschini, A., Danese, L., Palumbo, G.G.C., Boldt, E.A., Marshall, F.E., 1990. *Astrophys. J.*, **351**, 22.

Eaton, N., 1988. *Starlink User Note*, 45.1.

Edelson, R.A., Malkan, M.A., Rieke, G.H., 1987. *Astrophys. J.*, **321**, 233.

Ellington, E., Yee, H.K.C., Green, R.F., 1991. in *Space Distribution of Quasars*, ed. Crampton, *Pub. Astron. Soc. Pacific.*

Elvis, M. *et al.* , 1978. *Mon. Not. R. astr. Soc*, **183**, 129.

Elvis, M. & Lawrence, A., 1985. in *Astrophysics of Active Galaxies and Quasi Stellar Objects*, ed. J.S. Miller, University Science Books.

Fabian, A.C., 1975. *Mon. Not. R. astr. Soc*, **172**, 149.

Fabian, A.C., Canizares, C.R., Barcons, X., 1989. *Mon. Not. R. astr. Soc*, **239**, 15p.

Fabian, A.C., George, I.M., Miyoshi, S., Rees, M.J., 1990. *Mon. Not. R. astr. Soc*, **242**, 14.

Fabbiano, G., 1989. *Ann. Rev. Astron. Astroph.*, **27**, 87.

Feigelson, E.D., Nelson, P.I., 1985. *Astrophys. J.*, **293**, 192.

Felten, J.E., 1977. *Astron. J.*, **82**, 861.

Field, G.B. & Perrenod, S.C., 1977. *Astrophys. J.*, **215**, 717.

Fomalont, E., Kellerman, K., Wall J., 1984. *Astrophys. J.*, **277**, L23.

Franceschini, A., Gioia, I.M., Maccacaro, T., 1986. *Astrophys. J.*, **301**, 124.

Garmire, G. & Nousek, J., 1981. *Bull. Amer. Astron. Soc.*, **12**, 853.

Georgantopoulos, I., Stewart, G.C., Pounds, K.A., Shanks, T., Boyle, B.J., Griffiths, R.E., 1991. in *Space Distribution of Quasars*, ed. Crampton, *Pub. Astron. Soc. Pacific.*

Georgantopoulos, I., Stewart, G.C., Griffiths, R.E., Shanks, T., Boyle, B.J., 1992. in *X-ray Emission from AGN and the X-ray Background*, ed. Brinkmann, MPE report.

Giacconi, R., Gursky, H., Paolini, F., 1962. *Phys. Rev Lett.*, **9**, 439.

Giacconi, R. *et al.* , 1979. *Astrophys. J.*(Letters), **234**, L1.

Giacconi, R. & Zamorani, G., 1987. *Astrophys. J.*, **313**, 20.

Gioia, I.M., Maccacaro, T., Schild, R.E., Stocke, J.T., Liebert, J.W., Danzinger, I.J., Kunth, D., Lub, J., 1984. *Astrophys. J.*, **283**, 495.

Gioia, I.M., Maccacaro, T., Schild, R.E., Wolter, A., Stocke, J.T., Morris, S.L., Henry, J.P., 1990. *Astrophys. J. Sup. Ser.*, **72**, 567.

Graham, J.A., 1982. *Pub. Astron. Soc. Pacific*, **94**, 244.

Green, R.F., 1988. in *The Age of Galaxy Formation*, ed. Frenk *et al.* , Kluwer.

Griffiths, R.E., Tuohy, I.R., Brissenden, R.J.V., Ward, M., Murray, S.S., Burg, R., 1988. in *Proc. of a Workshop on Optical Surveys for Quasi Stellar Objects*, ed. P.S. Osmer *et al.* , *Pub. Astron. Soc. Pacific*.

Griffiths, R.E. & Padovani, P., 1990. *Astrophys. J.*, **360**, 483.

Groth, E.J. & Peebles, P.J.E., 1977. *Astrophys. J.*, **217**, 835.

Guilbert, P.W. & Fabian, A.C., 1986. *Mon. Not. R. astr. Soc*, **220**, 439.

Hamilton, T.T. & Helfand, D.J., 1987. *Astrophys. J.*, **318**, 93.

Hasinger, G., Schmidt, M., & Trumper, J., 1991. *Astron. Astrophys.*, **246**, L2.

Hayes, D.S. & Latham, D.W., 1975. *Astrophys. J.*, **197**, 593.

Heizler, J. & Ostriker, J.P., 1988. *Astrophys. J.*, **332**, 543.

Holmberg, E., 1937. *Ann. Lund Obs.*, **6**.

Huchra, J.P., Wyatt, W.F., Davis, M., 1982. *Astron. J.*, **87**, 1862.

Huchra, J.P. & Burg, R., 1990. *in preparation.*

Iovino, A., Melnick, J., Shaver P., 1988. *Astrophys. J.* (Letters), **330**, 117.

Iovino, A., Shaver, P.A., Cristiani, S., 1991. in *Space Distribution of Quasars*, ed. Crampton, Publ. Astron. Soc. Pacific.

Iwan, D., Marshall, F.E., Boldt, E.A., Mushotzky, R.F., Shafer, R.A., Stottlemeeyer, A., 1982. *Astrophys. J.*, **260**, 111.

Johnson, H.L. & Morgan, W.W., 1953. *Astrophys. J.*, **117**, 313.

Joseph, R.D., 1986. in *Light on Dark Matter*, ed. F.P. Israel, Dordrecht Reidel.

Koo, D.C., Kron, R.G., Cudworth, 1986. *Pub. Astron. Soc. Pacific*, **98**, 285.

Kriss, G.A. & Canizares, C.R., 1985. *Astrophys. J.*, **297**, 177.

Kruper, J.S. & Canizares, C.R., 1989. *Astrophys. J.*, **343**, 66.

Kruszewski, 1988. *preprint.*

Lampton, M., Margon, M., Bowyer, S., 1976. *Astrophys. J.*, **208**, 177.

Landolt, A.U., 1983. *Astron. J.*, **88**, 439.

Lawrence, A. & Elvis, M., 1982. *Astrophys. J.*, **253**, 410.

Lawrence, A., Rowan-Robinson, M., Leech, K., Jones, D.H.P., Wall, J.V., 1989. *Mon. Not. R. astr. Soc*, **240**, 329.

Limber, D.N., 1953. *Astrophys. J.*, **117**, 134.

Maccacaro, T., Gioia, I.M., Stocke, J.T., 1984. *Astrophys. J.*, **283**, 486.

Maccacaro, T. & Gioia, I.M., 1986. *Astrophys. J.*, **303**, 614.

Maccacaro, T., Gioia, I.M., Wolter, A., Zamorani, G., Stocke, J., 1988. *Astrophys. J.*, **326**, 80.

Maccacaro, T., della Cecca, R., Gioia, I.M., Morris, S.L., Stocke, J.T., Wolter, A., 1991. *Astrophys. J.*, **374**, 117.

Marshall, F.E., Boldt, E.A., Holt, S.S., Miller, R.B., Mushotzky, R.F., Rose, L.A., Rotschild, R.E., Serlemitsos, P.J., 1980. *Astrophys. J.*, **235**, 4.

Marshall, H.L., Avni, Y., Tananbaum, H., Zamorani, G., 1983. *Astrophys. J.*, **269**, 35.

Marshall, H.L., Avni, Y., Bracessi, A., Huchra, J., Tananbaum, H., Zamorani, G., Zitelli, V., 1984. *Astrophys. J.*, **283**, 50.

Marshall, H.L., 1991. in *Space Distribution of Quasars*, ed. Crampton, Publ. Astron. Soc. Pacific.

Marshall, H., 1987. *Astron. J.*, **94**, 3.

Mather, J.C. *et al.* , 1990. *Astrophys. J.* (Letters), **354**, L37.

Mobasher, B., 1987. Ph.D. thesis, University of Durham.

Morrison, R. & McCammon, R., 1983. *Astrophys. J.*, **270**, 119.

Mushotzky, R.F., 1982. *Astrophys. J.*, **256**, 92.

Mushotzky, R.F., & Wandel, A., 1989. *Astrophys. J.*, **339**, 674.

Nandra, K., 1991. Ph.D. thesis, University of Leicester.

Neugebauer, G. *et al.* , 1984. *Astrophys. J.* (Letters), **278**, L1.

Neyman, J. & Scott, E.L., 1952. *Astrophys. J.*, **116**, 144.

Osmer, P.S., 1981. *Astrophys. J.*, **247**, 762.

Peacock, J., 1986. in *Quasars*, ed. Swarup & Kapahi, Reidel.

Peebles, P.J.E. & Hauser, M.G., 1980. *Astrophys. J. Sup. Ser.*, **28**, 19.

Peebles, P.J.E., 1980. *The Large Scale Structure of the Universe*, Princeton University Press.

Peebles, P.J.E., 1981. *Astrophys. J.*, **248**, 885.

Penzias, A.A., Wilson, R.W., 1965. *Astrophys. J.*, **142**, 419.

Persic, M., De Zotti, G., Danese, L., Francesohini, A., Palumbo G.G.C., 1989. *Astrophys. J.*, **344**, 125.

Persic, M., De Zotti, G., Boldt, E.A., Marshall, F.E., Danese, L., Franceschini, A., Palumbo, G.G.C., 1989. *Astrophys. J.* (Letters), **336**, L47.

Petre, R., Mushotzky, R.F., Krolik J.H., Holt, S.S., 1984. *Astrophys. J.*, **280**, 499.

Pfefferman, E. *et al.* , 1986. *Proc. SPIE*, **733**, 519.

Piccinoti, G., Mushotzky, R.F., Boldt, E.A., Holt, S.S., Marshall, F.E., Serlemitsos, P.J., Shafer, R.A., 1982. *Astrophys. J.*, **253**, 485.

Pounds, K.A., 1977. *Ann. New York Acad. Sci.*, **302**, 161.

Press, W.H., Flannery, B.P., Teukolsky, S.A., Vetterling, W.T., 1986. *Numerical Recipes*, Cambridge University Press.

Primini, F.A., Murray, S.S., Huchra, J., Schild, R. Burg, R., Giacconi, R., 1991. Astrophys. J., in press.

Protheroe, R.J., Wolfendale, A.W., Wdowczyk, J., 1980. *Mon. Not. R. astr. Soc*, **192**, 445.

Reichert, G.A., Mushotsky, R.F., Petre, R., Holt, S.S., 1985. *Astrophys. J.*, **296**, 69.

Richstone, D.O. & Schmidt, M., 1980. *Astrophys. J.*, **235**, 377.

Rubin, V.C., 1954. *Proc. Nad. Acad. Sci.*, **40**, 541.

Sandage, A., Tammann, G.A., Yahil, A., 1979. *Astrophys. J.*, **232**, 352.

Schechter, 1976. *Astrophys. J.*, **203**, 297.

Scheuer, F.A.G., 1974. *Mon. Not. R. astr. Soc*, **166**, 329.

Schmidt, M., 1968. *Astrophys. J.*, **151**, 393.

Schmidt, M., 1972. *Astrophys. J.*, **176**, 273.

Schmidt, M. & Green, R.F., 1983. *Astrophys. J.*, **269**, 352.

Schmidt, M. & Green, R.F., 1986. *Astrophys. J.*, **305**, 68.

Schmidt, M., Schneider, D.P., Gunn, J. E., 1986. *Astrophys. J.*, **310**, 518.

Schmitt, J.H.M., 1985. *Astrophys. J.*, **293**, 178.

Schwartz, D.A., Qian, Y., Tucker, W.H., 1989. in *23rd ESLAB Symposium on X-ray Astronomy*, ed. Hunt & Battrick, ESA Publ. Division.

Setti, G., 1990. in *The Galactic and Extragalactic background radiation*, ed. Bowyer & Leinert, Reidel.

Shafer, R., 1983. Ph.D. thesis, University of Maryland.

Shafer, R. & Fabian, A.C., 1983. in *Proc. IAU symposium 104*, ed. Abell & Chincarini, Reidel.

Shane, C.D. & Wirtanen, C.A., 1954. *Astron. J.*, **59**, 285.

Shanks, T., Fong, R., Boyle, B.J., Peterson, B.A., 1987. *Mon. Not. R. astr. Soc*, **227**, 739.

Shanks, T., Boyle, B.J., Peterson, B.A., 1988. in *Proc. of a workshop on Optical Surveys for Quasars*, ed. Osmer *et al.* , *Pub. Astron. Soc. Pacific*.

Shanks, T., Hale-Sutton, D., Fong, R., Metcalfe, N., 1989. *Mon. Not. R. astr. Soc*, **237**, 589.

Shanks, T., Georgantopoulos, I., Stewart, G.C., Pounds, K.A., Boyle, B.J., Griffiths, R., 1991. *Nature*, **353**, 6342.

Shanks, T., Hale-Sutton, D., Fong, R., Metcalfe, N., 1989. *Mon. Not. R. astr. Soc*, **237**, 589.

Shanks, T., Fong R., Boyle, B.J., Peterson, B.A., 1987. *Mon. Not. R. astr. Soc*, **227**, 739.

Shapiro, S.L., 1971. *Astron. J.*, **76**, 291.

Shaver, P., 1988. in *Proc. of a workshop on Optical Surveys for Quasars*, ed. Osmer *et al.* , *Pub. Astron. Soc. Pacific*.

Soifer, B.T., Houck, J.R., Neugebauer, G., 1987. *Ann. Rev. Astron. Astroph.*, **25**, 187.

Soneira, R.M. & Peebles, P.J.E., 1977. *Astrophys. J.*, **211**, 1.

Spinoglio, L. & Malkan, M.A., 1989. *Astrophys. J.*, **342**, 83.

Stephens, S.A., 1988. *Astron. J.*, **97**, 10.

Stocke, J., Liebert, J., Gioia, I., Griffiths, R., Maccacaro, T., Danzinger, I., Kunth, D., Lub, J., 1983. *Astrophys. J.*, **273**, 458.

Strukov, I.A., 1990. in *The Galactic and Extragalactic background radiation*, ed. Bowyer & Leinert, Reidel.

Tananbaum, H. *et al.* , 1979. *Astrophys. J.* (Letters), **234**, L9.

Tananbaum, H., Avni, Y., Green, R.F., Schmidt, M., Zamorani, G., 1986. *Astrophys. J.*, **305**, 57.

Taylor, G.B. & Wright, E.L., 1989. *Astrophys. J.*, **339**, 619.

Totsuji, H. & Kihara, T., 1969. *Publ. Astron. Soc. Japan*, **21**, 221.

Trinchieri, G. & Fabbiano, G., 1985. *Astrophys. J.*, **296**, 447.

Turner, M.J.L., Williams, O.R., saxton, R., Stewart, G.C., Courvoisier, T.J.L., Ohashi, T., Makishima, K., Kii, T., Inoue, H., 1989. in *23rd ES-LAB Symposium on X-ray Astronomy*, ed. Hunt & Battrick, ESA Publ. Division.

Turner, T.J., & Pounds, K.A., 1989. *Mon. Not. R. astr. Soc*, **240**, 833.

Tyson, J.A., 1984. in *IAU Symposium 78, Astronomy with Schmidt type telescopes* , ed. Capaccioli, Reidel.

Urry, C.M. *et al.* , 1989. in *23rd ESLAB Symposium on X-ray Astronomy*, ed. Hunt & Battrick, ESA Publ. Division.

van den Bergh, S., 1961. *Z. Astrophys.*, **53**, 219.

Veron, P., 1983. *Quasars and Gravitational Lenses*, 24th liege Astrophysical Symposium.

Veron, M.P. & Veron, P., 1987. *A Catalogue of Quasars and Active Nuclei (3rd Edition)*, European Southern Observations.

Veron, P., 1986. in *Structure and Evolution of Active Galactic Nuclei*, ed. Giuricin *et al.* , Reidel.

Warren, S.J., Hewett, P.C., Osmer ,P.S., 1988. in *Proceedings of a Workshop on Optical Surveys for Quasars*, ed. P.S. Osmer *et al.* , *Pub. Astron. Soc. Pacific*.

Warwick, R. & Stewart, G.C., 1989. in *23rd ESLAB Symposium on X-ray Astronomy*, ed. Hunt & Battrick, ESA Publ. Division.

Webster, A., 1976. *Mon. Not. R. astr. Soc*, **175**, 61.

Weedman, D.W., 1986. *Quasar Astronomy*, Cambridge Astrophysics Series.

Weedman, D.W., 1986b. in *Structure and Evolution of Active Galactic Nuclei*, ed. Giuricin *et al.* , Reidel.

Wetherill, G.B., 1982. *Elementary Statistical Methods*, Chapman and Hall.

Wilkes, J.B. & Elvis, M., 1987. *Astrophys. J.*, **323**, 243.

Wilkes, B.J., Masnou, J.L., Elvis, M., McDowell, J., Arnaud, K., 1989. in *23rd ESLAB Symposium on X-ray Astronomy*, ed. Hunt & Battrick, ESA Publ. Division.

Wright, R., 1979. *Astrophys. J.*, **232**, 348.

Xu, C, De Zotti, G., Franceschini, A., Danese, L., 1988. *Astron. Astrophys.*, **196**, 59.

Yee, H.K.C. & Green, R.F., 1988. in *proceedings of a workshop on Optical Surveys for quasars*, ed. Osmer *et al.* , *Pub. Astron. Soc. Pacific*.

Young, E. *et al.* , 1984. *Astrophys. J.* (Letters), **278**, L75.

Zamorani, G., *et al.* , 1981. *Astrophys. J.*, **245**, 357.

Zamorani, G., Giommi, P. Maccacaro, T., Tananbaum, H., 1984. *Astrophys. J.*, **278**, 28.

Zamorani, G., Gioia, I.M., Maccacaro, T., Wolter, A., 1988. *Astron. Astrophys.*, **196**, 39.